UNIVERSIDADE FEDERAL DO CEARÁ
CENTRO DE TECNOLOGIA
DEPARTAMENTO DE ENGENHARIA METALÚRGICA E DE MATERIAIS
PROGRAMA DE PÓS-GRADUAÇÃO EM ENGENHARIA E CIÊNCIA DE MATERIAIS

BRENO RABELO COUTINHO SARAIVA

EFFECT OF CYCLIC LOADING ON MICROSTRUCTURAL EVOLUTION OF ADDITIVELY MANUFACTURED Co-28Cr-6Mo ALLOY: STUDY OF AS-BUILT AND REVERSE TREATED CONDITIONS

FORTALEZA
2023

BRENO RABELO COUTINHO SARAIVA

EFFECT OF CYCLIC LOADING ON MICROSTRUCTURAL EVOLUTION OF ADDITIVELY MANUFACTURED Co-28Cr-6Mo ALLOY: STUDY OF AS-BUILT AND REVERSE TREATED CONDITIONS

Thesis submitted to the Pos-Graduate Program in Engineering and Materials Science of the Universidade Federal do Ceará, in partial fulfilment of the requirements for the degree of Master in Materials Science and Engineering. Concentration area: Transformation and degradation processes of materials.

Advisor: Prof. Dr. Mohammad Masoumi.

FORTALEZA

2023

Dados Internacionais de Catalogação na Publicação
Universidade Federal do Ceará
Sistema de Bibliotecas
Gerada automaticamente pelo módulo Catalog, mediante os dados fornecidos pelo autor

---

S246e Saraiva, Breno Rabelo Coutinho.
Effect of cyclic loading on microstructural evolution of additively manufactured Co-28Cr-6Mo alloy: Study of as-built and reverse treated conditions / Breno Rabelo Coutinho Saraiva. – 2023.
98 f. : il. color.

Dissertação (mestrado) – Universidade Federal do Ceará, Centro de Tecnologia, Programa de Pós- Graduação em Engenharia e Ciência de Materiais, Fortaleza, 2023.
Orientação: Prof. Dr. Mohammad Masoumi.

1. Co-Cr-Mo alloy. 2. Laser powder bed fusion. 3. Martensitic transformation. 4. Electron backscattered diffraction. 5. Synchrotron X-ray diffraction. I. Título.

CDD 620.11

BRENO RABELO COUTINHO SARAIVA

EFFECT OF CYCLIC LOADING ON MICROSTRUCTURAL EVOLUTION OF ADDITIVELY MANUFACTURED Co-28Cr-6Mo ALLOY: STUDY OF AS-BUILT AND REVERSE TREATED CONDITIONS

Thesis submitted to the Pos-Graduate Program in Engineering and Materials Science of the Universidade Federal do Ceará, in partial fulfilment of the requirements for the degree of Master in Materials Science and Engineering. Concentration area: Transformation and degradation processes of materials.

Approved at: November 24th, 2023

EXAMINING COMMISSION

_____

Prof. Dr. Mohammad Masoumi (Advisor)
Universidade Federal do ABC (UFABC)

_____

Prof. Dr. João Pedro de Sousa Oliveira
Universidade Nova de Lisboa (UNL)

_____

Prof. Dr. Cleiton Carvalho Silva
Universidade Federal do Ceará (UFC)

To God.

To my partner, Larissa.

ACKNOWLEDGMENTS

This study was financed in part by the Coordenação de Aperfeiçoamento de Pessoal de Nível Superior - Brasil (CAPES) - Código de Financiamento 001.

The microstructural characterization was done in part at Central Analítica UFC/CT-INFRAFINEP/Pro-Equipamentos-CAPES/CNPq-SisNano-MCTI 2019 (Grant 442577/2019-2)-INCTFUNCAP. This research used facilities of the Brazilian Nanotechnology National Laboratory (LNNano), part of the CNPEM, projects Nr.: SEM-C1-27387, TEM-20230737, and TEM-26161.

I would like to acknowledge the support of the Laboratório de Pesquisa e Tecnologia em Soldagem (LPTS/UFC), where the tensile tests were conducted. I am also grateful to Dr. Naga Vishnu Vardhan Mogili from the LNNano for his assistance acquiring the TEM data. I would like to acknowledge Luiz Henrique Martinez Antunes from the Universidade de Campinas for his assistance with the sample preparation for the TEM analysis. The members of the Laboratório de Pesquisa em Corrosão (LPC/UFC), where electropolishing was conducted, are also acknowledged.

I would like to express my gratitude to Dr. Miloslav Béreš for the constructive discussions and support since the beginning of my master's degree. Thank you very much for helping me to achieve my goals. I also thank Prof. Dr. Hamilton Ferreira Gomes de Abreu and Dr. Luis Flávio Gaspar Herculano for all the lessons and support.

To João Rodrigues for his teachings, especially on crystallographic texture. To Tathiane Caminha Andrade for his teachings on variant selection of HCP-martensite. To Rodrigo Loureiro and Pablo Leão for all their valuable tips.

To Prof. Dr. Mohammad Masoumi for his excellent guidance.

The colleagues at the LACAM are all acknowledged for their reflections, criticisms, and suggestions.

To Larissa de Sousa Oliveira, my partner. Thank you very much for being by my side during every moment of my life.

ABSTRACT

The Co-28Cr-6Mo (wt.-%) alloy can be used as a material for artificial hip and knee joint metallic implants. For such applications, due to the complex cyclic loading conditions, the material must exhibit high fatigue resistance. This property is affected by the deformation-induced martensitic transformation (DIMT) because hexagonal close-packed (HCP) martensite acts as a preferential path for crack propagation. DIMT enables the formation of four orientational crystallographic variants. The influence of DIMT on the fatigue life of these alloys is already known. However, there is still a lack of literature discussing in detail the effect of crystallographic variants on this property. Hence, it is necessary to determine the effect of cyclic loading on the mechanical and microstructural evolution of the Co-28Cr-6Mo alloy, emphasizing the role of the martensite crystallographic variants. This can be accomplished by combining characterization techniques such as scanning electron microscopy and *in situ* synchrotron X-ray diffraction experiments. In this sense, an MP1 Co-28Cr-6Mo metallic powder was used as a raw material to produce samples by the laser powder bed fusion (L-PBF) process. This process allows higher ultimate tensile strength (1190 MPa) and yield strength (972 MPa) than those for the casting process (897 MPa and 517 MPa). After the L-PBF process, two material conditions were studied under load-controlled cyclic testing in the low cycle fatigue regime: the as-built and the heat treated in a three-stage way (1 - solution annealing, 2 – aging, and 3 - reverse transformation). This heat treatment was performed because it enables the production of homogenized and equiaxed grain microstructures, improving the fatigue resistance of the alloy. The electron backscattered diffraction analysis revealed that cyclic loading caused DIMT phase transformation, generating an accumulation of plastic strain at the FCC/HCP interface for both studied conditions. Concerning the as-built alloy, the crack propagation was found to proceed following a zig-zag pattern along the FCC/HCP interfaces. In particular, the HCP-variants $(11\bar{1})\,[1\bar{2}\bar{1}]$ and $(1\bar{1}1)\,[1\bar{1}\bar{2}]$ with high mechanical work are most prone to crack propagation. In turn, the reverse transformation induced a weak recrystallization crystallographic texture. With the progression of plastic deformation, the strain hardening increased as HCP-martensite was produced by DIMT. The DIMT was found to follow discrete transformation stages through the HCP-martensite relative fraction. This is discussed regarding the nucleation and growth of the crystallographic HCP-variants.

Keywords: Co-Cr-Mo alloy; Laser powder bed fusion; Reverse transformation; Martensitic transformation; Electron backscattered diffraction; Synchrotron X-ray diffraction.

RESUMO

A liga Co-28Cr-6Mo (%p) é comumente aplicada como componentes de articulações artificiais para joelho e quadril. Para esse fim, devido ao carregamento cíclico característico dessas aplicações, o material precisa apresentar alta resistência à fadiga. Essa propriedade é diretamente influenciada pela Transformação Martensítica Induzida por Deformação (TMID), porque a martensita hexagonal compacta (HC) atua como caminho preferencial para a propagação da trinca. Além disso, a TMID possibilita a formação de quatro variantes cristalográficas orientacionais da fase HC. A influência da TMID na vida em fadiga dessas ligas já é conhecida, porém ainda há pouca literatura discutindo detalhadamente o efeito das variantes cristalográficas nessa propriedade. Portanto, o objetivo do presente trabalho é estudar o efeito do carregamento cíclico no comportamento mecânico e microestrutural da Liga Co-28Cr-6Mo, com ênfase no papel das variantes de martensita. Isso pode ser feito combinando-se técnicas de caracterização, como a microscopia eletrônica de varredura e experimentos *in situ* de difração de raios-x com luz síncrotron. Nesse sentido, um pó metálico MP1 Co-28Cr-6Mo foi usado como matéria-prima para produzir amostras pelo processo de Fusão em Leito de Pó a *Laser* (FLPL). Esse processo permite a obtenção de maiores limite de resistência a tração (1190 MPa) e ao escoamento (972 MPa) que os obtidos pelo processo de fundição (897 MPa e 517 MPa). Após o processo FLPL, duas condições de material foram estudadas em testes de fadiga de baixo ciclo no modo de força controlada: a condição como fabricada e a tratada termicamente em três estágios (1 - solubilização, 2 - envelhecimento e 3 - transformação reversa). Esse tratamento térmico foi realizado porque permite a produção de uma microestrutura homogeneizada e grãos equiaxiais, melhorando a resistência à fadiga da liga. A difração de elétrons retroespalhados revelou que o carregamento cíclico causou TMID, gerando um acúmulo de deformação plástica na interface matriz/HC para ambas as condições. Com relação à liga como fabricada, verificou-se que a propagação da trinca seguiu um caminho em zigue-zague ao longo das interfaces matriz/HC. Em particular, as variantes $(11\bar{1})$ $[1\bar{2}1]$ e $(1\bar{1}1)$ $[1\bar{1}2]$ com maior energia são as mais propensas à propagação da trinca. Por sua vez, a transformação reversa induziu uma textura cristalográfica de recristalização fraca. Com a progressão da deformação plástica, o encruamento aumentou à medida que a martensita HC foi produzida pela TMID. Encontrou-se que a TMID segue estágios discretos de transformação por meio da fração relativa de martensita. Isso é discutido em termos de nucleação e crescimento das variantes cristalográficas.

Palavras-chave: liga Co-28Cr-6Mo; Fusão em leito de pó a *laser*; Transformação martensítica induzida por deformação; Difração de elétrons retroespalhados; Difração de raios-x com luz síncrotron.

LIST OF FIGURES

LIST OF TABLES

LIST OF ABBREVIATIONS AND ACRONYMS

BCC	Body-Centered Cubic
DIMT	Deformation-Induced Martensitic Transformation
EBSD	Electron Backscatter Diffraction
FCC	Face-Centered Cubic
FWHM	Full Width at Half Maximun
HCP	Hexagonal Close-Packed
IPF	Inverse Pole Figure
KAM	Kernel Average Misorientation
L-PBF	Laser powder bed fusion
ODF	Orientation Distribution Function
PBF	Powder Bed Fusion
SE	Secondary Electrons
SF	Stacking Fault
SN	Shoji-Nishiyama
SP	Shockley Partial
SXRD	Synchrotron X-Ray Diffraction
TEM	Trasmission Electron Microscopy

CONTENTS

1 INTRODUCTION

The primary metallic materials used in biomedical applications are stainless steel, titanium, and cobalt alloys. They are used in cardiovascular, orthopedic, and dentistry areas. Each of these applications requires a set of specific component properties. In the case of orthopedic components, such as the acetabular cup and the femoral head, the main requirements are related to mechanical properties, specifically wear and fatigue resistance. These components are subjected to complex fatigue loads, which include tension, compression, torsion, and shear. Co-Cr-Mo alloys are, therefore, often used in these applications because they have greater fatigue resistance in the forged condition than the other candidates, i.e., stainless steels and Ti alloys (TEOH, 2000).

The fatigue life of metallic materials is directly related to the microstructural response to cyclic loading. This response has been studied as a function of the glide of crystallographic defects, such as dislocations and vacancies (POLÁK; MAN; OBRTLÍK, 2003; POLÁK; SAUZAY, 2009). The glide of crystallographic defects causes the formation of slip bands. When these bands form on the free surface, surface relief characterized by extrusions and intrusions also appears. These morphological and crystallographic features can act as stress concentrators and, therefore, imply crack nucleation and propagation during cyclic loading. This is corroborated by observations made on 316L stainless steel (POLÁK et al., 2003) and Co-Cr-Mo alloys (MITSUNOBU et al., 2014).

In the case of Co-Cr-Mo alloys, the leading plastic deformation mechanism is deformation-induced martensitic transformation (DIMT). This mechanism is responsible for the formation of the surface relief mentioned in the previous paragraph and implies the formation of a phase with fewer slip systems, hexagonal close-packed (HCP) martensite. The formation of this phase distorts the crystal lattice at the FCC/HCP interface since this interface is semicoherent (LEE; MATSUMOTO; CHIBA, 2011). Consequently, strain concentration will occur at the FCC/HCP interface, acting as a preferential path for crack propagation (KUROSU et al., 2011). Therefore, the DIMT is directly related to the fatigue life of these alloys.

In this case, DIMT is characterized by four crystallographic orientational variants for a given crystallographic orientation of the parent phase. Thus, during plastic deformation, there is a mechanism for selecting the variants that should be formed preferentially. This mechanism was described by Humbert et al. (2007) and applies to Co-Cr-Mo alloys under static loading conditions. The influence of DIMT on the fatigue life of these alloys is already known.

However, there is still a lack of literature discussing in detail the effect of the selection of crystallographic variants on this property.

At this point, grain structure is another microstructural characteristic that must be considered when studying the fatigue life of Co-Cr-Mo alloys. In this sense, reverse transformation heat treatment has been studied as a strategy for improving the fatigue life of these alloys. Wei et al. (2018) observed an increase in fatigue life from 100 cycles, with the alloy in the as-built condition via laser powder bed fusion (L-PBF) (average grain size: 108 μm), to values on the order of 10000 cycles, after the application of aging and reverse transformation heat treatments (average grain size: 24 μm).

Therefore, it is necessary to determine the effect of cyclic loading on mechanical and microstructural evolution, specifically DIMT and the formation of crystallographic variants, in addition to the effect of this phase transformation on crack nucleation and propagation. This can be done by combining heat treatments with mechanical tests (cyclic loading) and characterization techniques such as scanning electron microscopy and synchrotron X-ray diffraction.

1.1 Objectives

1.1.1 General objective

To characterize the microstructural evolution and plastic response of the Co-28Cr-6Mo alloy with progression cyclic deformation in the load-controlled low cycle fatigue regime. Here, it is proposed to study the alloy in two conditions: as-built via L-PBF and subjected to reverse transformation heat treatment.

1.1.2 Specific objectives

1. To correlate DIMT and the formation of HCP-martensite variants with plastic deformation during cyclic loading.
2. To analyze the evolution of the crystallographic texture of the FCC-phase employing *ex situ* EBSD analysis and during *in situ* synchrotron X-ray diffraction.

1.2 Thesis structure

This thesis consists of three main chapters. The first chapter provides a concise review of the essential topics on Co-Cr-Mo alloys, including their applications and microstructural aspects. It also briefly explains the characterization techniques used. The two following chapters are presented in the form of research papers.

Chapter 3 investigates the effect of cyclic loading on the microstructure and crack propagation of the Co-28Cr-6Mo alloy as-built via L-PBF. This investigation utilizes scanning electron microscopy and electron backscatter diffraction, discussing the role of HCP-martensite in the strain hardening mechanism.

Chapter 4, the second research paper, aims to study the mechanical and microstructural evolution during cyclic loading of the material subjected to a reverse transformation heat treatment. This is achieved through electron backscatter diffraction and *in situ* synchrotron X-ray diffraction, and it discusses the plasticity behavior of the alloy in terms of the HCP-phase fraction and its crystallographic variants.

Finally, Chapter 5 summarizes the conclusions from both papers in Chapters 3 and 4.

2 LITERATURE REVIEW

This section reviews the main aspects of the literature on Co-28Cr-6Mo alloys, the laser powder bed fusion process, and the microstructural aspects of Co-Cr-Mo alloys.

2.1 Co-28Cr-6Mo alloys

The chemical composition and mechanical properties of Co-28Cr-6Mo alloys for biomedical applications in the forged and cast states are specified by ASTM F75 and ASTM F1537 standards. These specifications, according to ASTM F1537, are shown in Table 1 and Table 2 for chemical composition and mechanical properties, respectively.

Table 1 – Chemical composition specification (wt.-%) for low carbon Co-28Cr-6Mo alloy.

Element	Min	Max
Cr	26,0	30,0
Mo	5,0	7,0
Mn	-	1,0
Si	-	1,0
Fe	-	0,75
Ni	-	1,0
C	-	0,14
N	-	0,25
Co	Bal.	

Source: Modified from ASTM F1537 (2011).

Table 2 – Minimum mechanical property requirements for Co-28Cr-6Mo alloy.

Condition	Ultimate tensile strength (MPa)	0.2% proof stress (MPa)	Hardness (HRC)
Solution annealed	897	517	25

Source: Modified from ASTM F1537 (2011).

In addition to the properties shown in Table 2, Co-28Cr-6Mo alloys have excellent wear and corrosion resistance. Therefore, among the possible biomedical applications of cobalt-based alloys and Co-28Cr-6Mo, it can be mentioned those listed in Table 3.

Table 3 – Areas and examples of applications of cobalt-based alloys.

Division	Example of implants
Cardiovascular	Stent
Orthopedic	Artificial joints
Dentistry	Orthodontic wire
Craniofacial	Plate and screw

Source: Hermawan, Ramdan e Djuansjah (2011).

The main field of application for these alloys is in the orthopedic area. In this field, they are used as components of hip and knee joints, as shown in Figure 1. Of particular note are the femoral head, Figure 1(a), and the femoral component, Figure 1(b). These components, especially in the case of total arthroplasty, require high wear and fatigue resistance. They are, therefore, made from Co-Cr-Mo alloys.

Figure 1 – Artificial hip (a) and knee (b) joint components that can be produced from Co-Cr-Mo alloys.

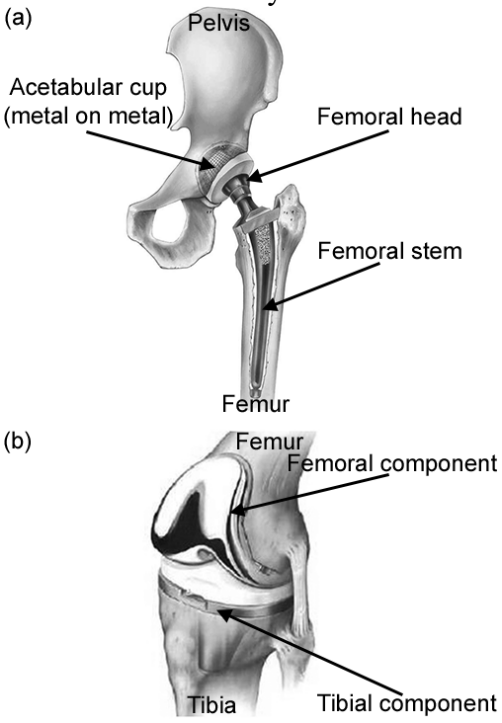

Source: Modified from Physiopedia, Purnama et al. and Turner (2022; 2015; 2012).

The use of Co-Cr-Mo alloys in the production of metal-on-metal joints has reduced the formation of debris during the wear process in comparison to other types of orthopedic implants (HERMAWAN; RAMDAN; P. DJUANSJAH, 2011). Despite this reduction in debris

volume, the formation of micro/nanoparticles and the release of metal ions still occur. These wear byproducts are associated to patient adverse reactions (BIJUKUMAR et al., 2018).

In addition to the intrinsic properties of these alloys, the production of orthopedic components by using additive manufacturing, such as L-PBF, makes it possible to produce patient-specific components. Another aspect to note is the possibility of producing parts that combine a solid core with an external layer in the form of open-cellular structures. This combination is impossible through conventional manufacturing processes and implies other advantages, such as reduced stress shielding and improved osseointegration. The former occurs because the porous structure reduces the stiffness of the Co-Cr-Mo alloy from 210 GPa to 19 GPa, which is closer to the bone stiffness (MURR et al., 2012). The second, in turn, occurs because bone growth, in addition to its anchoring, is facilitated by the possibility of cellular and vascular proliferation through the porous structure (IATECOLA et al., 2021).

2.2 Laser powder bed fusion

Here, the main aspects of the L-PBF process are briefly presented, and a schematic representation is shown in Figure 2.

Figure 2 – Schematic representation of the laser powder bed fusion (L-PBF) process.

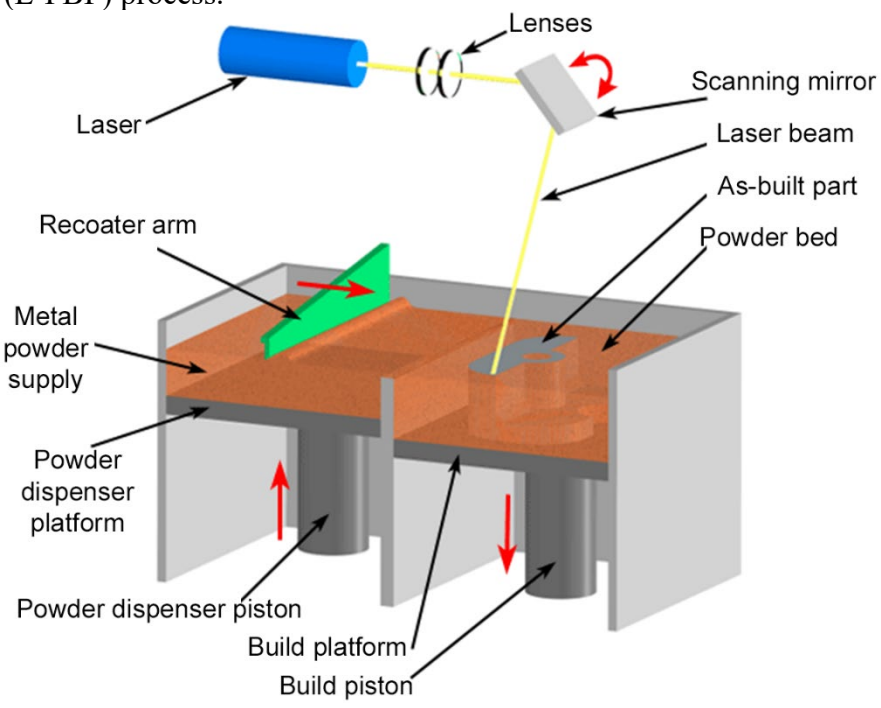

Source: Custompart.net (2022).

In this process, the part is built up layer by layer after its digital model has been segmented into slices. The main components shown in Figure 2 are the powder dispenser platform, the build platform, the recoater arm, and the laser. During operation, the recoater arm transfers a layer of powder from the powder dispenser platform to the build platform. The laser then melts the regions of the powder bed corresponding to a layer of the part. Once a layer is complete: 1 - the piston on the build platform descends; 2 - the piston on the powder dispenser platform rises; 3 – the recoater arm deposits a new layer of powder; and 4 - the laser melts a subsequent layer of the part. These steps are repeated until the entire part is complete.

The main parameters of this process include laser power, scanning speed, scanning strategy, layer thickness, hatch spacing, which is the overlap between adjacent laser paths, and powder characteristics (absorptivity, size, shape, surface roughness, and particle size distribution). These parameters can be controlled and varied to ensure that the desired microstructural, dimensional, and mechanical characteristics are obtained.

This process made it possible to obtain parts with greater ultimate tensile strength and fracture elongation than those produced by casting (WANG et al., 2021). Thus, the requirements of the ASTM F1537 standard can be met through this process, with the following advantages: the possibility of producing complex, patient-specific parts, direct production from a computer model, and porosity control.

These results can be attributed in part to the high cooling rates characteristic of the L-PBF process, which leads to a refined microstructure (PRASHANTH; ECKERT, 2017) with a high-density of crystallographic defects (WANG et al., 2021). In the as-built condition, the structure of these defects ranges from laser melting boundaries, grain boundaries, and cell structure, formed by dislocation walls in which Mo segregation occurs (ROUDNICKÁ et al., 2021a).

2.3 Microstructure of the Co-28Cr-6Mo alloy

The microstructure of Co-28Cr-6Mo alloys produced by L-PBF can be understood by considering the system as a pseudo-binary formed by the CoCr and Mo phases (PRASHANTH; ECKERT, 2017). According to these authors, during cooling, the CoCr phase forms from the liquid and expels Mo (which has low solubility in the system and is not in sufficient concentration to form another phase). Consequently, a cellular dendritic structure is formed because of the high cooling rate, with the core formed by the CoCr phase and the

contours formed by the Mo, as shown in Figure 3(a). The process also involves the formation of melt pools and a columnar grain structure, as shown in Figure 3(b) and in Figure 3(c). It should be noted that the dendritic structure is not restricted to the inside of the melting pools, as seen by the yellow (melting pools) and black (columnar grains) boundaries in Figure 3(b). This occurs through epitaxial grain growth from the previously solidified track boundaries (CHEN; PHAN; DARVISH, 2017). In the same work, it was elucidated that epitaxial growth in the Co-Cr-Mo alloy occurs by means of cellular network growth in the same direction, keeping the <100> direction at 0° or 90° about the same direction as the grain at the solidified boundary (CHEN; PHAN; DARVISH, 2017).

Figure 3 – Scanning electron micrograph, in secondary electron mode, showing the dendritic cell structure (a). Micrograph showing the melt pools, highlighted by the yellow dotted line, and the columnar grains, marked by the black dashed lines (b). Euler angle map showing the columnar grains of the Co-28Cr-6Mo alloy produced by L-PBF (c).

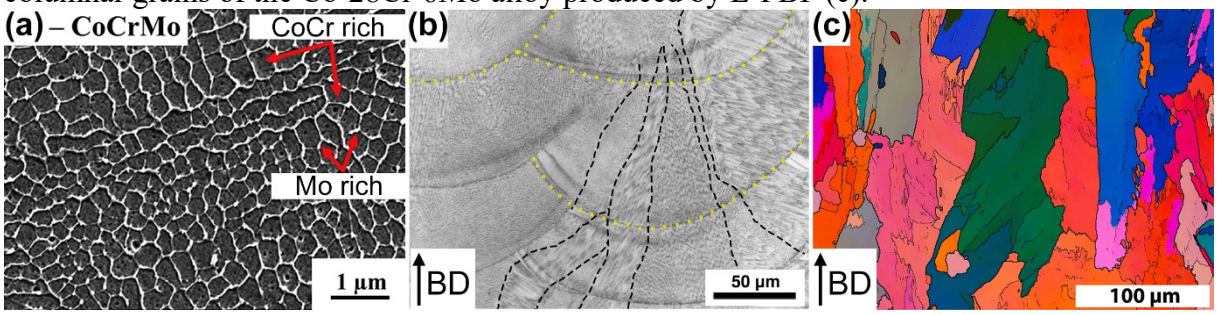

Source: Modified from Antunes et al., Prashanth and Eckert, Roudnická et al. (2021; 2017; 2021b).

The phase diagram for the Co-Cr binary system, shown in Figure 4, can be used to understand the phases present in the alloy under study, which shows behavior similar to that highlighted by the red line for 28 weight percent of Cr. Thus, for temperatures above approximately 920 °C, the stable phase is the FCC (face-centered cubic) phase, while for temperatures below approximately 900 °C, the stable phase is the HCP (hexagonal close-packed) phase. Similar behavior occurs for the Co-28Cr-6Mo alloys, except that the transformation temperatures differ.

Figure 4 – Co-Cr binary phase diagram.

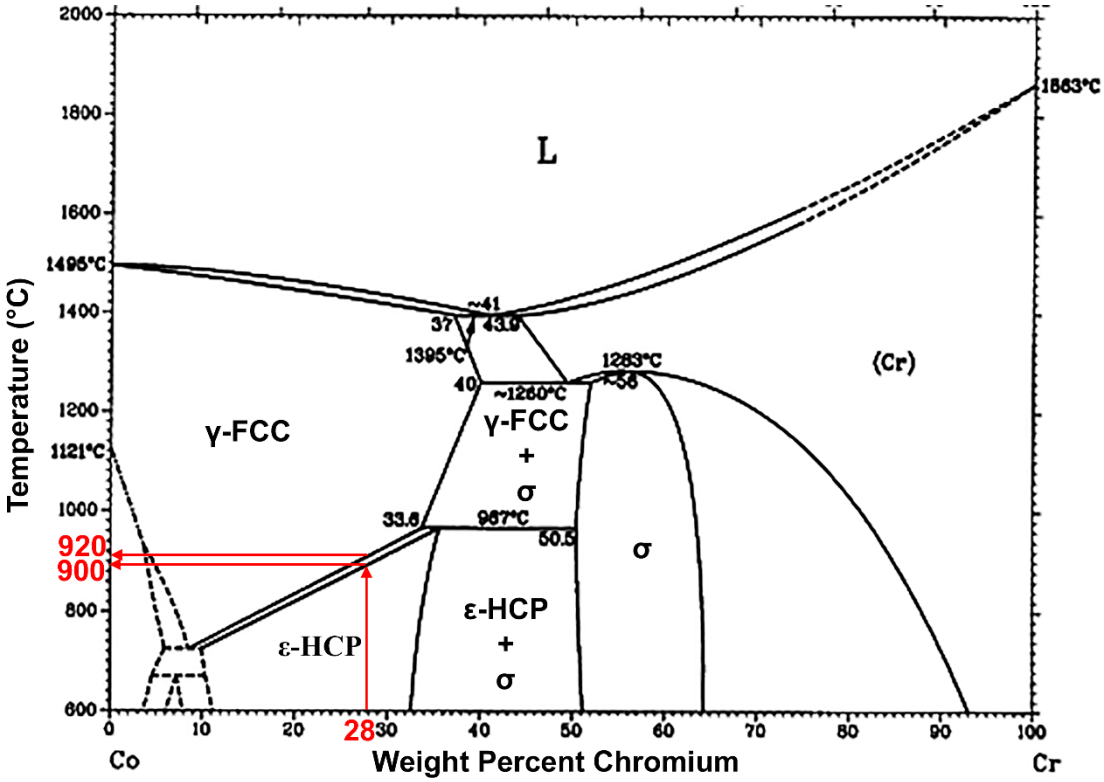

Source: Modified from Baker and Okamoto (1992).

Thus, at room temperature, the HCP phase is thermodynamically stable. However, the metastable FCC phase is observed in nonequilibrium cooling conditions. It is a metastable phase because of its higher Gibbs free energy than the HCP phase, as observed for the Co-29Cr-6Mo alloy (LI et al., 2012). Co-Cr-Mo alloys produced by L-PBF are formed predominantly by the FCC phase. On the one hand, this is because the FCC → HCP transformation process occurs slowly under conventional cooling conditions (LÓPEZ; SALDIVAR-GARCIA, 2008). On the other hand, due to the high cooling rates of L-PBF, in addition to the metastable microstructure, some authors have observed the presence of the HCP phase at contents on the order of 28% vol (ROUDNICKÁ et al., 2021b) up to 95% vol. (WANG et al., 2021). In this case, the martensite present is athermal or induced during the metallographic preparation. The other possible martensitic transformation mechanisms are isothermal and deformation-induced.

2.3.1 Martensitic transformation

As mentioned in the previous section, the FCC → HCP phase transformation can occur through one of the following mechanisms:

1) Athermal: a function of the thermal gradient used in quenching (degree of undercooling) (ZANGENEH et al., 2019) but is independent of the time at the specific temperature. Thus, the higher the degree of undercooling is, the higher the percentage of athermal martensite formed.
2) Isothermal: occurs at constant temperatures in the field where the HCP phase is stable. It is an adifusional and thermally activated transformation. It is time and temperature-dependent, showing a sigmoidal shape for the volume fraction of HCP with the heat treatment time (SALDÍVAR GARCÍA; MEDRANO; RODRÍGUEZ, 1999). Figure 5 shows an example of a temperature-time-transformation diagram for a Co-Cr-Mo-C alloy. This mechanism occurs at temperatures in the 750 °C to 900 °C range.

Figure 5 – Temperature-time-transformation diagram for the isothermal FCC → HCP transformation of the Co-Cr-Mo-C cast alloy.

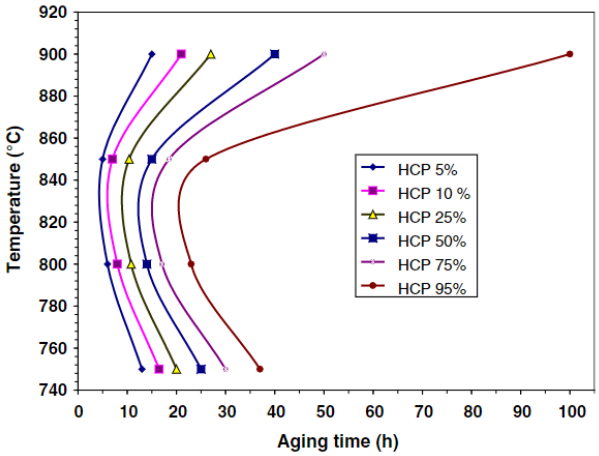

Source: (LÓPEZ; SALDIVAR-GARCIA, 2008).

3) Deformation-induced: occurs through the dissociation of perfect dislocations into their corresponding Shockley Partials on alternating $\{111\}_{FCC}$ planes (CAYRON, 2016). This is shown schematically in Figure 6, where it is possible to observe that the stacking order ABCABC... of the FCC structure is changed to the ABABAB... order of the HCP structure. This change occurs along a few atomic planes, and when stress is applied, these stacking faults have the necessary size to act as nucleation sites for the HCP phase (KOIZUMI et al., 2013). Such a mechanism is possible due to the alloy's low staking fault energy (i.e., < 15 mJ/m^2 at room temperature (PARK et al., 2022)). From the atomistic

perspective, this transformation occurs in such a way that the $(111)_{FCC}$ remains parallel to the $(0001)_{HCP}$ plane, and the direction $[110]_{FCC}$ is parallel to the $[11\bar{2}0]_{HCP}$ direction. This corresponds to the Shoji-Nishiyama (SN) orientation relationship. A schematic representation of this transformation is shown in Figure 7(a), where it can be seen that the transformation corresponds to the movement of atom M to the position initially occupied by atom N, while the latter moves to a position above atom P. Figure 7(b) shows a representation of the change in stacking order resulting from the explained rearrangement of the atoms.

Figure 6 – Schematic of the dissociation of a perfect dislocation into Shockley partials.

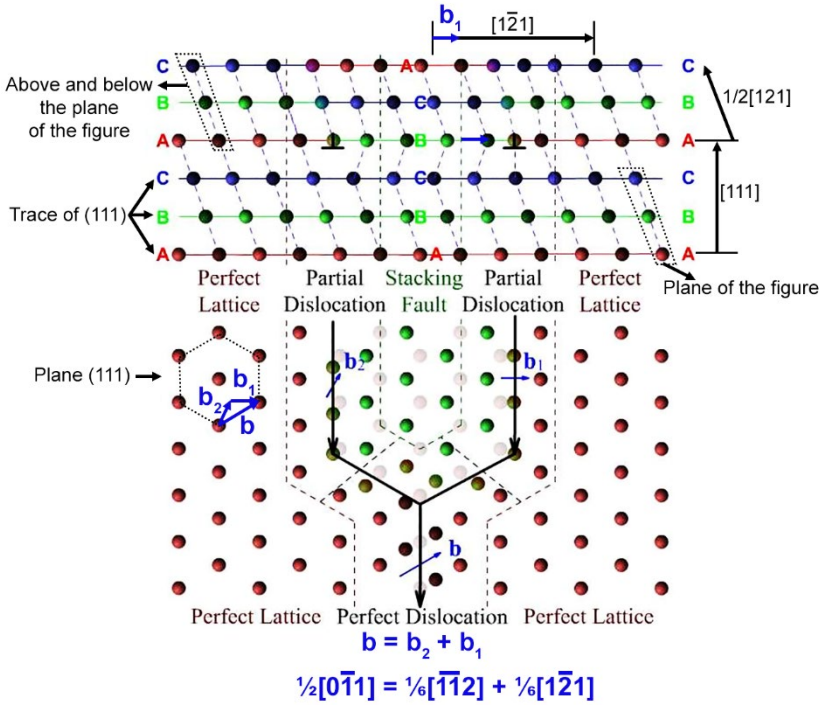

Source: Modified from Liu (2009).

Figure 7 – Schematic representation of the transformation from the point of view of atomic movements (a). Change in stacking order due to atomic rearrangement (b).

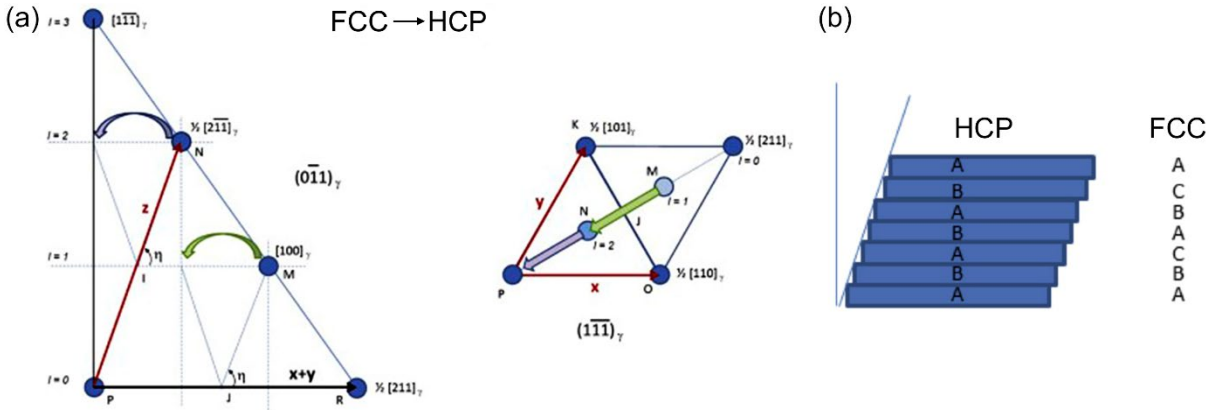

Source: Modified from Cayron (2016).

2.3.2 Heat treatments

The athermal and isothermal martensitic transformation mechanisms presented in the previous section can be used to understand the heat treatments to which Co-28Cr-6Mo alloys can be subjected.

The solution annealing consists of heating the alloy up to the FCC phase field (~1150 °C, for example). The temperature must be maintained until homogenization (chemical composition) occurs and the dendritic structure resulting from solidification under nonequilibrium conditions is eliminated, as shown in Figure 3(a). It is then cooled rapidly to prevent the formation of stable second phases. This results in a microstructure predominantly formed by the metastable FCC phase, with equiaxed grains. This treatment eliminates the inhomogeneities characteristic of processes with high cooling rates (WEI et al., 2019).

Another possible heat treatment is aging. This treatment uses the isothermal mechanism of martensitic transformation. It thus produces microstructures composed predominantly of two phases, FCC and HCP. The kinetics of this transformation is shown in Figure 5. However, the beginning of the transformation is delayed, and the kinetics of the transformation is slowed down when the alloy undergoes a previous heat treatment of solution annealing (SALDÍVAR GARCÍA; MEDRANO; RODRÍGUEZ, 1999).

To attain grain size refinement, a combination of the previous treatments has been used. This treatment consists of applying the aging treatment followed by heating to the FCC phase field, remaining in this phase field long enough for the nucleation of the FCC phase to occur without any grain growth. This last stage is called reverse transformation. An example is shown in Figure 8, which shows the application of one reverse transformation cycle. Kurosu,

Matsumoto, and Chiba (2010) observed a reduction in grain size from 201 μm after solution annealing heat treatment to 20-25 μm after reverse transformation treatment.

Regarding the grain refinement mechanism, the literature proposed that a pearlite-type structure (FCC → HCP + carbides/carbonitrides) is formed during aging. This structure would be responsible for acting as nucleation sites for size-reduced grains of the FCC phase during the reverse transformation (i.e. HCP + carbides/carbonitrides → FCC) (HASSANI et al., 2019; WEI et al., 2019; ZANGENEH; KETABCHI, 2013). Another possible explanation is based on the induction of stresses and the athermal HCP phase, both because of thermal cycling, which in this case would be the nucleation sites of the FCC phase (ZANGENEH et al., 2020).

Figure 8 – Example of a reverse transformation heat treatment.

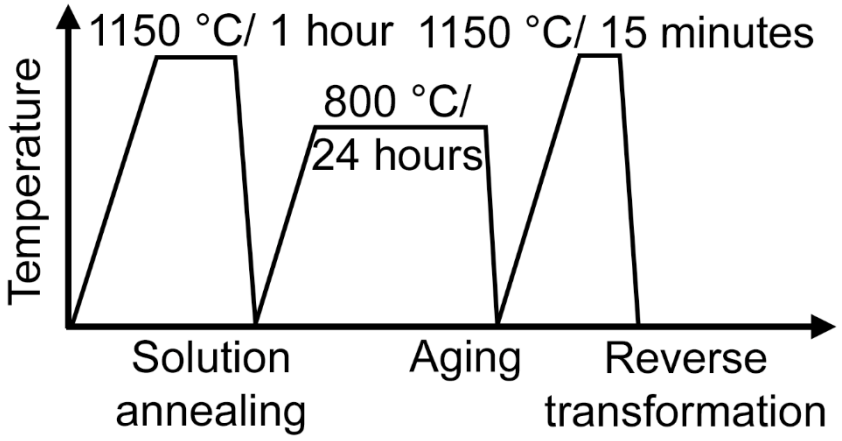

Source: Own elaboration.

2.4 Characterization techniques

2.4.1 Electron backscatter diffraction

This characterization technique is based on detecting and indexing the Kikuchi bands formed on a phosphor screen. Figure 9 schematically shows the principle of the technique.

Figure 9 – Schematic representation of the formation of Kikuchi bands.

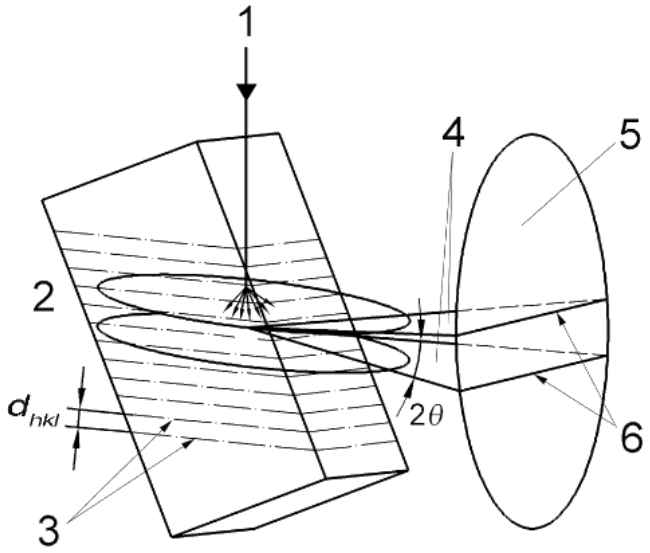

Source: (INTERNATIONAL STANDARD, 2009).

When the electron beam (1) hits a tilted crystalline sample (2), inelastic scattering occurs with little energy loss. The electrons resulting from this interaction that satisfy Bragg's Law ($2 \cdot d \cdot \text{sen}\,\theta = n \cdot \lambda$) are diffracted. Thus, for each family of planes, with interplanar spacing (d_{hkl}) and specific diffraction angle (θ), the diffracted beam forms Kossel cones (4). the diffracted beam forms Kossel cones (4). These cones intersect the phosphor screen (5), forming the Kikuchi bands (5). The Kikuchi bands are associated with the crystallographic information of interest. The spacing between the Kikuchi lines is inversely proportional to the interplanar spacing (because the diffraction angles are on the order of 1°). The intersections between the Kikuchi bands define the zone axes and crystallographic directions.

2.4.2 Synchrotron X-ray diffraction

Figure 10 shows a schematic representation of how a synchrotron source works. In this configuration, electrons are accelerated to speeds close to that of light inside a vacuum ring. Due to the radial acceleration, the electrons emit electromagnetic radiation tangential to their trajectory. This radiation is collected at specific points in the electron's trajectory by magnets or other suitable devices, defining beamlines. Once collected, the (synchrotron) radiation passes through monochromators and an optical system to focus the beam on the sample.

Figure 10 – Representation of the principle of synchrotron radiation production.

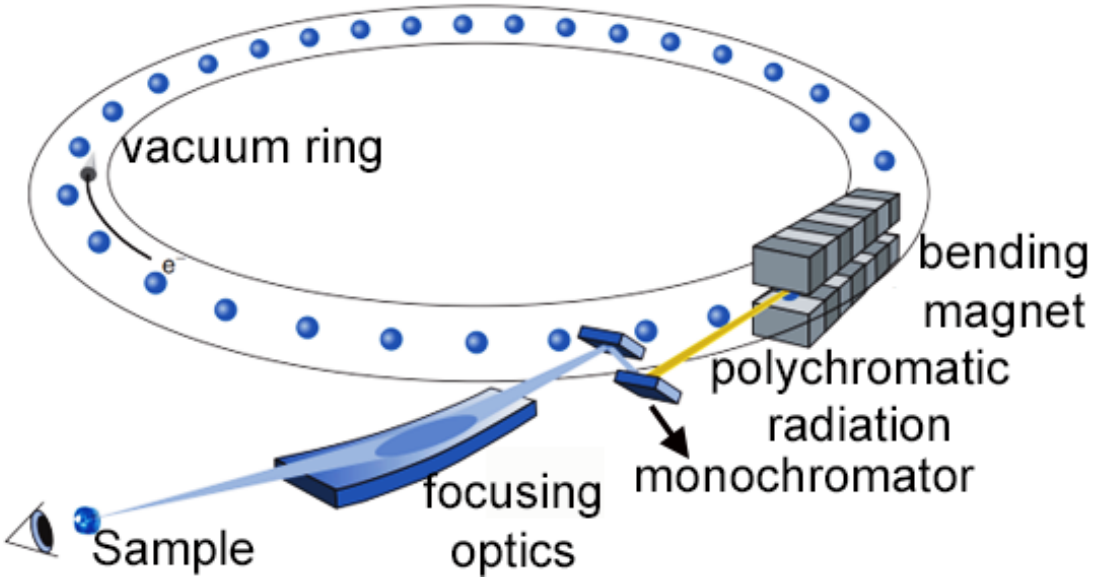

Source: Modified from Willmott (2011).

Synchrotron radiation sources can be used to carry out X-ray diffraction experiments. Due to the characteristics of this radiation, such as the high flux (10^{20} photons/s/mrad^2/mm^2/0.1% *bandwidth* (WILLMOTT, 2011)) and beam coherence, a wide variety of experimental configurations are possible. Among these possibilities, Debye-Scherrer diffraction experiments in transmission mode stand out. In this case, the sample, bulk or powder, is placed between the incident beam and the detector. When interacting with the material, the diffracted beam produces diffraction cones, called Debye-Scherrer cones, which intersect the detector (Debye-Scherrer ring) and form the diffraction pattern (set of Debye-Scherrer rings, one for each hkl reflection). An example of this experimental setup is shown in Figure 11.

Figure 11 – Schematic diagram of the geometry of the X-ray diffraction experiment in transmission mode.

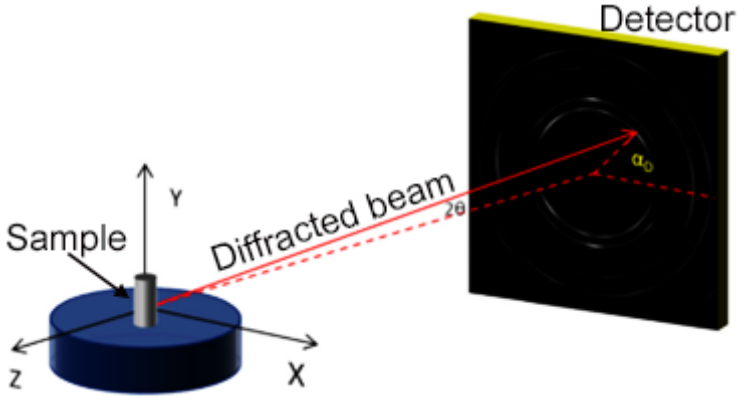

Source: Modified from Xie et al. (2013).

An important aspect that should be mentioned is the influence of the type of crystalline material on the Debye-Scherrer rings. This is shown in Figure 12, where it is possible to observe the diffraction patterns formed by a powder sample (random) and by a sample that has crystallographic texture. The effect of the texture is to produce a change in the diffracted intensity along the Debye-Scherrer rings.

Figure 12 – Schematic diagram of crystalline samples and their diffraction patterns. Sample with crystallographic texture (a) and sample in powder form (b).

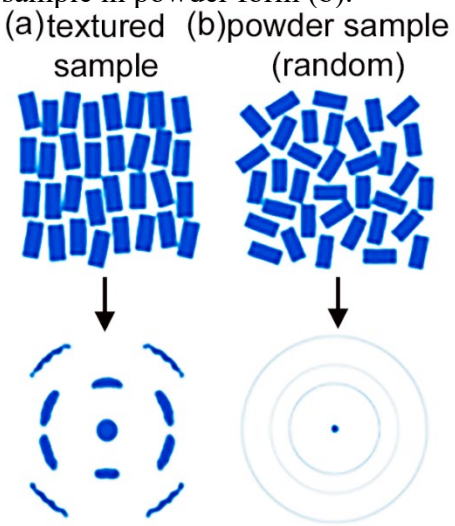

Source: Modified from Willmott (2011).

Therefore, the crystallographic texture can be obtained from these X-ray diffraction experiments. This is done by determining the orientation density along a circle on the reference sphere. The orientation density, in turn, is proportional to the intensity of the corresponding Debye-Scherrer ring. Figure 13 shows a schematic representation of this method.

Figure 13 – Geometric representation of the relationship between the position on the Debye-Sherrer ring (a) and the position on the stereographic projection (b).

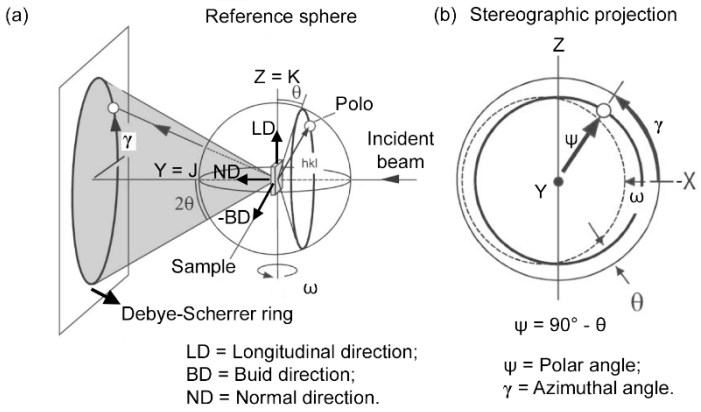

Source: Modified from Wenk and Grigull (2003).

The pole corresponding to the Debye-Scherrer ring shown in Figure 13(a), making an angle of 2θ with the incident beam, intersects the reference sphere in the orientation (ψ,γ) of the stereographic projection, Figure 13(b). Thus, the intensity along the circle shown in the projection can be determined from the corresponding intensities along the diffraction ring.

3 EFFECT OF CYCLIC LOADING ON MICROSTRUCTURE AND CRACK PROPAGATION IN ADDITIVELY MANUFACTURED BIOMATERIAL Co-Cr-Mo ALLOY

3.1 Abstract

Cobalt-chromium-molybdenum (Co-Cr-Mo) alloys are commonly used for artificial hip and knee joint metallic implants. These components are subjected to repetitive loads during service. Therefore, materials used for such applications must exhibit a high fatigue crack resistance. In this research, Co–28Cr–6Mo (wt.-%) powder was utilized as a feedstock in a laser powder bed fusion process to produce test coupons. The coupons were then subjected to load-controlled cyclic material tests in the low cycle fatigue regime to study the mechanical response and microstructural changes of the material. With the progressing number of cycles, a continuous increase in macroscopic plastic strain was observed. The Electron backscattered diffraction analysis revealed that cyclic loading caused deformation-induced face-centered cubic (FCC) → hexagonal close-packed (HCP) phase transformation. In addition, the phase transition generated an accumulation of plastic strain at the FCC/HCP interface giving rise to crack nucleation. The crack propagation path along HCP orientation variants with high mechanical work and strain hardening mechanism is discussed.

Keywords: Co-Cr-Mo alloy; Laser powder bed fusion; Deformation-induced martensitic transformation; Variant selection; Crack propagation.

3.2 Introduction

Cobalt-chromium-molybdenum (Co-Cr-Mo) alloys are commonly used for hip and knee joint implants due to their superior corrosion and wear resistance (HASSANI et al., 2016; NAJJAR et al., 2000) under sliding conditions. These artificial joint replacements are subjected to cyclic loading that can reach a high number of cycles per year (YANG et al., 2021). Therefore, the fatigue fracture of such components is one of the major concerns for their application as biomaterials (TEOH, 2000). Fatigue crack nucleation is linked to microstructural changes occurring during loading along the time of usage as implants. In general, the movement and rearrangement of dislocations under cyclic loading can lead to strain localization at persistent

slip bands inducing extrusions and intrusions on the free surface (POLÁK; SAUZAY, 2009). The formed extrusions and intrusions can act as fatigue crack initiation sites. Fatigue crack nucleation in ferritic steels is commonly associated with slip localization at the free surface (SWEENEY et al., 2013). In 316 austenitic stainless steel submitted to cyclic loading, Pham and Holdsworth (2013) pointed out that dislocation ladder structures, localized deformation bands, and slip localization at persistent slip bands have a strong influence on crack initiation.

Research into the additive manufacturing of Co-Cr-Mo alloys has been mostly focused on L-PBF and electron beam melting (EB-PBF) powder bed fusion processes (SAMES et al., 2016). Kajima et al. (2016) investigated the influence of anisotropy on the fatigue properties of Co-Cr-Mo samples produced by L-PBF with varying angles between the build and longitudinal directions. Apart from the anisotropy, surface roughness was identified as an important factor that influenced fatigue strength. In addition, attempts have been made to enhance the fatigue properties of Co-Cr-Mo alloys by heat treatment (SEKI et al., 2019; WEI et al., 2018). An improvement in fatigue life was attributed to the reduction in residual stresses, elimination of molten pool boundaries (SEKI et al., 2019), and refinement of the microstructure caused by phase transformation (WEI et al., 2018) in the L-PBF and EB-PBF samples. Under static loading conditions, the face-centered cubic (FCC) phase of Co-Cr-Mo alloys can transform into a hexagonal close-packed (HCP) phase by the deformation-induced martensitic transformation (DIMT) mechanism (LÓPEZ; SALDÍVAR; HUANG, 2000). This transformation occurs due to the low stacking fault energy in this alloy system, i.e., < 15 mJ/m^2 at room temperature (KOIZUMI et al., 2013; PARK et al., 2022; YAMANAKA et al., 2009). On the one hand, the formation of the HCP phase contributes to a high strain hardening rate, wear resistance, and high energy absorption values. On the other hand, the DIMT produces a surface relief characterized mainly by steps at the $\{111\}_{FCC}$ planes (MITSUNOBU et al., 2014) which can act as crack nucleation sites. In addition, due to the reduced number of independent slip systems, the HCP phase provides a favorable path for crack propagation (KOIZUMI et al., 2013; LEE; MATSUMOTO; CHIBA, 2011).

Concerning the effects of the DIMT on the fracture behavior, it was found that a high-entropy alloy exhibited brittle-like behavior when martensite was generated (YANG et al., 2022). In that research, the authors reported that the high strain-hardening effect resulting from the DIMT of FCC to body-centered cubic (BCC) phase via intermediate HCP has led to a remarkable combination of strength and ductility (YANG et al., 2022). In other investigations, some authors have reported about beneficial effects of DIMT on ductility (CHENG et al., 2008;

MITSUNOBU et al., 2014; RAZAVI et al., 2021; SONG et al., 2016). They showed that the perpendicular lattice dilation of α″ martensite to the crack propagation plane and the lattice contraction in the 〈200〉 β direction produce compressive and tensile strain, respectively, perpendicular and parallel to the planes where the crack propagates (SONG et al., 2016). As a result, they hinder crack propagation and promote crack deflection during subsequent cyclic fatigue loading. In addition, it has been shown that other aspects, such as the crack size (WANG et al., 2022) and the morphology of the martensite (YANG et al., 2022), also impact the mechanical behavior under dynamic loading conditions.

The laser powder bed fusion (L-PBF) technique is widely used to produce customized metallic implants from alloy precursor powder (BOSE et al., 2018; LI et al., 2020). In the present investigation, a Co–28Cr–6Mo (wt.-%) alloy that is employed for orthopedic implants was produced by the L-PBF method. It is well known that DIMT leads to microstructural changes that influence mechanical behavior and fracture properties. To date, however, the effect of FCC → HCP phase transformation on crack propagation during cyclic loading in Co-Cr-Mo alloy produced via the L-PBF route has not been studied comprehensively (BÉREŠ et al., 2018; WANG et al., 2021). Therefore, the present work brings as a novelty a detailed investigation of the effect of the crystallographic HCP-variants that influenced the mechanisms of crack initiation and propagation in Co-Cr-Mo samples submitted to cyclic loading.

3.3 Materials and methods

Dog-bone shaped tensile test specimens with cross-sections of 3.46 × 1.26 mm^2 and 4 mm gauge length were manufactured by the L-PBF technique using an EOSINT 280 machine (EOS GmbH, Germany) applying process parameters provided by EOS (EOS, 2011). The determined chemical composition of the sample (in wt.-%) is 27.89Cr-6.27Mo-0.72Mn-0.62Si-0.32Fe-0.1Ni-0.14C-0.14N, balance Co. For additional experimental details, including powder feedstock, composition determination techniques, and tensile specimen design, the reader is referred to previously published works (ANTUNES et al., 2019, 2021).

To determine the mechanical properties, the as-built sample was subjected to a tensile test until failure at a strain rate of 10^{-2} (YAMANAKA; MORI; CHIBA, 2013). The determined yield and ultimate strength were 1035 and 1450 MPa, respectively. A stress of 1101 MPa was used for the cycling loading experiments with a fatigue stress ratio of 0.02. The cyclic

tests were performed up to 2018 cycles with 16 cycles per minute, using an MTS 810-FlexTest 40 servo-hydraulic testing machine. The machine operated in a force control mode where each cycle was applied with constant maximum tension load (F) equal to 4.8 kN (above the yield strength of the material) and subsequent tension release. A linear fitting algorithm using OriginPro® software (OriginPro, 2019) was utilized to determine the slope of the permanent strain increase.

Samples for electron backscattered diffraction (EBSD) characterization were prepared by electropolishing using a solution of perchloric acid (10 vol.-%) in acetic acid. EBSD maps were acquired on the region of interest prior to loading and after the application of 300 and 2018 cycles. The local crystallographic texture obtained through EBSD analysis was utilized because it enables the determination of the crystallographic texture resulting from the formation of the HCP phase within individual FCC grains. For this, FEI-Quanta 650 and 450 field emission gun scanning electron microscopes (SEM) fitted with Oxford Instruments EBSD cameras were used. The data processing was carried out using Channel 5 software. To analyze the surface morphology of the sample subjected to 2018 cycles, secondary electron (SE) images were collected. Here, an acceleration voltage of 20 keV and a working distance of 10 mm were used.

To reveal the as-built microstructure, the electropolished samples were submitted to electrochemical etching using a solution of hydrochloric acid (10 vol.-%) in distilled water applying a voltage of 6 V. Next, SE micrographs were acquired using an acceleration voltage of 20 keV and a working distance of 8 mm.

Transmission electron microscopy (TEM) studies were conducted on both as-built and deformed specimens. Disc samples were punched out from ~100 μm thick electrolytically thinned foils. Then, they were polished to electron transparency using a Struers Tenupol-3 apparatus and the electrolyte mentioned above. The bright-field (BF) TEM micrographs were acquired using a JEOL FX2100 transmission electron microscope, operating at 200 kV.

The variant selection analysis was performed following Humbert's approach (HUMBERT et al., 2007). According to this approach, the selection of the crystallographic variants occurs due to the different levels of mechanical work for each crystallographic variant, forming the variants with the highest applied stress, σ. In accordance with elasticity theory, the mechanical work would be understood as the area under the elastic portion of the stress vs. strain curve, i.e. $(1/2)\sigma\cdot\varepsilon$, where ε is the transformation strain associated with the formation of each HCP crystallographic variant. Here, the mechanical work was calculated following the

elasticity theory, with both stress and transformation strain tensors expressed in the macroscopic reference frame. The analysis was performed using $||\boldsymbol{\sigma}||$ =100 MPa, and a severity factor of 0.9 was considered. The severity factor, as proposed by Humbert, indicates that the selected variants would be the ones whose mechanical work is higher than the severity factor times the highest mechanical work among all possible variants.

3.4 Results

3.4.1 Stress-strain curve of the as-received metal and analytical investigation

The true stress-strain curve of the as-built sample is presented in Figure 14. The yield stress ($\sigma_{0.02}$) and ultimate tensile strength (σ_{max}) of the L-PBF-produced Co-Cr-Mo alloy presented values of 1035 and 1450 MPa, respectively. The total elongation where the fracture occurred was 14%. The $\sigma_{0.02}$ value shows that the specimen experienced a load of 4.5 kN at this point, lower than the maximum employed tension load during the cyclic experiment (4.8 KN). The red solid line represents the strain hardening rate (SHR) curve versus the true strain. The SHR suffers a sharp decrease from the yield point until the strain of approximately 0.03 and then continues to experiment a slight decrease. This transition corresponds to the onset of phase transformation or other softening or hardening mechanisms (LIMA et al., 2023; LIMA et al., 2022). In the present research, this may be associated with martensitic phase transformation (ARANAS et al., 2018; MENDES-FONSECA et al., 2019; RODRIGUES et al., 2018; RODRIGUES; ARANAS; JONAS, 2017). To analytically detect the approximate value of the strain where the phase transformation commenced, the double differentiation method was employed (POLIAK; JONAS, 1996). This method identifies the minima that correspond to the initiation of phase transformation and other softening or hardening mechanisms. The inset chart in Figure 14 corresponds to the result of the double differentiation curve. Here, the first minimum value of the second derivative was 1175 MPa which matched the strain of 0.036. Nonetheless, any strain greater than the first minimum value will lead to the phase transformation of austenite into martensite.

Figure 14 – Stress-strain curve of the L-PBF-produced Co-Cr-Mo alloy with its corresponding strain hardening rate (SHR) and double differentiation curve.

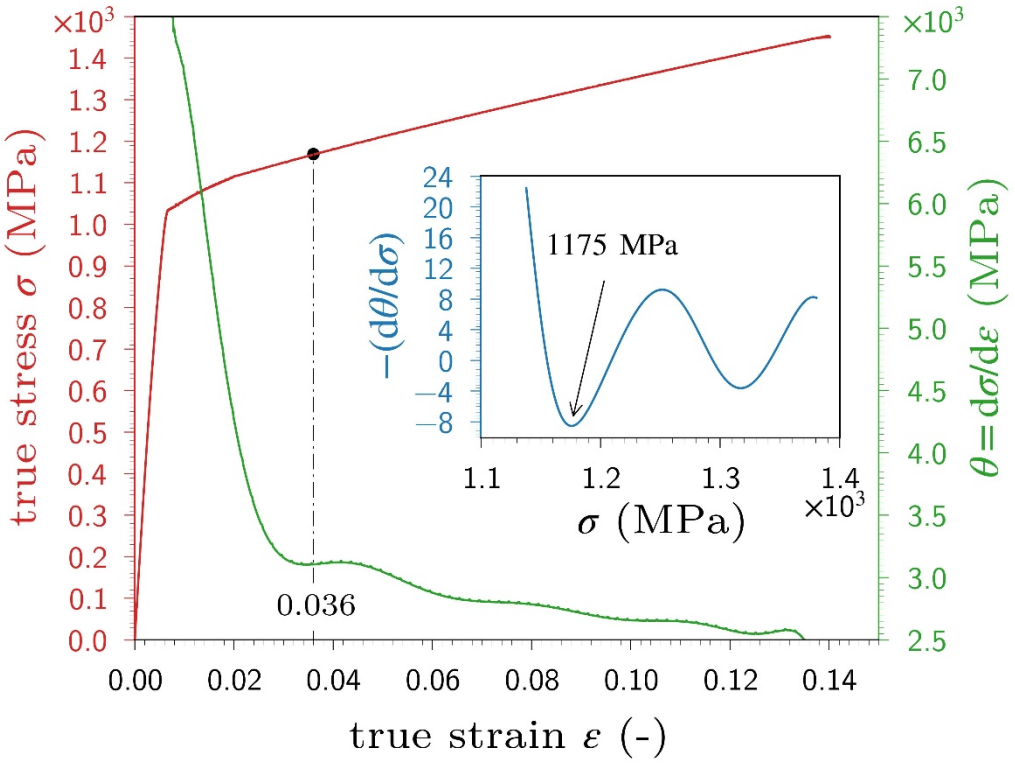

Source: Own elaboration.

3.4.2 Microstructural characteristics of the L-PBF-produced Co-Cr-Mo alloy

The high-resolution SEM image of the microstructure features of the L-PBF-produced Co-Cr-Mo alloy in the as-received condition is shown in Figure 15. Columnar dendrites grow in various directions from the molten pool boundaries, following the inverse direction of the maximum heat flux. Secondary dendrites can be seen along the primary dendritic arms at the triple molten point boundaries. Details of the fine cellular structure within the grains and in various directions in the etched as-built sample can be seen in Figure 16(a). In this micrograph, the melt-pool boundaries are highlighted by the red dashed lines, while columnar grains are highlighted by yellow dashed lines. The corresponding EBSD Euler Orientation map superimposed by the Band Contrast map is displayed in Figure 16(b). Here, it is possible to observe that the L-PBF process allowed the promotion of epitaxial grain growth, which crossed several layers and melt-pool boundaries. In the as-built sample, a single FCC phase without residual HCP phase was revealed by microstructural analysis. The presence of a single FCC phase is the result of rapid cooling that takes place during the L-PBF process.

Figure 15 – High-resolution SEM images of the dendritic structures around the molten pool boundaries in the as-built Co-Cr-Mo alloy.

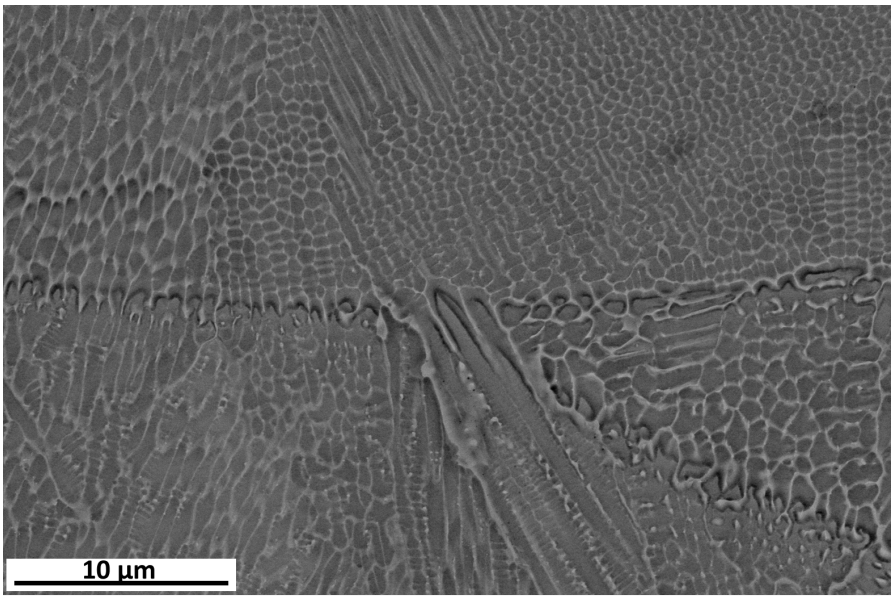

Source: Own elaboration.

Figure 16 – SE micrograph (a) and the EBSD Euler Orientation map superimposed by the Band Contrast map (b) of the as-built sample after electrochemical etching.

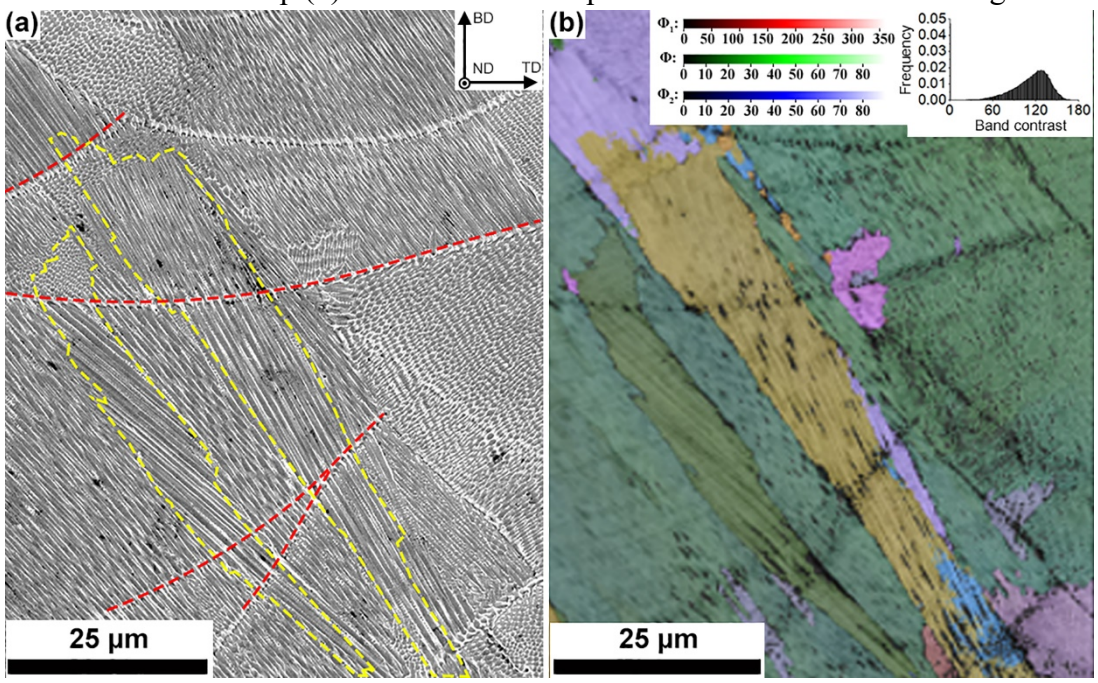

Source: Own elaboration.

3.4.3 Cyclic loading simulation

Based on the obtained results presented in Figure 14, cyclic loading parameters were chosen with the aim of investigating the mechanisms that promote deformation-induced phase transformation and crack propagation in the studied alloy fabricated via the L-PBF

process. Figure 17 presents the loading patterns and the strain response to constant cyclic loading (ΔF = 4.8 kN) of the first 30 passes of the experiment. Each pass employed equivalent stress and strain above the yield strength of the material. Here, an initial linear increase in strain amplitude values was observed in the cycle range from 1 to 30, a red straight line in Figure 3, and this trend continued until the maximum number of cycles (2018), when the sample failed. This behavior can be attributed to the plastic deformation mechanism that operates in this alloy system. The image also depicts that the applied load was kept constant throughout the entire experiment. According to the calculated onset for phase transformation, see Figure 14, in terms of stress and strain, at the end of the very first cycle of the test, a transformation of HCP martensite could have occurred.

Figure 17 – Loading patterns and strain response during the application of the first 30 loading cycles.

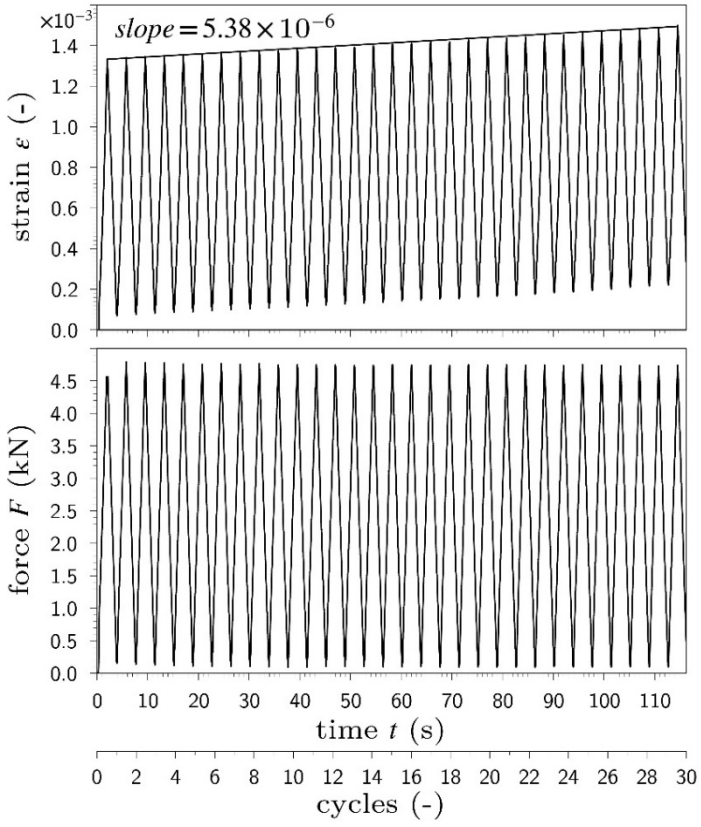

Source: Own elaboration.

3.4.4 Crystallographic features of the tested specimens

A single-phase FCC structure was observed prior to the application of the load, as shown in Figure 16(b), and Figure 18(a). In the sample submitted to 300 cycles, the presence

of the HCP phase in addition to the FCC phase was revealed and this is depicted by arrows in Figure 18(b). Therefore, it is confirmed here that cyclic loading causes deformation-induced FCC → HCP phase transformation.

Figure 18(c) and Figure 18(d) show KAM maps of the specimens prior to the employment of any force and after the application of 300 loading cycles, respectively. On the one hand, in the as-built sample, higher KAM values were found at the subgrain boundaries, as shown in Figure 18(c). On the other hand, higher KAM values were determined at FCC/HCP interfaces after FCC → HCP phase transformation, as shown in Figure 18(d). In addition, from the presented histograms, it is possible to observe a frequency increase at higher angles for the FCC phase. Figure 18(e) shows the experimentally determined pole figures for the FCC phase from the boxed region in Figure 18(a). Furthermore, Figure 18(f) shows the experimentally obtained pole figures for the FCC and HCP phases from the depicted square in Figure 18(b). One can note that the $\{111\}_{FCC}$ pole figures, Figure 18(e) and Figure 18(f), coincide with that of $\{0002\}_{HCP,}$ which is consistent with the Shoji-Nishiyama (S-N) orientation relationship (NISHIYAMA, 1978).

Experimentally determined Euler angle values for the FCC orientation from the boxed region in Figure 18(a) were used as input for variant selection analysis. Table 4 shows four possible orientation variants for the FCC → HCP phase transformation. Considering the severity factor of 0.9 in Humbert's model, only the $V_{\varepsilon 3}$ variant must be formed. However, as revealed experimentally in Figure 18(b) and Figure 18(f), the $V_{\varepsilon 1}$ variant was also detected. These two orientation variants correspond to $(111)[11\bar{2}]$ and $(1\bar{1}1)[\bar{2}11]$ Shockley partials. The calculated pole figures, plotted in Figure 18(g), contain two HCP orientation variants with the highest mechanical work (however with a severity factor below 0.9) as shown in Table 4.

Figure 18 – Inverse pole figure map (IPF) of (a) the as-built sample and (b) after 300 cycles. (c) and (d) are the corresponding kernel average misorientation (KAM) maps. (e) and (f) are experimentally determined pole figures from the boxed regions in (a) and (b) for the FCC-phase and HCP-phase. The calculated pole figures of the HCP variants are presented in (g). (BD = build direction, ND = normal direction, TD = tensile direction).

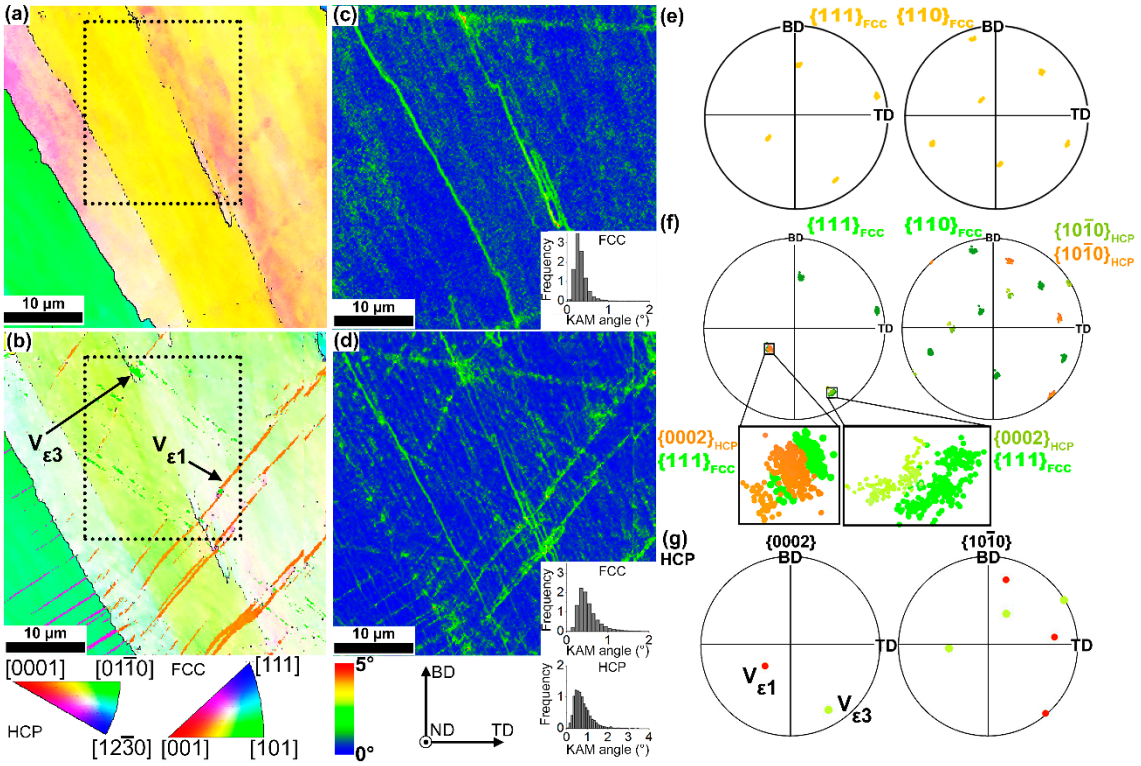

Source: Own elaboration.

Table 4 – Calculated crystallographic variants of the HCP-phase considering experimentally obtained Euler angles in the boxed regions in Figure 3(a) and in Figure 4(b), corresponding to the samples submitted to 300 and 2018 loading cycles, respectively. Experimentally determined Euler angles of the parent FCC phase are represented by the $[\Phi_1\ \phi\ \Phi_2]_{FCC}$ format, with angles in degrees. Bold numbers indicate the selected variants.

Variant	**Slip system**	**300 cycles**				**2018 cycles**			
		[261.6 149.4 199.2]FCC				**[327.1 29.3 34.8]FCC**			
		Euler angles (°)			**Mechanical work (MJ/m³)**	**Euler angles (°)**			**Mechanical work (MJ/m³)**
		Φ_1	**Φ**	**Φ_2**		**Φ_1**	**ϕ**	**Φ_2**	
$V_{\varepsilon 1}$	(111) [11$\bar{2}$]	**127.9**	**150.6**	**116.8**	**6.1**	**128.0**	**26.3**	**281.3**	**3.5**
	(111) [$\bar{2}$11]	127.9	150.6	236.8	-1.6	128.0	26.3	41.3	-5.7
	(111) [1$\bar{2}$1]	127.9	150.6	356.8	-4.5	128.0	26.3	161.3	2.2
$V_{\varepsilon 2}$	($\bar{1}$11) [211]	352.5	132.7	291.5	-0.8	248.1	54.9	114.0	-8.6
	($\bar{1}$11) [$\bar{1}$2$\bar{1}$]	352.5	132.7	171.5	1.7	**248.1**	**54.9**	**354.0**	**5.7**
	($\bar{1}$11) [$\bar{1}$1$\bar{2}$]	352.5	132.7	51.5	-0.9	248.1	54.9	324.0	2.8
$V_{\varepsilon 3}$	(1$\bar{1}$1) [$\bar{2}$11]	**210.8**	**108.5**	**358.9**	**7.3**	30.2	64.3	182.2	-6.9
	(1$\bar{1}$1) [121]	210.8	108.5	238.9	-5.0	30.2	64.3	62.2	1.7
	(1$\bar{1}$1) [1$\bar{1}$2]	210.8	108.5	118.9	-2.3	**30.2**	**64.3**	**302.2**	**5.2**
$V_{\varepsilon 4}$	(11$\bar{1}$) [112]	102.5	82.9	282.9	1.2	138.7	96.4	95.0	1.6
	(11$\bar{1}$) [$\bar{2}$1$\bar{1}$]	102.5	82.9	162.9	2.9	138.7	96.4	355.0	-8.3
	(11$\bar{1}$) [1$\bar{2}$1]	102.5	82.9	42.9	-4.1	**138.7**	**96.4**	**215.0**	**6.6**

Source: Own elaboration.

With the application of subsequent cycles (i.e., 2018 cycles), crack propagation and surface relief were observed on the pre-polished sample surface as depicted by arrows in Figure 19(a) and Figure 19(b). The crack propagation followed a zig-zag path, Figure 19(a), along the $\{111\}_{FCC}$ planes. Figure 19(b) reveals that a subdivided FCC phase remained even after HCP-martensite was generated and crack propagation took place. In addition, Figure 19(b) revealed that crack nucleation and propagation occurred at the FCC/HCP interfaces in which the KAM values are higher, Figure 19(c). Specifically, it is possible to note that the orientation variants corresponding to $(11\bar{1})[1\bar{2}\bar{1}]$ ($V_{\varepsilon 4}$) and $(1\bar{1}1)[1\bar{1}\bar{2}]$ ($V_{\varepsilon 3}$) Shockley partials serve as the preferential path for crack propagation, as shown in Figure 19(b) and Table 4.

The Humbert model approach was again applied for the boxed region shown in Figure 19(b). This picture shows an experimentally determined pole figure for the parent-FCC orientation. Its corresponding Euler angles were used to calculate the formation of HCP-variants, with results the presented in Figure 19(f) and Table 4. According to the selection criterion, only the $(11\bar{1})[1\bar{2}\bar{1}]$ orientation variants must be observed. However, all four possible orientation HCP-variants are present, see Figure 19(e). Therefore, the proposed variant selection mechanism, based on the formation of variants with mechanical work within 10% of the highest mechanical work value, does not apply to the studied dynamical loading conditions.

Figure 19 – SEM micrograph (a), IPF map (b), and KAM map (c) of the sample subjected to 2018 loading cycles. (d) and (e) are experimentally determined pole figures from the boxed regions in (b) for the FCC-phase and HCP-phase, respectively. The calculated pole figures of the HCP variants are

presented in (f). (BD = build direction, ND = normal direction, TD = tensile direction)

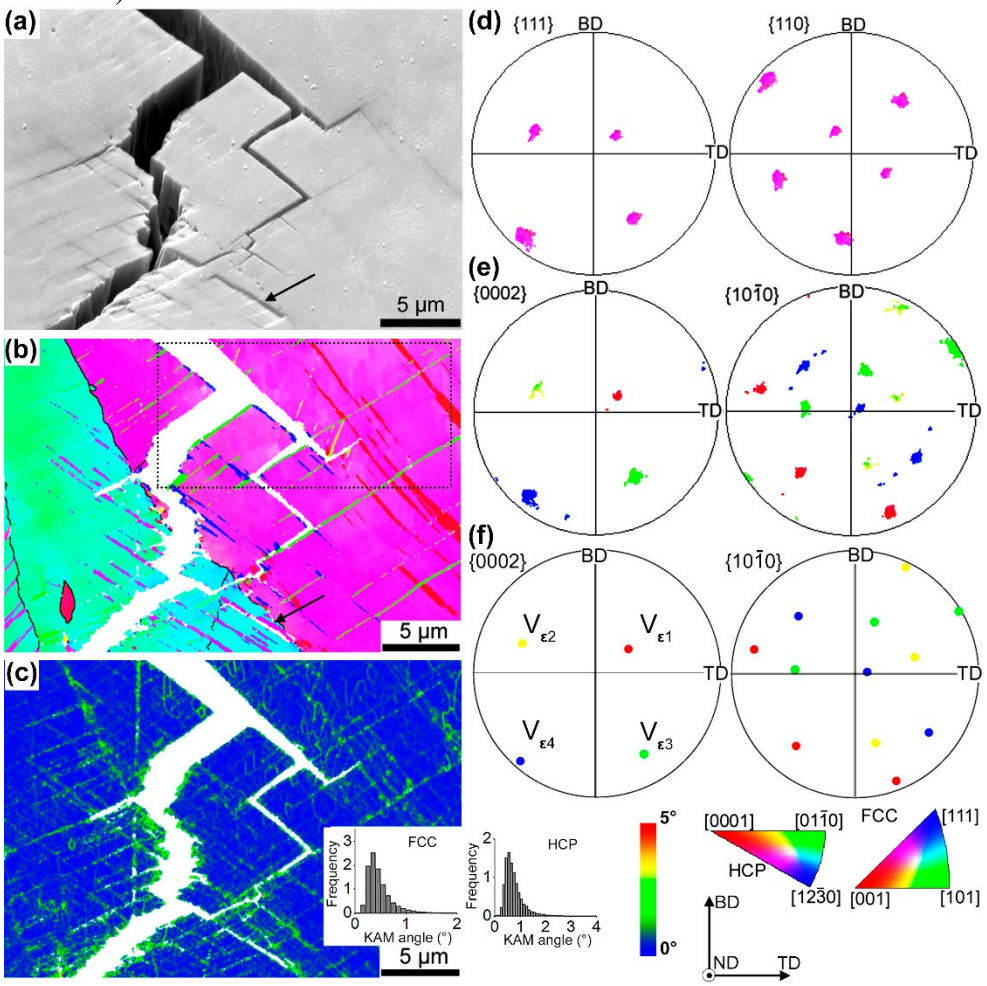

Source: Own elaboration.

3.4.5 Fractographic analysis

The fracture features of the tensile sample are displayed in Figure 20. The image shows dimples that are characteristic of ductile fracture, reflecting the reasonable level of elongation of the material. Spheroidized carbide precipitates (highlighted with red arrows) are randomly distributed in the matrix.

Figure 20 – SEM micrographs of fractured Co-Cr-Mo biomaterial alloy after tensile testing.

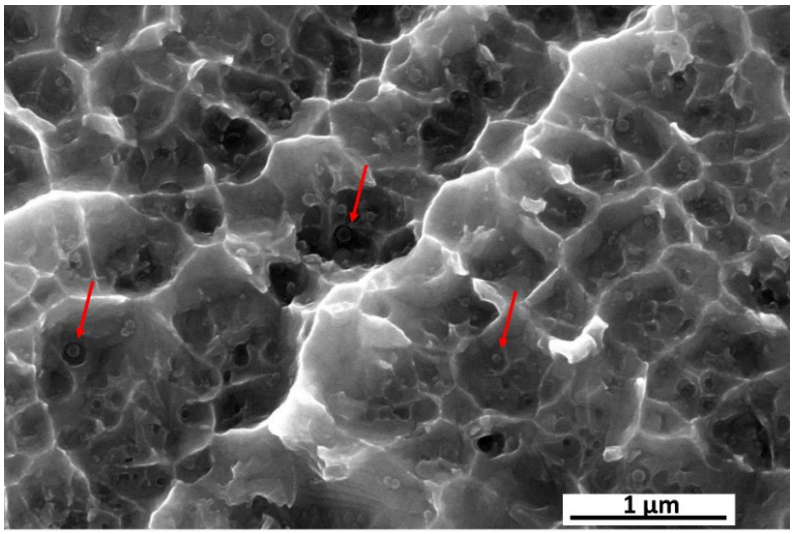

Source: Own elaboration.

After the final sample rupture (2018 cycles), the fractured surface morphology was studied by SEM and the results are shown in Figure 21. One can note the presence of microcracks in Figure 21(a). In addition, it is possible to see some faceted surface regions, depicted by the black arrows, corresponding to brittle fractures at the final stages of the rupture. From the black rectangle in Figure 21(a), one notes the presence of a relief formed by the slip bands corresponding to the {111} habit planes of the DIMT. This is shown in Figure 21(b) by the intersecting black lines and by the black circle. Such a stepwise aspect is a ductile feature possibly formed at the early stages of cyclic loading when HCP-variants are nucleate and grow.

Figure 21 – SEM micrographs of fractured Co-Cr-Mo biomaterial alloy after loading cyclic experiment.

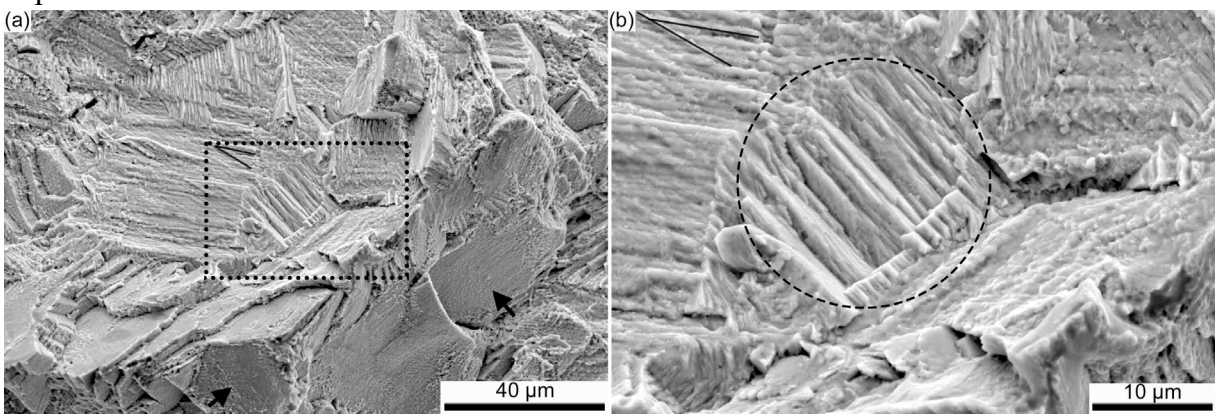

Source: Own elaboration.

3.5 Discussion

Figure 15 and Figure 16 show the typical microstructure of Co-Cr-Mo alloys produced by the L-PBF technique, in agreement with results reported in other studies (CHEN; PHAN; DARVISH, 2017; DA SILVA COSTA et al., 2021; ROUDNICKÁ et al., 2021c; TONELLI, 2021; TONELLI; AHMED; CESCHINI, 2023). Prashanth and Eckert (2017) proposed that the Co-Cr-Mo alloy system can be considered a pseudobinary composed of CoCr and Mo phases. During cooling, the CoCr phase forms from the liquid and ejects Mo (which has low solubility in this system and is not present in sufficient concentration to form another stable phase). Consequently, a dendritic structure forms, with CoCr forming the nuclei and Mo forming the contours. Semiquantitative chemical analysis agrees with this explanation, revealing that the Mo content is higher at the edges of the dendritic structure than at its nuclei (DE CASTRO GIRÃO et al., 2020; ROUDNICÁ et al., 2021a). Additionally, the laser scanning process used in L-PBF leads to the generation of melt-pool boundaries (red dashed lines in Figure 16(a)). Moreover, layer-by-layer production promotes the formation of columnar grains (yellow dashed lines in Figure 16(a)) crossing melt-pool boundaries by the epitaxial growth mechanism (BASAK; DAS, 2016). The interdendritic microsegregation, melt pools, process-induced voids and high residual stresses degrade the fatigue properties of the L-PBF components (ZHANG et al., 2019).

The high cooling rates present in the L-PBF process, 10^5 to 10^6 K/s (PRASHANTH; ECKERT, 2017), result in a high dislocation density and stacking fault (SF) defects (WANG et al., 2021). These microstructural aspects impact the mechanical properties of the as-built alloy. The refined dendritic structure and the high density of defects contribute to the alloy strengthening process (red line in Figure 16). Both mechanisms can be understood based on the Hall-Petch relation, as such microstructural features reduce the mean-free path for dislocation movement. This explanation is consistent with those proposed in the literature to explain the tensile properties (as evidenced by stress-strain curve analyses) of other alloy systems produced by the L-PBF technique (KWABENA ADOMAKO; HAGHDADI; PRIMIG, 2022; ZHAO et al., 2021).

The initial linear increase in strain amplitude values, observed in Figure 17, is presumably caused by the formation of the HCP phase with the progressing number of loading cycles. This is supported by the results presented in Figure 14, where analytically, it is shown that DIMT starts at a strain of 0.036 and stresses over 1175 MPa. The formation of the HCP phase by the DIMT mechanism, Figure 18(a) and Figure 18(b), further supports such behavior

due to the volume change that takes place during displacive FCC → HCP phase transformation, consistent with previously reported research (YAMANAKA; MORI; CHIBA, 2013). Here, the measured macroscopic strain is a sum of the transformation strains of specific martensite variants that are formed during cyclic loading in individual grains with different volume fractions (MIRZAEIFAR et al., 2013).

Figure 18(a) and Figure 18(b) revealed the displacive formation of two HCP-martensite variants originating from the (110) FCC grain. The FCC → HCP phase transition requires shear and shuffle of atoms causing angular distortion to attain the atomic arrangement of HCP basal planes and these atoms are coplanar on the {111} habit plane of the parent FCC-phase (YAMANAKA; MORI; CHIBA, 2013). This phase transformation occurs by the motion of Shockley partials on every second {111} FCC plane (OLSON; COHEN, 1976a) and is possible because the dislocations in the FCC-phase are dissociated into its Shockley partial dislocations in accordance with Yamanaka et al. (YAMANAKA et al., 2014)

$$\frac{a}{2}[\bar{1}01]_{FCC} \rightarrow \frac{a}{6}[\bar{2}11]_{FCC} + SF + \frac{a}{6}[\bar{1}\bar{1}2]_{FCC}, \qquad (1)$$

where a is the lattice parameter and *SF* is the stacking fault. The displacive FCC → HCP is accompanied by an increased dislocation density in the {111}FCC planes (GRAY; WILLIAMS; THOMPSON, 1983). Moreover, the elastic and plastic strains introduced into the FCC matrix through this phase transition affect the mechanical properties of the alloy.

The observed relief, see Figure 19(a), is caused by the intersection of Shockley partials with the surface, leaving behind a slip band. The formation of slip bands acts as the stress concentration factor and serves as the crack initiation site. The zig-zag crack propagation path is a consequence of the DIMT because the orientation of crack propagation changes under identical angles as the orientation divergence between two HCP-variants, see Figure 19(b). This propagation type was reported to increase the fatigue life due to roughness-induced crack closure (GRAY; WILLIAMS; THOMPSON, 1983) and occurred at the FCC/HCP interface which is considered to have a low resistance against brittle fracture (KOYAMA; SAWAGUCHI; TSUZAKI, 2015). As shown in Figure 18(f), the orientation relationship between the FCC-matrix and the formed HCP-martensite at the FCC/HCP interface satisfies the Shoji-Nishiyama condition. Since one of the $\{111\}_{\mathrm{FCC}}$ slip plane is parallel to the $\{0002\}_{\mathrm{HCP}}$ basal slip plane, the dislocation movement on the other $\{111\}_{\mathrm{FCC}}$ planes are suppressed. This gives rise to stress concentration at the FCC/HCP interface, which promotes brittle cracking. Moreover, the atomic

misfit at the FCC/HCP interface acts as a barrier for dislocation motions, generating plastic strain accumulation as indicated by the higher KAM values in these regions, Figure 19(c) and Figure 18(d). A similar mechanism of strain localization, crack nucleation, and propagation has been reported in cast Co-Cr-Mo alloys (KOIZUMI et al., 2013; LEE; MATSUMOTO; CHIBA, 2011; MORI et al., 2010).

In the initial stages of cyclic loading, with the formation of the first HCP variants, Figure 18(b), within the FCC-grain that has the highest Schmid factor, a subdivision of grains takes place, leading to grain boundary strengthening in accordance with the Hall-Petch relationship. The subdivided "hard" grains turn out to be more difficult to deform and plastic deformation can progress on a neighboring "softer" grain. The process of cyclic hardening, the straight line in Figure 17, continues until favorably oriented grains are deformed and HCP variants with the highest mechanical work are formed. Then, the activation of other Shockley partials with lower mechanical energy occurs, leading to the nucleation of other HCP variants, as shown in Figure 19(b). Therefore, the formation of the variants with a lower Schmid factor becomes more prominent with the progressing number of loading cycles.

The distortional variants $(11\bar{1})[1\bar{2}\bar{1}]$ and $(1\bar{1}1)[1\bar{1}\bar{2}]$ were the preferential paths for crack propagation because of their high mechanical work. Therefore, these partials are most prone to glide until encountering some barrier, such that some already formed HCP variants, leading to impingement at the HCP-martensite plates. This is caused by the formation of a sessile dislocation at the intersection line between the planes $(11\bar{1})$ and $(1\bar{1}1)$, according to the reaction

$$\frac{a}{6}[1\bar{2}\bar{1}] + \frac{a}{6}[\bar{1}12] \rightarrow \frac{a}{6}[0\bar{1}1]. \qquad (2)$$

The dislocation formed by this reaction is known as stair-rod dislocation and is sessile because its Burgers vector does not belong to the $(11\bar{1})$ neither to $(1\bar{1}1)$ planes. Therefore, the stair-rod dislocation formed acts as a barrier to the glide of further dislocations on these planes, favoring the stress concentration at the intersection of the distortional variants. This explanation is in accordance with the experimental observation of intersecting stacking faults on a deformed alloy with negative intrinsic staking fault energy (WEI; TASAN, 2020).

A schematic representation of the proposed mechanism is shown in Figure 22(a) and Figure 22(b). Figure 22(a) shows the dissociation of two perfect dislocations on its Shockley partials, and those with high mechanical work are represented by the blue and green

arrows, following the colors shown in Figure 19(b). Therefore, these partials will glide until their intersection at the $[0\bar{1}\bar{1}]$ intersection line between planes $(11\bar{1})$ and $(1\bar{1}1)$, resulting in sessile dislocation, as represented in Figure 22(b).

Figure 22 – Schematic representation of the formation mechanism of sessile dislocations due to the interaction of the $[1\bar{2}\bar{1}]$ and $[\bar{1}12]$ Shockley partials before (a) and after (b) deformation. Bright-field TEM micrographs of the as-built (c) and fractured (d) samples.

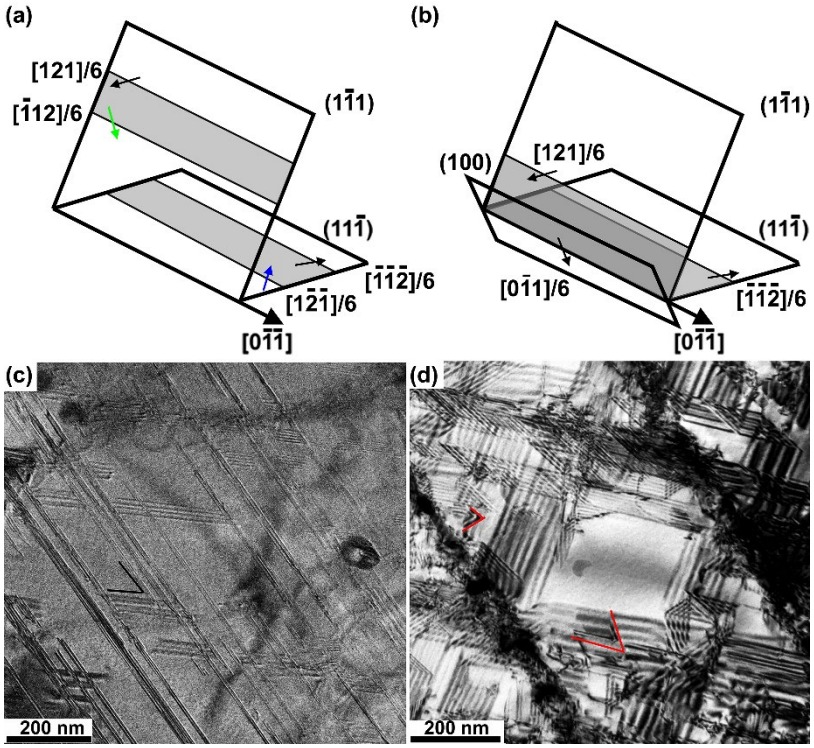

Source: Own elaboration.

Experimental evidence of all these features is shown in Figure 22(c) and Figure 22(d). For the as-built sample, bright field TEM micrographs showed the presence of {111} faulting planes, which appear as bands with fringe contrast and are represented by the black lines in Figure 22(c). Therefore, the perfect dislocations are dissociated, according to the representation in Figure 22(a). Near the surface fracture, it is possible to observe the increase in the stacking fault density, see Figure 22(d). In addition, one can note the formation of wedge-shaped morphological features, such as those depicted by the red lines in Figure 22(d). Such aspect corresponds to intersecting stacking faults and is possibly a consequence of the bidimensional projection of the configuration represented in Figure 22(b). Therefore, TEM observations corroborate the formation of sessile dislocations at the intersecting lines of the

Shockley partials from different {111} planes. This phenomenon has also been observed for other deformed Co-Cr-Mo alloys (PETROV et al., 2016; YAMANAKA; MORI; CHIBA, 2012). Additionally, Yamanaka et al. (YAMANAKA; MORI; CHIBA, 2012) associated extra lattice distortion during deformation due to the presence of sessile dislocation, further supporting the explanation for the observed path crack.

Although the observed good coincidence of the calculated pole figures with those experimentally obtained, both for the sample subjected to 300 cycles (Figure 18(f) and Figure 18(g)) and to 2018 cycles (Figure 19(e) and Figure 19(f)), Humbert's model does not apply due to the nonuniform stress distribution inside the grains when the most favorable HCP-variants have already nucleated. This model considers that the identical uniaxial macroscopic stress tensor is applied to both original grains and partitioned grains. An additional reason for this can be inhomogeneous stresses arising from geometric constraints near the boundary or the local stress resulting from the martensite plates in the adjacent grain impinging on the grain boundary causing the formation of all variants (ZHANG et al., 2011).

3.6 Conclusions

The effect of FCC → HCP phase transformation on crack propagation during cyclic loading of Co-28Cr-6Mo biomaterial alloy produced via the L-PBF route was analyzed. The following conclusions are drawn:

- The linear increase in plastic strain during the first loading cycles is attributed to the transformation volume change during displacive FCC → HCP phase transformation and subsequent volume fraction increase of the HCP phase.
- The presence of slip incompatibility at FCC/HCP interfaces causes localized accumulation of plastic strain which promotes crack nucleation.
- The crack proceeds along the FCC/HCP interfaces causing the formation of a zig-zag propagation path which decreases the crack growth rate. In particular, the HCP-variants $(11\overline{1})[1\overline{21}]$ and $(1\overline{1}1)[1\overline{12}]$ with high mechanical work are most prone to the crack propagation.
- Humbert's model used in this work was not able to predict the martensite variant selection mechanism during cyclic loading. The reason for this has not yet been

elucidated. Therefore, further work is needed to develop a variant selection model that takes into account plastic strain accumulation during dynamic loading conditions.

4 EFFECT OF CYCLIC LOADING ON MICROSTRUCTURE AND PLASTIC DEFORMATION IN A REVERSE TRANSFORMED Co–28Cr–6Mo ALLOY FABRICATED VIA LASER POWDER BED FUSION

4.1 Abstract

We present a systematic microstructure-oriented plasticity investigation of an additively manufactured cobalt-based alloy. A load-controlled cyclic test in the low-cycle fatigue regime was utilized to study the mechanical response and microstructural evolution of the heat-treated material. Through *in situ* synchrotron X-ray diffraction combined with electron backscatter diffraction, and scanning electron microscopy, deformation-induced FCC → HCP phase transformation and kinetics of transformation are revealed. It was found that a stepwise increase in plastic deformation is attributed to nucleation and growth of different martensitic crystallographic variants. These insights on plasticity and microstructural changes provide hints for possible approaches that lead to improved fatigue resistance of the alloy.

Keywords: Co-Cr-Mo alloy; Laser powder bed fusion; Deformation-induced martensitic transformation; Variant selection; Reverse transformation.

4.2 Introduction

Cobalt-based alloys are extensively employed for metal-on-metal total hip and knee arthroplasties due to the low wear of the articulating surfaces (HERMAWAN; RAMDAN; P. DJUANSJAH, 2011). Despite the low wear rate and debris volume, the metal ions release, and formation of micro/nanoparticles is one of the key failure factor, limiting the lifetime of the implant. Bijukamar et al. (2018) reported that release of metal ions and particles can trigger adverse reactions in human body including vasculitis, osteolysis and necrosis. Therefore, there is a constant strive for reduction of the debris at the sliding (HASTIE et al., 2021; NAWABI et al., 2014). This can be achieved, for example, through production of joints with textured surfaces that can store debris (LIU et al., 2023). Another approach is mitigation of mechanisms that contribute to the debris formation. One of these mechanisms is the stress concentration at intrusions/extrusion formed by cyclic loading conditions (STEPHENS et al., 2000). Therefore, understanding the evolving nature of microstructural aspects associated with

intrusions/extrusions is a fundamental step toward further reduction of debris formation that takes place during cyclic loading conditions.

In cobalt-based alloys extrusions/intrusions are readily formed when the gliding of dislocations at the HCP-martensite reaches the free-surface (MITSUNOBU et al., 2014). The formation of HCP-martensite takes place via deformation-induced martensitic transformation (DIMT) mechanism. This transformation occurs through the dissociation of dislocations into Shockley Partials (SP) in the $\{111\}_{FCC}$ planes (CAYRON, 2016). This dissociation creates HCP structure along a few atomic planes and, when stress is applied, the stacking faults (SF) generated have the necessary size to act as nucleation sites for HCP-martensite (KOIZUMI et al., 2013). Such phase transition is possible due to the low stacking fault energy of the alloy (i.e., < 15 mJ/m^2 at room temperature (PARK et al., 2022)).

An intrinsic characteristic of this displacive DIMT, is the possibility of attaining the geometrical restrictions associated with the transformation for any one of the four $\{111\}_{FCC}$ planes and their corresponding three $<110>_{FCC}$ directions. Consequently, it is possible to form twelve distortional crystallographic HCP-variants. However, due to the sixfold rotational symmetry of the HCP basal planes, the three different $<110>_{FCC}$ directions give rise to HCPs with the same orientation, resulting in four orientational HCP-variants.

The susceptibility of the FCC matrix to DIMT is determined, from a thermodynamic perspective, by the superficial energy of the HCP/FCC interface and by the difference in Gibbs free energy between the two phases. However, a reduction in grain size contributes to increased mechanical stability (HAN et al., 2015; LEE et al., 2021). Takaki, Nakatsu, and Tokunaga (1993) elucidated that the critical grain size for matrix stabilization depends on the elastic stress field at the tip of the growing HCP-martensite lath. Thus, stabilization occurs when the FCC grain size is small enough to prevent martensite growth before the elastic stresses induce branching into the other available $\{111\}_{FCC}$ planes.

Moreover, a decrease in the FCC grain size in the alloy of concern leads to an extension in fatigue life (WEI et al., 2018). In this study, a decrease of the grain size from 108 μm to 24 μm resulted in an increase in fatigue life from 113 cycles to 4462 cycles (WEI et al., 2018). Such grain size reduction was achieved through a reverse transformation heat treatment. The procedure consists of two-steps heat treatment. In the first stage, isothermal heat treatment is applied, where FCC → HCP phase transformation takes place. In the second stage, the formed HCP-martensite is reverted back into the FCC-phase during solution annealing. This approach

increases the number of available nucleation sites compared to the microstructure before aging, thereby reducing the grain size.

Recently, *in situ* synchrotron X-ray diffraction investigations of FCC → HCP phase transformation in Co-Cr-Mo alloy systems were conducted (ANTUNES et al., 2023; CAI et al., 2018; WEISSENSTEINER et al., 2019). This advanced technique enables to follow microstructural evolution including volume phase fraction (MENG et al., 2020; ZHANG et al., 2023), defect density (ALKHAZRAJI et al., 2014; PRASAD et al., 2021; ZHONG et al., 2015), and crystallographic texture (BENATTI et al., 2022; LONARDELLI et al., 2005; LUTTEROTTI; VASIN; WENK, 2014). This is possible because a two-dimensional area detector allows fast acquisition of full Debye–Scherrer patterns. In addition, this technique has enabled to understand how DIMT impacts the low-cycle fatigue behavior of stainless steels (SCHOELL et al., 2022).

Additive manufacturing techniques, such as laser powder bed fusion (L-PBF), can be used to produce cobalt-based alloys with enhanced fatigue resistance compared to the same alloys produced by casting (DONG et al., 2020). Thus, combining additive manufacturing with reverse transformation heat treatment offers a promising route for production of reliable joint implants. In this regard, the comprehension of effect of deformation-induced martensitic phase transformation on the deformation process and failure mechanisms is crucial in production of damage-tolerant components.

Therefore, in the present work, we investigate additively manufactured Co-28Cr-6Mo alloy subjected to cyclic loading tests. A combination of *ex situ* electron backscatter diffraction and *in situ* synchrotron X-ray diffraction allowed us to elucidate effect of microstructural changes and formation of martensitic crystallographic variants on deformation behavior. Our results indicate that a stepwise increase in plastic deformation occurs exclusively via nucleation and extension of martensitic phase. Possible microstructural design measures that could potentially enhance fatigue life of the alloy of concern are also discussed.

4.3 Materials and methods

4.3.1 Material

Specimens with cross-section of 2.7 × 1.1 mm^2 and a 4 mm gauge length were additively manufactured via laser powder bed fusion (L-PBF) process using an EOSINT 280

machine (EOS GmbH) fitted with an ytterbium laser. The MP1 metallic powder feedstock, specified according to the EOS GmbH manufacturer's catalog (EOS, 2011), was utilized. The production parameters are summarized in Table 5.

Table 5 – L-PBF process parameters used.

Nominal laser power (W)	Scanning speed (mm/s)	Laser spot (µm)	Layer thickness (µm)	Hatch spacing (µm)
200	800	100	40	~90

Source: Own elaboration.

The chemical composition of the as-built sample, Table 6, was determined using the following techniques:

- X-ray fluorescence spectroscopy (PANalytical Axios): for the metallic elements;
- Combustion infrared absorption analysis (LECO CS844): for carbon;
- The inert gas fusion analysis (LECO TC400): for nitrogen.

Table 6 – Chemical composition of the as-built Co-28Cr-6Mo alloy (wt.-%).

Cr	Mo	Mn	Si	Fe	Ni	C	N	Co
27.89	6.27	0.72	0.62	0.32	0.1	0.14	0.14	Bal.

Source: Own elaboration.

4.3.2 Heat treatment

The as-built material was submitted to a reverse transformation heat treatment in a muffle furnace. The schematic representation of the applied heat treatment and calculated phase diagram using Thermo-Calc software are shown in Figure 23(a) and Figure 23(b), respectively. The heat treatment was composed of the following stages:

(1) Solution annealing was performed at 1150 °C for 1 hour.

(2) Aging treatment was applied at 800 °C for 24 hours.

(3) Reverse transformation (RT) was applied at 1150 °C for 15 minutes.

Each of these stages was followed by water quenching (WQ).

Figure 23 – Schematic representation of the heat treatment utilized (a). Phase diagram of the Co-28Cr-6Mo-0.14C-xN (wt.-%) alloy obtained using Thermo-Calc software (b).

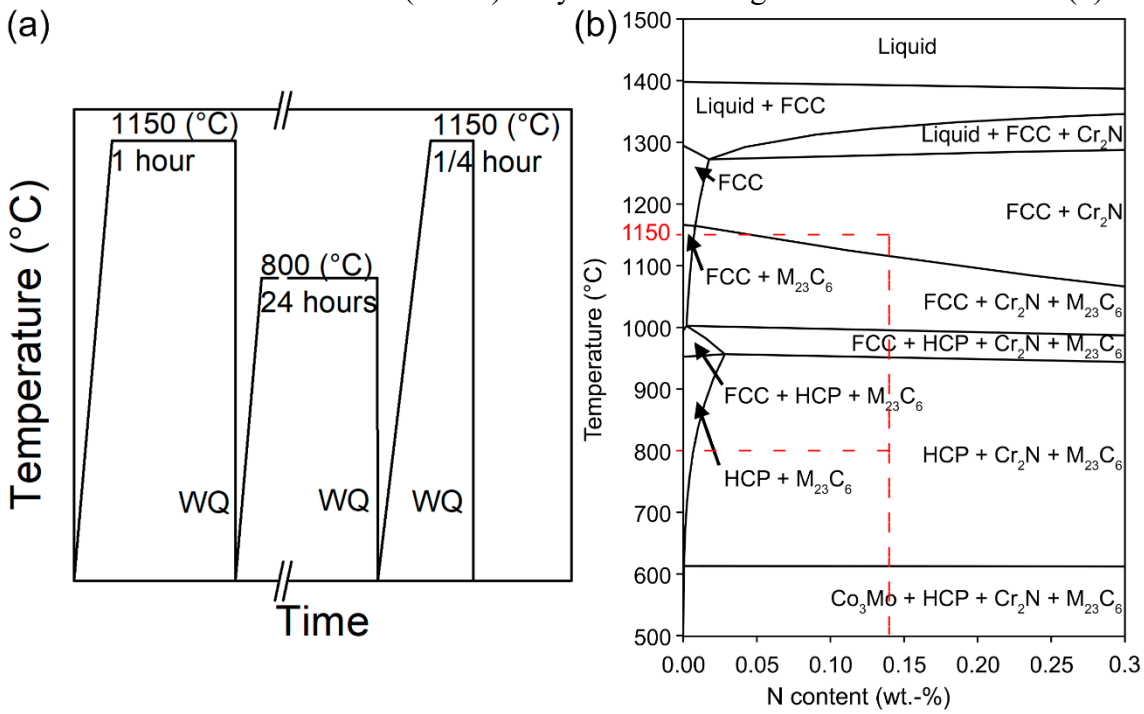

Source: Own elaboration.

4.3.3 *Microstructural characterization and mechanical testing*

A metallographic preparation was carried out in a way that avoided the formation of martensite induced by deformation resulting from the grinding and manual polishing processes. This was achieved by electropolishing using a solution of perchloric acid (10 vol.-%) in acetic acid applying a voltage of 13.5 V in a Struers Letropol-5 machine. The temperature of the electrolyte was approximately 18 °C.

For microstructural characterization, FEI Quanta 450-FEG and FEI Quanta 650-FEG scanning electron microscopes were used. Here, secondary electrons (SE) imaging in addition to electron backscatter diffraction (EBSD) were utilized. The SE image acquisition employed the following settings: an acceleration voltage of 15 kV and a working distance of 15 mm. The EBSD maps were acquired using an acceleration voltage of 15 kV, working distance ranging from 15 mm to 17 mm, and step size of 0.08 µm. The Channel5 program was employed to process the collected data. The standard intercept method was used for determining the average grain size following the ASTM E112 standard.

A transmission electron microscopy (TEM) study was conducted on a solution-treated specimen. Disc-shaped samples were punched out from electrolytically thinned foils,

which were approximately 50 μm thick. Subsequently, these discs were electropolished to achieve electron transparency using a Struers Tenupol-3 apparatus utilizing the electrolyte mentioned above. A JEOL 2100F transmission electron microscope operating at 200 kV was used in high-angle annular dark-field scanning transmission electron (HAADF-STEM) mode. Energy-dispersive X-ray spectroscopy (EDS) point analysis was carried out using a 30 mm^2 silicon drift energy dispersive X-ray detector.

A reverse treated dog-bone shaped specimen with cross-sections of 5.19 × 1.92 mm^2 and 32 mm gauge length was subjected to a monotonic tensile test at a constant crosshead speed of 0.5 mm/min. using an MTS Landmark tensile test machine. True stress-true strain curve was plotted, and the mechanical properties were determined.

4.3.4 Synchrotron X-ray diffraction experiment

Synchrotron X-ray diffraction (SXRD) experiments were conducted on tensile test specimens that were extracted using wire electric discharge machining, with nominal dimensions shown in Figure 24(a). The *in situ* SXRD experiments were carried out at the P07 High-Energy Materials Science synchrotron beamline located at the Deutsches Elektronen-Synchrotron, Hamburg/Germany. The experiment was carried out in transmission mode using energy of 86 keV (corresponding to wavelength: 0.144167 Å) with a 0.7×0.7 mm^2 beam dimension. A Perkin Elmer amorphous silicon two-dimensional (2D) detector with pixel resolution of 2048×2048 was used. The calibration of the experimental setup (detector to sample distance equal to 1223 mm) was carried out using the LaB_6 powder standard (NIST SRM660a). The experimental setup used is presented in Figure 24(b).

Figure 24 – Dimensions of the tensile coupons, showing the regions where the analyses were carried out (a). Schematics of the experimental setup and the reference system used for the *in situ* SXRD experiments (b). Example of the 2D pattern acquired and the caking procedure used to obtain the 1D diffractograms (c). An example of one-dimensional diffraction pattern, showing the observed data and the results from refinement by the Rietveld method (d). (BD = build direction, ND = normal direction, and LD = loading direction).

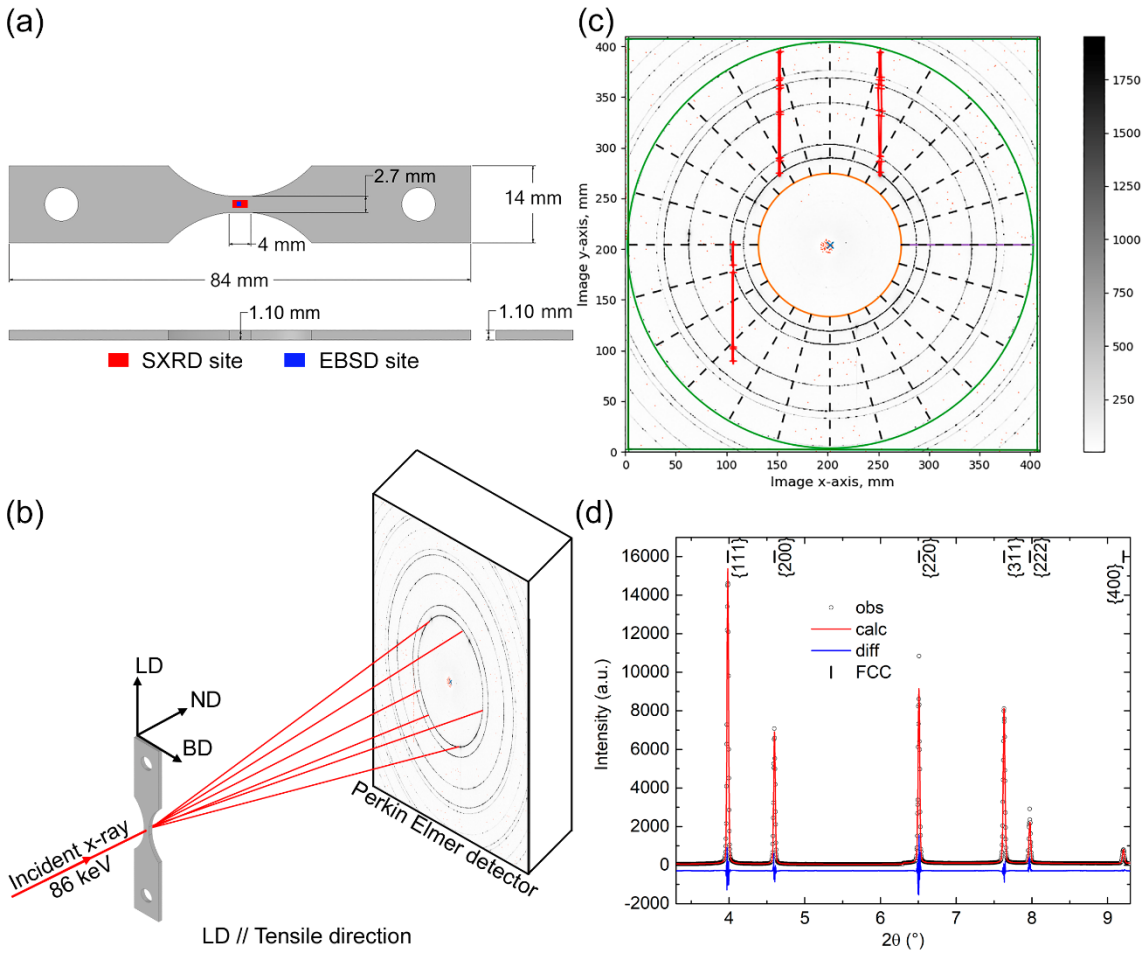

Source: Own elaboration.

Tensile test specimens were mounted in a load frame integrated within the SXRD beamline and cyclic loading tests were carried out at room temperature. The mechanical testing machine operated in force control mode with a load amplitude from 40 N to 2.1 kN. During mechanical tests, 2D diffraction patterns were acquired using an exposure time of 5 seconds.

The SXRD data acquired with progression of plastic deformation was analyzed by sequential Rietveld refinement to follow the microstructural changes in the specimens. Figure 24(c) shows an example of the 2D pattern obtained prior to loading. The refinement by the Rietveld method was carried out using GSAS-II software (TOBY; VON DREELE, 2013). Here, masks were initially applied to remove outlier pixels, and red lines and green square are shown in Figure 24(c). Subsequently, the cakes along which the integration is carried out to obtain the 1D patterns, such as the one shown in Figure 24(d), were defined. Then, an integration along each of the 24 azimuthal angles is performed. The Rietveld approach that refines the preferred orientation, is applied to determine the pole figures from the intensity changes along the azimuthal angles. These data were exported from the GSAS-II program and converted to

postprocessing using the LABOTEX (PAWLIK; OZGA, 1999) and MTEX (BACHMANN; HIELSCHER; SCHAEBEN, 2010) software packages to calculate the Orientation Distribution Function (ODF) and to plot pole figures.

The relative phase fractions of the FCC and the HCP phases were determined considering the Fm-3m and the P 63/mmc space groups, respectively. The refinement sequence was as follows: unit cell, scale factors, spherical harmonics preferred orientation coefficients, and, as the last refinement step, zero correction. The background was fitted using the Chebyschev-1 function. To adjust the sample's coordinate system to the goniometer coordinate system, the sample orientation angles of the GSASII software were set to (Ω, X, Φ) = (0°, 90°, 90°), according with the geometric representation shown in Figure 13.

4.3.5 Variant formation analysis

The variant selection analysis was conducted in accordance with Humbert's approach (HUMBERT et al., 2007). According to this method, the formation of crystallographic variants is based on the distinct levels of mechanical work associated with each variant. In line with this, the mechanical work is equal to the area under the elastic portion of the stress vs. strain curve, specifically $(1/2)\sigma \cdot \varepsilon$, where σ represents stress, and ε denotes the transformation strain of each HCP crystallographic variant. In this analysis, mechanical work was computed following elasticity theory, with both stress and transformation strain tensors expressed in the macroscopic reference frame.

The analysis was carried out with $||\sigma||$ set at 100 MPa, and a severity factor of 0.9 was considered. Hence, the selected variants might be those with mechanical work greater than 90% of the highest mechanical work.

4.4 Results

4.4.1 Microstructural characterization after reverse transformation heat treatment

Figure 25 shows the microstructure obtained after the reverse transformation (RT) heat treatment. From the EBSD inverse pole figure map, Figure 25(a), it is possible to observe equiaxed FCC grains with annealing twins. The kernel average misorientation (KAM) map, Figure 25(b), shows values lower than 1°, indicating a fully recrystallized microstructure. In

addition, it is possible to note an inhomogeneous grain size distribution. The mean lineal intercept was 16.2 µm with a standard deviation of 14.1 µm, Figure 26, corresponding to an ASTM grain size number of 8.6.

Figure 25 – EBSD inverse pole figure map showing the equiaxed FCC grains after reverse transformation heat treatment and annealing twin boundaries (maroon lines) (a). Corresponding KAM map (b). (BD = build direction, ND = normal direction, and LD = loading direction).

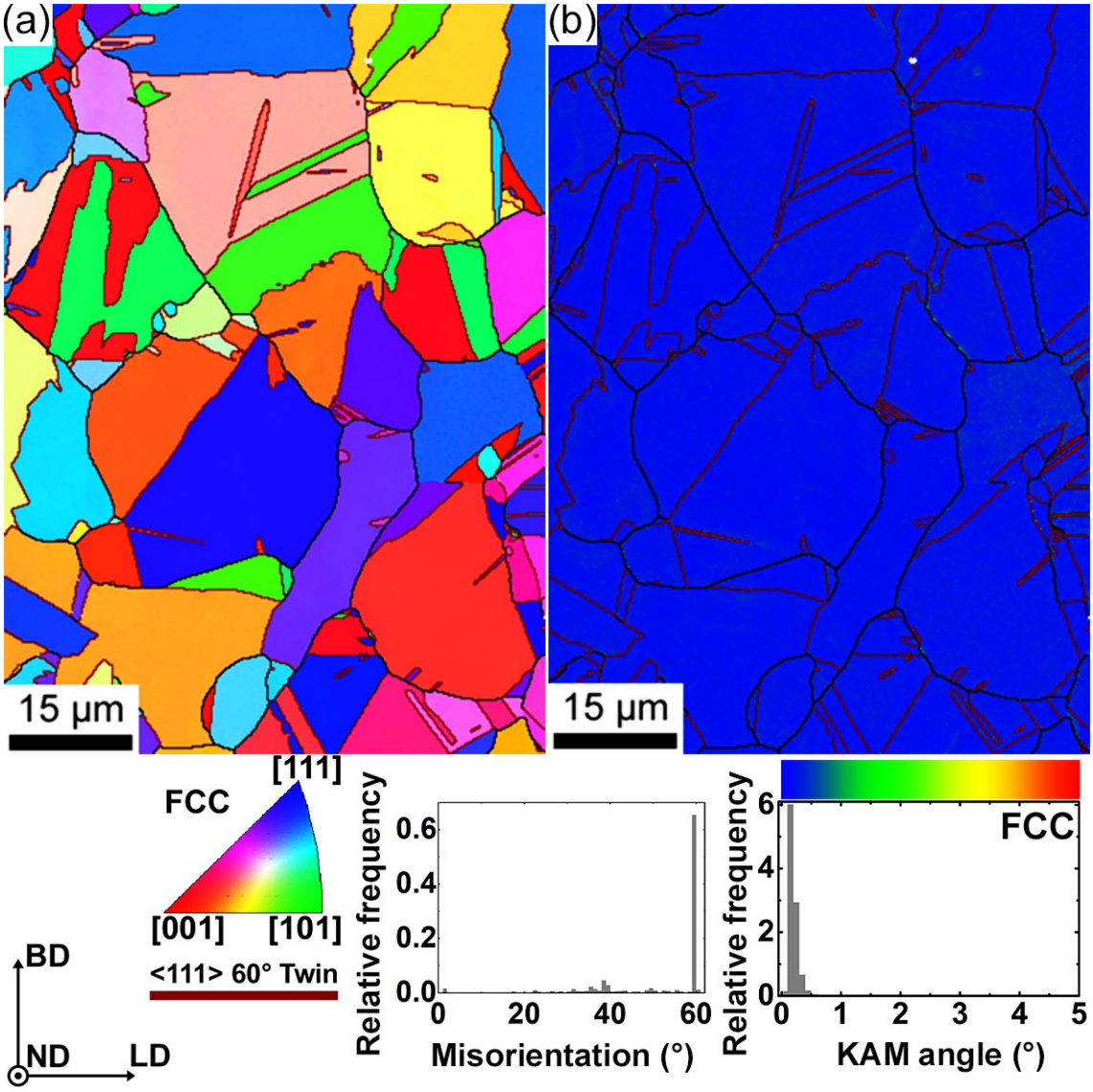

Source: Own elaboration.

Figure 26 – Results from the standard intercept method for determination of average grain size. Note that twin boundaries were not considered in the analysis.

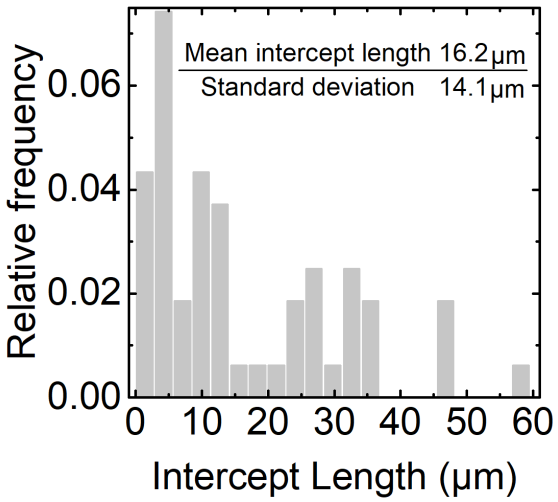

Source: Own elaboration.

4.4.2 Mechanical properties and fractographic analysis

Figure 27 show the true stress-true strain curve of the reverse treated sample along with the strain hardening rate (θ). The 0.2% proof stress and the ultimate tensile strength obtained were 645.8 MPa and 1069.2 MPa, respectively. The measured total elongation at fracture was 13%. Please note that the determined yield strength is lower than the engineering stress applied during the cyclic loading test, i.e., 707 MPa. Consequently, the sample undergoes plastic deformation in each cycle. The strain hardening rate curve reveals two hardening stages. During the first one, marked as I, it is possible to observe a sharp decrease in θ until true strain equal to 0.01. Then, the stage II corresponds to a slight decrease in θ followed by a nearly constant value until the failure at 0.13 true strain. The hardening behavior observed during the stage I is presumably dominated by multiplication of Shockley partials. The stage II, in turn, is possibly dominated by the formation of HCP-martensite.

Figure 27 – True stress-true strain curve of the reverse treated alloy and corresponding strain hardening rate (θ).

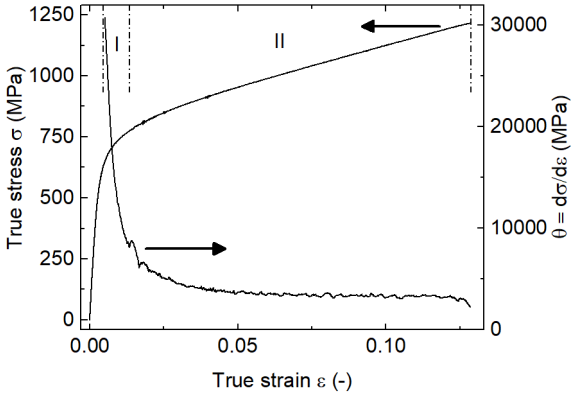

Source: Own elaboration.

Figure 28 shows the fracture surface of specimen after the tensile test. The fracture surface exhibits dimples which is characteristic for ductile fracture. Notably, precipitates, highlighted by red arrows, are randomly distributed in the FCC matrix with an approximate size of 200 nm. It is possible to observe that some precipitates remained inside the dimples. The dimples' formation occurs through void nucleation and growth around the precipitates that are harder than the FCC matrix. Therefore, the size and distribution of these precipitates will affect the alloy ductility because the fracture will occur when the voids link to each other.

Figure 28 – Secondary electron SEM micrograph of fractured sample after tensile test.

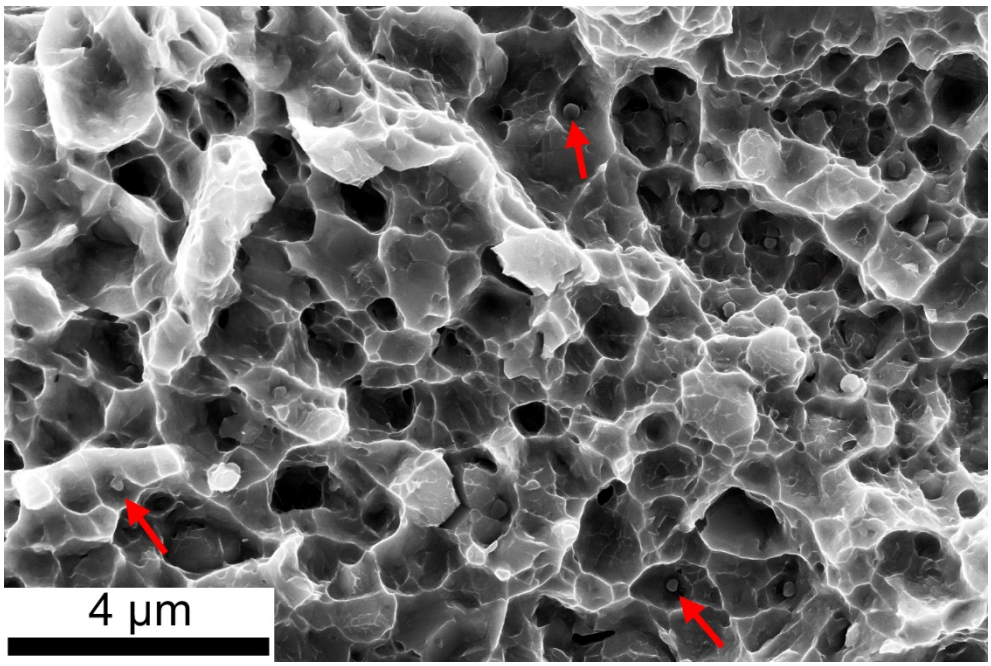

Source: Own elaboration.

4.4.3 In situ synchrotron X-ray diffraction

Figure 29 presents the diffraction pattern and the corresponding refinement using the Rietveld method applying the first tensile cycle. Figure 29(a) shows the initially obtained experimental and calculated intensities versus 2θ (degrees). From the Rietveld method, an initial lattice parameter of 3.5911(41) Å for the undeformed FCC phase (ICSD reference code 52934) was determined. The weighted-profile error value obtained was 7.5% and the results presented through this work were obtained from Rietveld refinements with weighted-profile error close to this value. Figure 29(b) shows a magnified view of the experimental measurement presented in Figure 29(a). Here, it is possible to identify secondary phases attributed to $Cr_{23}C_6$ (ICDD reference code 01-085-1281) and Cr_2N (ICDD reference code 00-035-0803). Due to their low relative phase fraction, the Rietveld method was not applied to these phases, but the identification was possible on the basis of the peak position and lattice parameter. The $Cr_{23}C_6$ phase is present presumably because the solution annealing was not sufficient to attain the thermodynamic equilibrium condition needed for complete dissolution of this phase. The presence of Cr_2N is indeed indicated by the calculated alloy phase diagram, as shown in Figure 23(b).

Figure 29 – Synchrotron X-ray diffraction measurement with corresponding refinement by the Rietveld method (a). Magnified section of the experimental measurement (b).

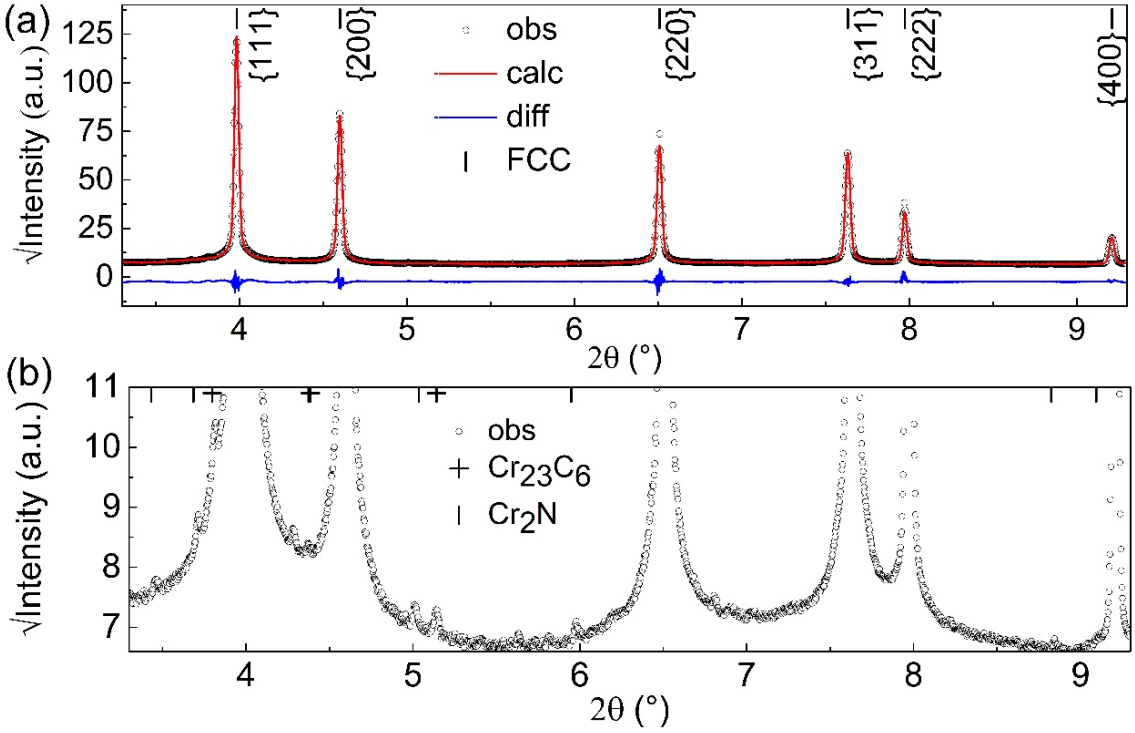

Source: Own elaboration.

Figure 30 shows the mechanical response to the cyclic loading using load frame integrated within the SXRD beamline that operated in the force control mode. By means of the engineering stress versus engineering strain curve, one can observe that the application of the first cycle caused plastic deformation because the applied engineering stress is above the 0.2% proof stress, as shown in Figure 27. The strain hardening of the alloy, with the application of subsequent cycles, can be qualitatively observed by means of the increase in the slope of the plastic portion of the curve.

Figure 30 – Engineering stress-strain curves obtained during force-control tensile cyclic loading. The applied minimum and maximum engineering stresses are depicted by horizontal lines.

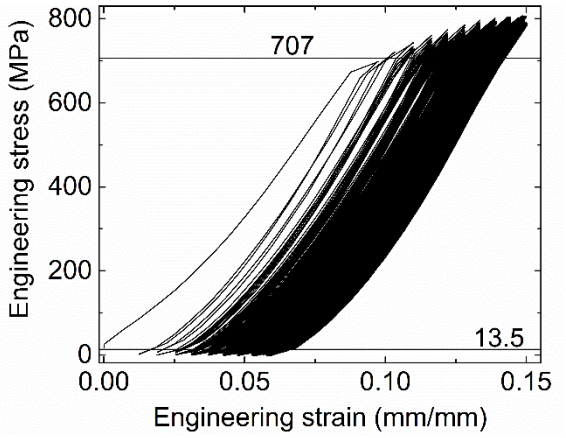

Source: Own elaboration.

Figure 31 shows the *in situ* SXRD data obtained during the cyclic loading test. This color map shows the cycle-resolved peak intensity in the 2θ range of 3.5° - 5°, covering two peaks for both FCC and HCP phases. In this figure, the diffracted intensity is represented by the color range from the lowest intensity (dark blue) to highest intensity (red). Here, it is possible to observe that prior to the cyclic loading, only the $\{111\}_{FCC}$ and $\{200\}_{FCC}$ diffraction peaks are present. With an increased number of applied cycles, the $\{10\bar{1}0\}_{HCP}$ and $\{10\bar{1}1\}_{HCP}$ diffraction peaks attributed to the HCP-phase (ICSD reference code 53806) appear. It should be noted that $\{10\bar{1}0\}_{HCP}$ reflection has lower intensity than $\{10\bar{1}1\}_{HCP}$ diffraction peak because deformation-induced HCP-phase nucleates with preferential orientation. One can also note that these peaks' intensities increase until approximately 1000 cycles and then remain constant.

Figure 31 – Cycle-resolved synchrotron X-ray diffraction peaks revealing the formation of the HCP-phase.

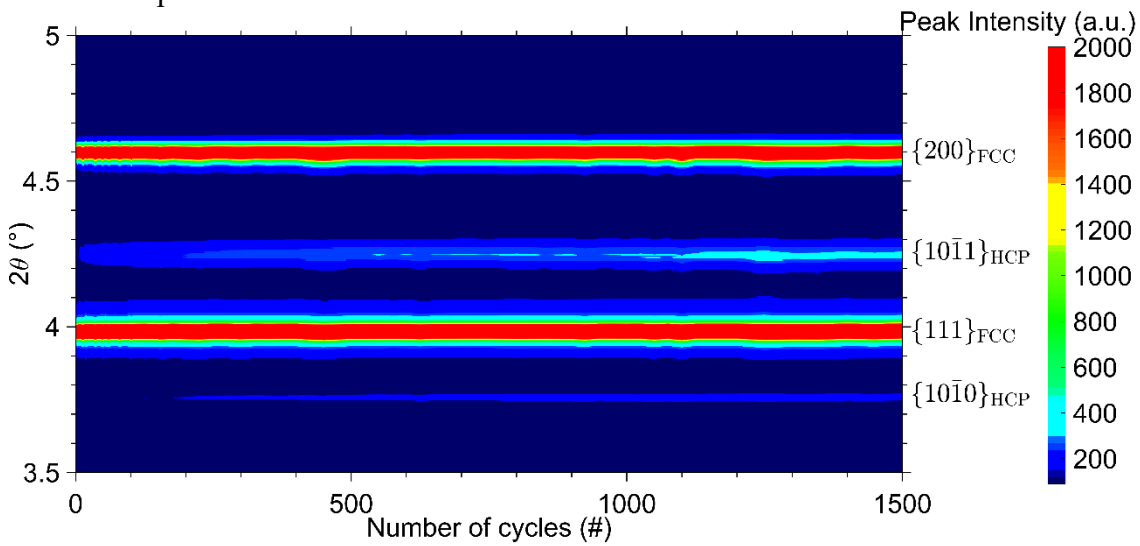

Source: Own elaboration.

Figure 32 shows the engineering strain and relative HCP-phase fraction, obtained from the refinement by the Rietveld method, plotted against the number of cycles. A stepwise increase in the engineering strain with progressing number of applied cycles is accompanied by a gradual increase in the relative HCP-phase fraction. Hence, the deformation-induced FCC → HCP phase transformation causes the observed plastic deformation. For example, it is possible to observe a nearly stable HCP fraction (~3.9 %) between 200 and 300 cycles, and a stable value of the engineering strain (~0.048 mm/mm). When the HCP fraction changes to ~4.5%, there is also an increase in the engineering strain (~0.054 mm/mm).

Figure 32 – Evolution of the engineering strain as function of number of loading cycles (a). Evolution of the relative HCP fraction as function of number of loading cycles (b).

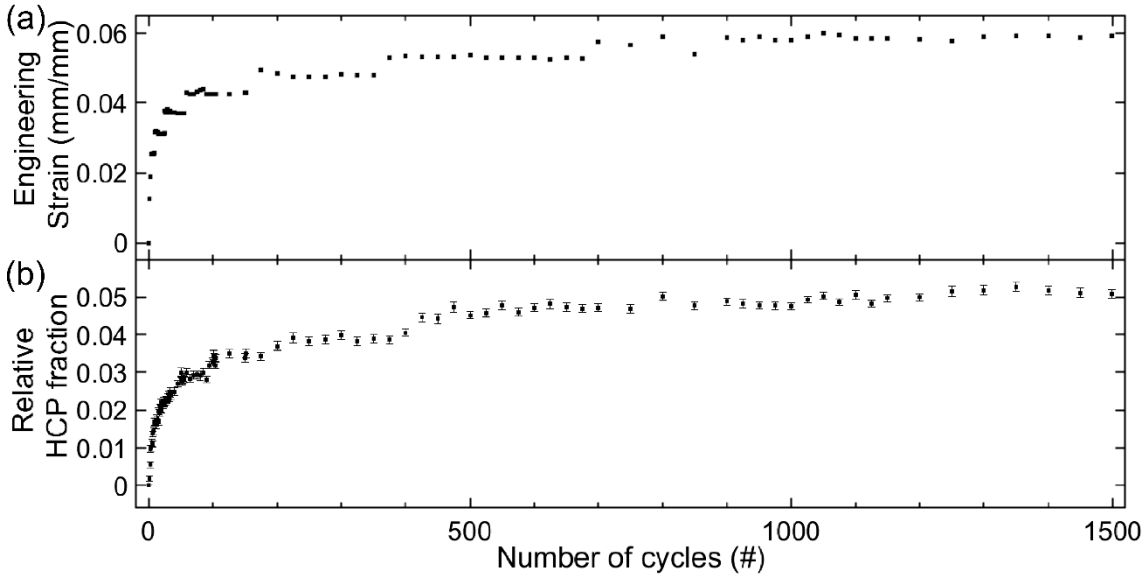

Source: Own elaboration.

Figure 33 shows the strain hardening rate (θ), which was calculated as the slope of the plastic portion in the true stress vs. true strain curve, plotted against the relative HCP fraction. This figure shows that as the relative HCP fraction increases, with the progression of cyclic loading and the strain hardening rate also increases. Therefore, the formation of the HCP-phase contributes to alloy hardening.

Figure 33 – Strain hardening rate as a function of corresponding relative HCP fraction.

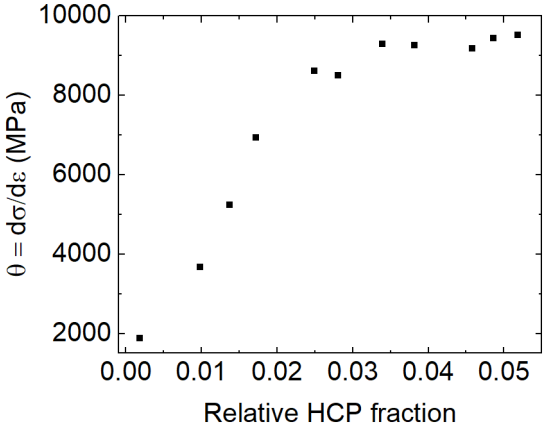

Source: Own elaboration.

The relative full width at half maximum (FWHM) was calculated by dividing the FWHM by the respective plane spacing (GONG et al., 2023). This parameter can be used to qualitatively investigate the behavior of the crystallographic defects during plastic deformation.

Figure 34 shows these results for both the FCC and HCP phases. Please note that for the FWHM analysis the HCP phase was considered only in range the from 300 to 1500 cycles because of its low relative fraction. In this figure, it is possible to observe that both the initial value and the absolute increase in the relative FWHM of $\{311\}_{FCC}$ crystallographic planes were the highest. With the progression of plastic deformation, more cycles are needed to produce the same increase in the relative HCP fraction. For example, 16 cycles are sufficient to produce ~2% of the HCP-phase, but 225 cycles are needed for a twofold increase and reaches only ~5% after 1500 cycles, Figure 32. The relative FWHM exhibits the same behavior, Figure 34. Here, the $\{311\}_{FCC}$ crystallographic plane shows a stepwise increase similar to that observed for the HCP relative fraction. In addition, the increase in the relative FWHM of the $\{10\bar{1}0\}_{HCP}$ and $\{10\bar{1}1\}_{HCP}$ crystallographic planes indicates defects accumulation, which is more pronounced with progressing number of applied cycles. Therefore, cyclic loading induces an increase in the density of crystallographic defects both in the FCC-matrix and in the HCP-phase. In addition, it is not possible to observe a reduction in the relative FWHM with rise of HCP-phase fraction.

Figure 34 – Cycle-resolved relative FWHM of the FCC-phase (black) and that of HCP-phase (gray).

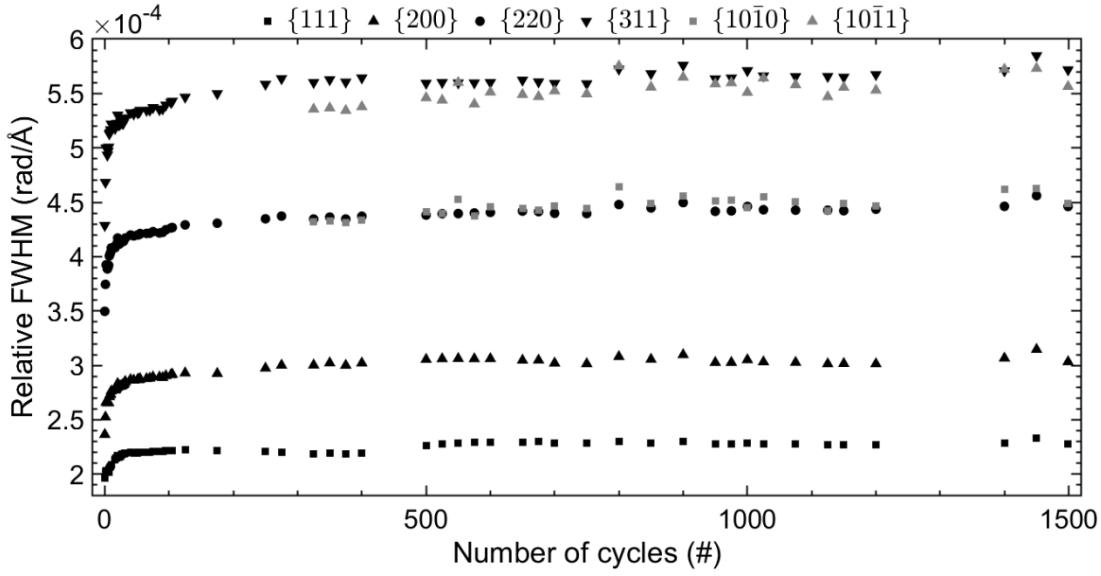

Source: Own elaboration.

4.4.4 Postmortem microstructural characterization

Figure 35 shows the postmortem characterization realized after the application of 1500 cycles. Figure 35(a) shows the SE micrograph where it is possible to observe the formation

extrusion and intrusions caused by the intersection of Shockley partials with the free surface. Figure 35(b) shows that HCP-martensite nucleation occurred at these deformation bands, supporting that cyclic loading cause formation of the HCP-phase by the DIMT mechanism. Figure 35(c) shows the inverse pole figure map for both the FCC and HCP phases. The annealing twin boundaries are observed to act as nucleation sites for the HCP-phase, as shown by the red arrows in Figure 35(a) and Figure 35(c). Figure 35(d) reveals higher KAM values at FCC/HCP interfaces after FCC → HCP phase transformation. The formation of extrusions and intrusions occurs to accommodate the plastic strain associated with the FCC → HCP displacive transformation. Therefore, this morphological surface feature causes higher KAM values for HCP-phase when compared to that for FCC-phase, refer to histograms inserted in Figure 35. In addition, when comparing the KAM histogram for the FCC-phase shown in Figure 25 with the histogram presented in Figure 35, it is possible to observe an increase in frequency at higher angles for the FCC-phase, in accordance with the increase in the relative FWHM.

Figure 35 – Secondary electron SEM micrograph (a), EBSD band contrast map superimposed with HCP-martensite phase map (b), inverse pole figure map (c), and KAM map (d) of the reverse transformed sample after application of 1500 loading cycles. (BD = build direction, ND = normal direction, and LD = loading direction).

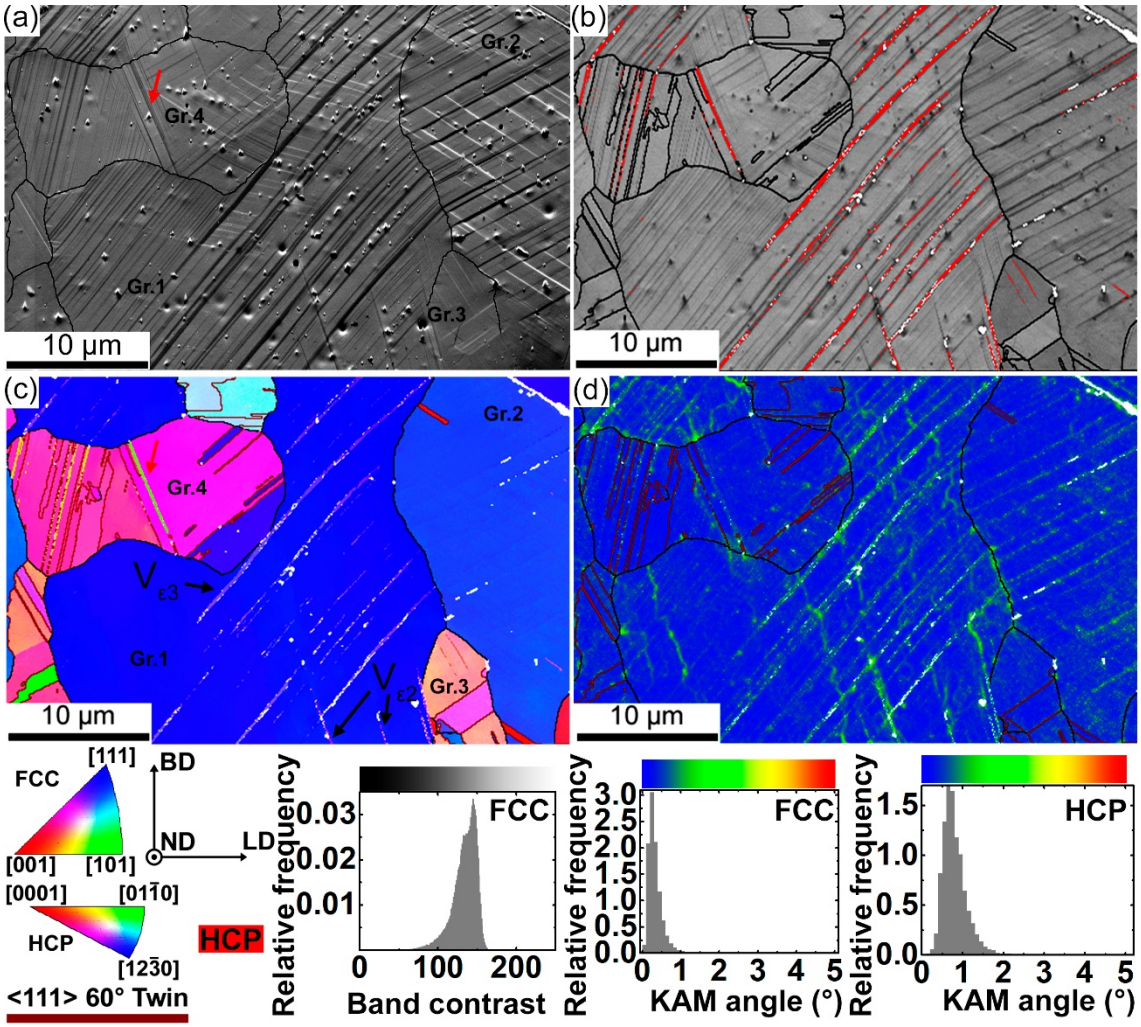

Source: Own elaboration.

From the grain marked as Gr.1 in Figure 35(c), which belongs to the $\{111\}_{FCC}$ family of planes, the Humbert' model approach was applied to calculate the HCP-distortional variants formed. The results are shown in the pole figures presented in Figure 36 and the calculations are shown in Table 7. Figure 36(a) and Figure 36(b) were experimentally determined for the FCC and HCP phases, respectively. Figure 36(c) shows the theoretically calculated HCP orientations. It is possible to observe that $(1\bar{1}1)[1\bar{1}\bar{2}]$ (Vε3) and the $(\bar{1}11)[\bar{1}1\bar{2}]$ (Vε2) distortional variants were formed. The same analysis was performed for additional three grains presented in Figure 35, and the results are shown in Appendix. For the other regions, the model still applies for the determination of the distortional variants observed. Two distortional variants ($(\bar{1}11)[\bar{1}1\bar{2}]$ (Vε3) and $(11\bar{1})[\bar{2}1\bar{1}]$ (Vε4)) were observed in Gr.2, and one ($(111)[11\bar{2}]$ (Vε1 – Gr.3), and $(1\bar{1}1)[\bar{2}11]$ (Vε3 – Gr.4)) in each of the other two grains. Therefore, four possible orientational variants are present after 1500 cycles. However, the severity factor

considered is not adequate to predict the formed variants. On the one hand, it was possible to identify two grains (Gr.1 and Gr.2) where it should be present in just one crystallographic variant. However, two can be observed in the inverse pole figure map, Figure 35(c). On the other hand, the observed variants in Gr.3 and in Gr.4 were not those with the highest mechanical work.

Figure 36 – Experimentally determined pole figures from the {111} grain (Gr.1) in Figure 11(b) of the FCC-phase (a) and HCP-phase (b), respectively. The calculated pole figures of the HCP-distortional variants are presented in (c).

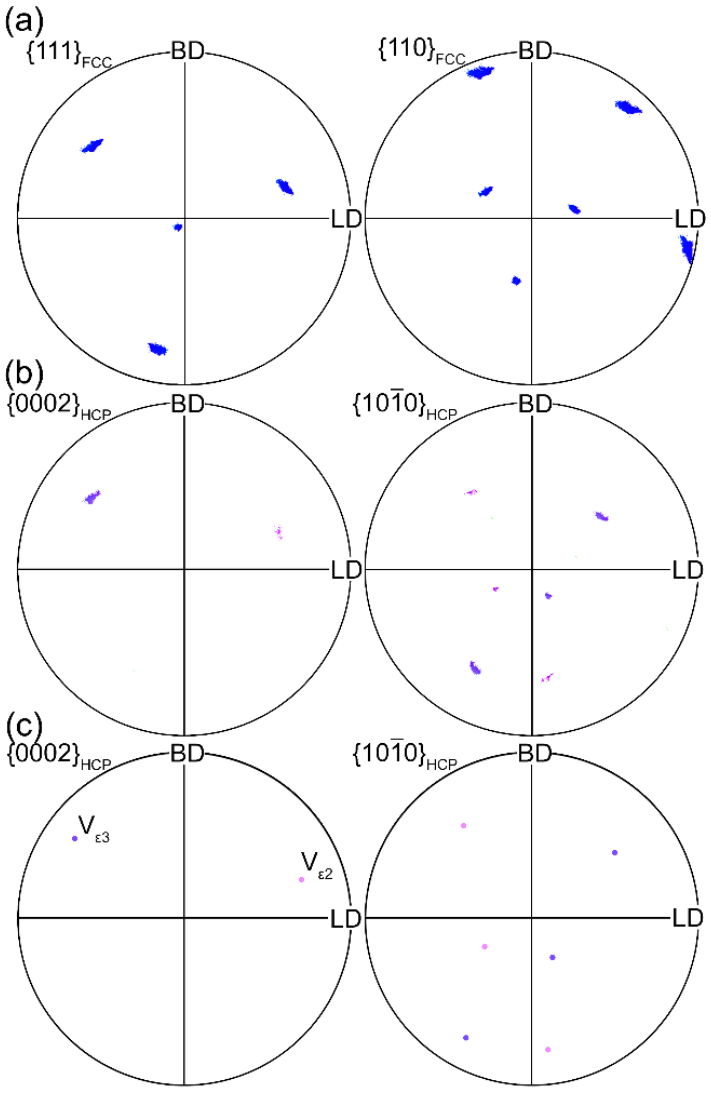

Source: Own elaboration.

Table 7 – Calculated crystallographic variants of the HCP-phase considering experimentally obtained Euler angles from the {111} grain (Gr.1) in Figure 11(b),

corresponding to the sample submitted to 1500 loading cycles. Experimentally determined Euler angles of the parent FCC-phase are represented by $[\Phi_1\ \Phi\ \Phi_2]_{FCC}$, with angles in degrees. Bold numbers indicate the experimentally observed distortional variants.

Variant	**Slip system**	**Gr.1 from {111}$_{FCC}$ family of planes**			
		[174.1 47.3 39.6]$_{FCC}$			
		Euler angles (°)			**Mechanical work (MJ/m^3)**
		Φ_1	**Φ**	**Φ_2**	
$V_{\varepsilon1}$	(111) [11$\bar{2}$]	322.9	8.5	297.8	0.2
	(111) [$\bar{2}$11]	322.9	8.5	57.8	-1.5
	(111) [1$\bar{2}$1]	322.9	8.5	177.8	1.2
$V_{\varepsilon2}$	($\bar{1}$11) [211]	108.7	63.4	95.1	-5.9
	($\bar{1}$11) [$\bar{1}\bar{2}$1]	108.7	63.4	335.1	-1.7
	($\bar{1}$11) [$\bar{1}$1$\bar{2}$]	**108.7**	**63.4**	**215.1**	**7.6**
$V_{\varepsilon3}$	(1$\bar{1}$1) [$\bar{2}\bar{1}$1]	233.7	70.4	200.9	-6.1
	(1$\bar{1}$1) [121]	233.7	70.4	80.9	-2.3
	(1$\bar{1}$1) [1$\bar{1}\bar{2}$]	**233.7**	**70.4**	**320.9**	**8.5**
$V_{\varepsilon4}$	(11$\bar{1}$) [112]	349.6	78.1	94.1	0.1
	(11$\bar{1}$) [$\bar{2}\bar{1}\bar{1}$]	349.6	78.1	334.1	-2.7
	(11$\bar{1}$) [1$\bar{2}\bar{1}$]	349.6	78.1	214.1	2.6

Source: Own elaboration.

4.4.5 Crystallographic texture evolution during cyclic deformation

Figure 37 shows the crystallographic texture in the investigated sample before and after the application of cyclic deformation. The results obtained both from the spherical harmonic texture coefficients determined by the Rietveld method and from the EBSD data are in good agreement, emphasizing that higher sampling of the SXRD implies lower intensities. In Figure 37, it is possible to note the low intensities resulting from the recrystallization occurred during the heat treatment. In addition, the applied cyclic deformation did not cause significant changes in the observed texture components, as shown in Table 8.

Figure 37 – Orientation distribution function (ODF) displayed at φ2 = 45° section calculated from the spherical harmonics coefficients determined by applying the Rietveld method to 24 azimuthal integrations of the synchrotron X-ray diffractograms for samples submitted to 0 cycles (a) and 1500 cycles (b). ODF displayed at φ2 = 45° section calculated from the EBSD data for sample submitted to 0 cycles (c) and 1500 cycles (d). The intensities are shown in multiples of random units – (m.r.u.).

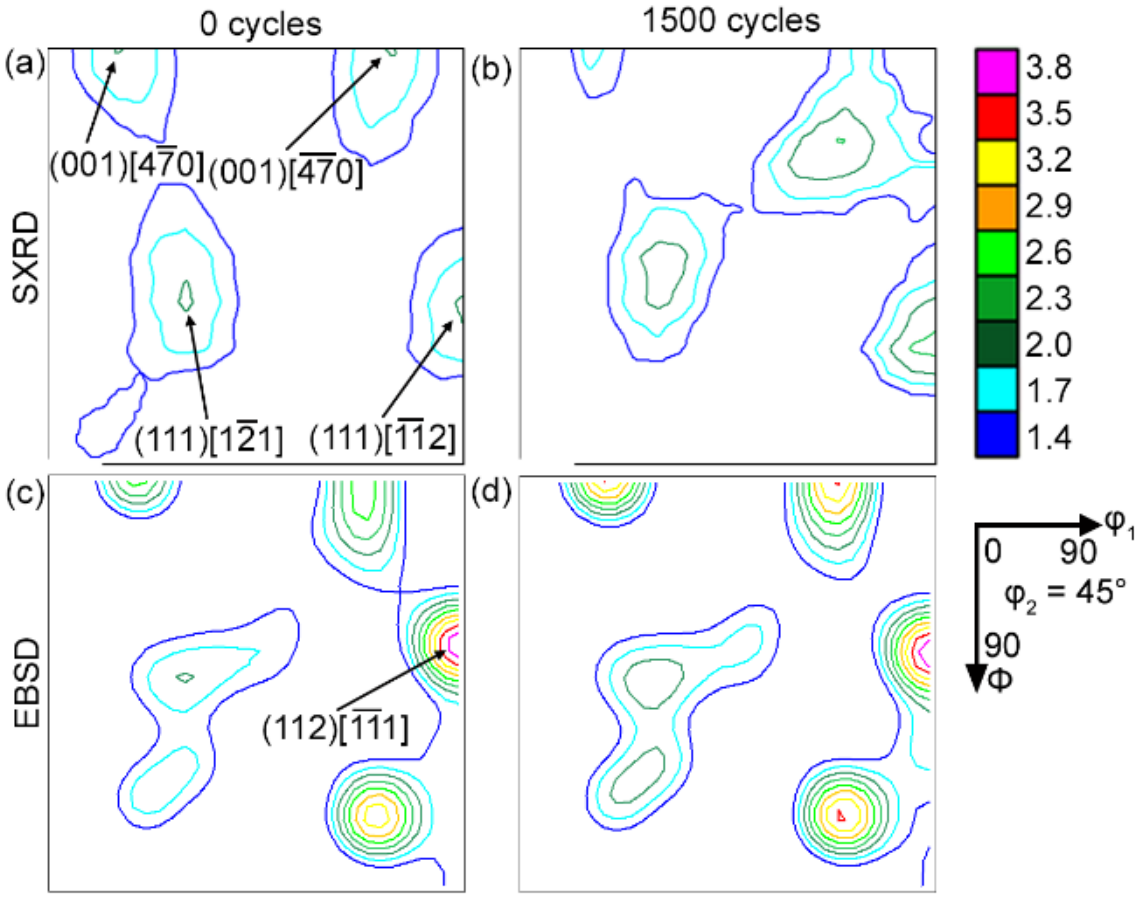

Source: Own elaboration.

Table 8 – Comparison of the intensities (m.r.u.) before and after application of cyclic loading obtained from SXRD data and EBSD data, respectively.

Euler angles			**Miller indices**	**SXRD**		**EBSD**	
φ1	**Φ**	**φ2**	**(hkl)[uvw]**	**0 cycles**	**1500 cycles**	**0 cycles**	**1500 cycles**
15	0	45	(001) [4$\bar{7}$0]	2.02	1.89	3.17	2.46
75	0	45	(001) [$\bar{4}$70]	2.02	1.89	2.5	1.97
30	55	45	(111) [1$\bar{2}$1]	2.06	2.08	1.88	1.61
90	55	45	(111) [$\bar{1}$12]	2.07	2.08	1.88	1.6
90	35	45	(112) [$\bar{1}\bar{1}$1]	1.16	1.37	3.78	3.99

Source: Own elaboration.

4.5 Discussion

4.5.1 Effect of the reverse transformation on the initial microstructure

The applied solution annealing treatment at 1150 °C for one hour was found to be adequate to produce equiaxed grains and cause residual stress relief. Kajima et al. (2018)

observed a similar behavior of a solution-annealed Co-Cr-Mo alloy. In addition, Kurosu, Matsumoto and Chiba (2010) observed that one cycle of reverse transformation treatment produced a partial grain size homogenization. These authors reported average grain sizes ranging from 20 μm to 25 μm after reverse transformation treatment (KUROSU; MATSUMOTO; CHIBA, 2010). This is in agreement with our results where recrystallized grains, Figure 25(a), and low KAM values, Figure 25(b), were identified.

Concerning the mechanism behind the nucleation of new FCC grains, the literature hypothesizes that a pearlite-type structure (FCC → HCP + carbides/carbonitrides) is formed during aging of a nitrogen-doped Co-Cr-Mo alloy. This structure enhances the number of nucleation sites for the FCC-phase during the reverse transformation (i.e., HCP + carbides/carbonitrides → FCC) (HASSANI et al., 2019; WEI et al., 2019; ZANGENEH; KETABCHI, 2013). Another possible explanation is based on the induction of thermal stresses and athermal HCP-phase (ZANGENEH et al., 2020). The proposed refinement mechanism is based on the recrystallization process. In such cases, due to the low alloy stacking fault energy, recrystallization is expected to occur through the reorientation of crystals located in heavily faulted regions (TOYODA et al., 1984). Therefore, the heavily deformed regions, induced by both the thermal stresses and athermal HCP-phase, would act as recrystallization sites for FCC grains (ZANGENEH et al., 2020).

This study displayed large variation in the average grain diameter, as depicted in Figure 25 and Figure 26. The reason for this can be the incompleteness of FCC to HCP + carbides/carbonitrides phase transformation. Figure 38 shows that solution annealing (1150 °C for 1 hour) and aging (800 °C for 24 hours) produce partially transformed structures with a 14% residual area fraction of the FCC-phase. Such microstructure provides fewer nucleation sites when compared to material that had undergone a full FCC → HCP transformation. An additional reason can be the presence of second-phase precipitates in the partially transformed alloy. These particles can lead to a grain boundary pinning, also contributing to the nonuniform grain diameter distribution.

Figure 38 – EBSD phase map of sample submitted to solution annealing (1150 °C for 1 hour) and aging (800 °C for 24 hours) heat treatment.

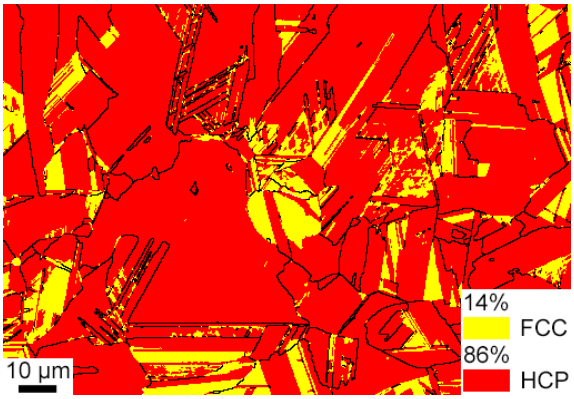

Source: Own elaboration.

Figure 39(a) shows a HAADF-STEM micrograph of the alloy of concern submitted to solution annealing (1150 °C for 1 hour). It is possible to observe randomly distributed precipitates in the FCC matrix with an approximate size of 4 nm. The chemical composition of one representative precipitate, the one highlighted by a red arrow, is shown in Figure 39(b). It is possible to note higher Cr and Mo contents in the precipitate compared to the matrix, as shown in Figure 39(c). The observed precipitates are presumably of the $M_{23}C_6$ type, which was also confirmed from the diffractogram shown in Figure 29(b) in addition to Thermo-Calc results presented in Figure 23. The $M_{23}C_6$ and Cr_2N precipitates have already been reported to form in this alloy system (KAJIMA et al., 2018; KUROSU; MATSUMOTO; CHIBA, 2010; ROUDNICKÁ et al., 2021b; TAKAICHI et al., 2020; WANG; MIYAGI; CHIBA, 2023; ZHANG et al., 2018).

Figure 39 – HAADF-STEM micrograph of sample subjected to solution annealing heat treatment at 1150 °C for 1 hour (a). EDS results of Co, Cr, and Mo contents of the precipitate depicted by the red arrow (b) and that of the FCC matrix (c).

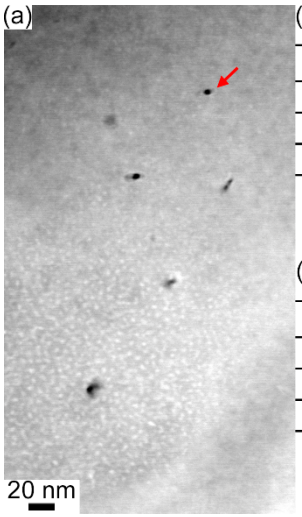

(b) Precipitate

Element	wt.-%
Co	60.8 (± 0.5)
Cr	26.6 (± 0.3)
Mo	9.0 (± 0.4)

(c) Matrix (FCC)

Element	wt.-%
Co	56.2 (± 0.5)
Cr	23.9 (± 0.3)
Mo	6.8 (± 0.4)

Source: Own elaboration.

4.5.2 Effect of cyclic loading on microstructural evolution

The HCP-phase developed by a stepwise progression of DIMT with each deformation step being preceded by a yielding region where there is no significant increase in the HCP-martensite, Figure 32. A similar plateau-like increase was found for BCC-martensite formed by a deformation-induced mechanism on austenitic steels (CELADA-CASERO et al., 2017; HEDSTRÖM et al., 2007; NARAGHI; HEDSTRÖM; BORGENSTAM, 2011). One possible explanation for such behavior is based on a two-stage mechanism: 1) the formation of many BCC-martensite nuclei with a suppressed growth, followed by 2) the rapid growth of the formed nuclei (CELADA-CASERO et al., 2017). The first stage corresponds to the plateau-like portion, and the second stage part is related to the step stage. Another hypothesis is based on the HCP → FCC martensitic transformation (WEI et al., 2020). According to this theory, the plateau stage is caused by the formation of a substantial number of new FCC nuclei due to the HCP to FCC phase transformation, which experiences minimal growth kinetics. This, in turn, would result in offsetting the expected increase in the HCP-phase fraction. The step stage, i.e., the rapid rise in the nominal HCP-phase fraction will occur when all possible nucleation sites of the FCC-phase are consumed.

In the present work, microstructural observation did not reveal the occurrence of the HCP → FCC transformation. Hence, it is proposed that each plateau-like region of the HCP-phase fraction corresponds to the nucleation stage of the new distortional HCP-variant, as observed in Figure 32 between 100 and 200 cycles. The steps are related to the rapid growth of the nucleated HCP-variant.

Figure 40 shows basal pole figures of HCP-martensite at 300 and 1500 loading cycles. These pole figures exhibit a strengthening of the intensities which further supports the hypothesis outlined in the previous paragraph. Please note the development of the pole highlighted by the red square whose intensity is 1.86 m.r.u. after 1500 cycles. The rotation observed around ND is presumably caused by the errors associated with the Rietveld refinement of the HCP-phase. These errors are due to the low relative fraction of the HCP-phase. These errors are due to the low relative fraction of the HCP-phase which influences the calculated spherical harmonic coefficients.

Figure 40 – Basal pole figures for the HCP-phase derived from SXRD data of samples subjected to 300 and 1500 loading cycles.

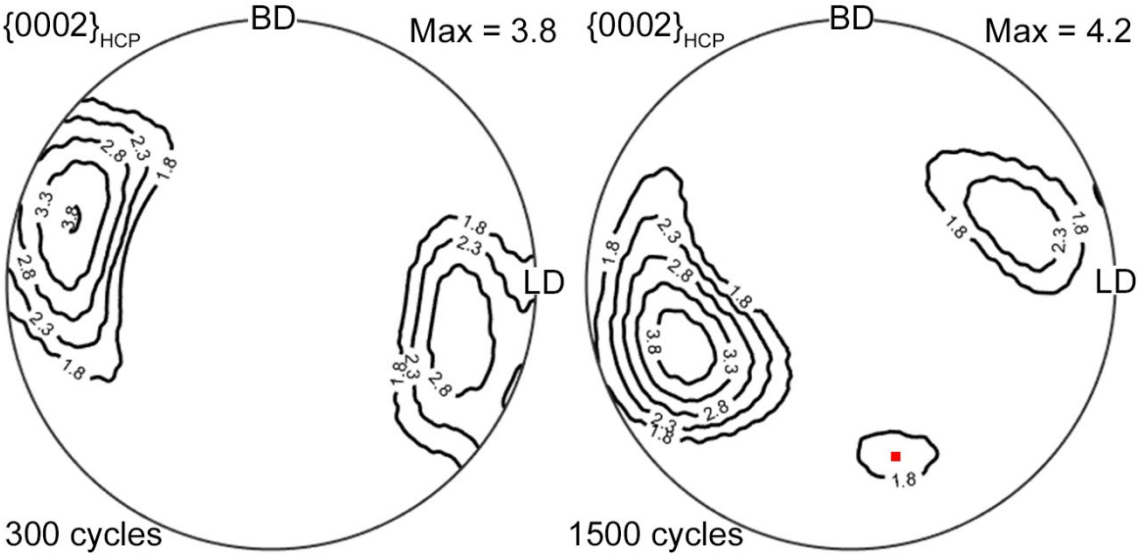

Source: Own elaboration.

The strain hardening revealed in Figure 33 is attributed to the formation of the HCP-martensite. This is because a higher critical resolved shear stress is necessary to activate the slip systems of the HCP-phase ({0001}<11$\bar{2}$0> basal and {1$\bar{1}$00}<11$\bar{2}$0> prismatic) when compared to that of the FCC-phase (KAITA et al., 2018). Indeed, the formation of the HCP-phase via the DIMT mechanism has been reported as one of the active strengthening mechanisms in Co-Cr-Mo alloys. In addition, the Lomer-Cottrell locks, grain boundaries, dislocation density, and stacking faults might also contribute to the observed increase in the strain hardening rate (CHEN et al., 2023; MORI et al., 2015).

Moreover, as plastic deformation progresses, the increase in the dislocation density causes alloy strengthening (MORI et al., 2012). The formation of HCP-martensite provides an increased number of phase boundaries which effectively suppresses the dislocation glide on the FCC-matrix (LIU et al., 2019). Therefore, one of the reasons for the observed strengthening is

based on the Hall-Petch relationship (HALL, 1951). In accordance with this model, the strength will rise with a reduction in the FCC-grain size due to its subdivision by newly formed HCP-variants.

When considering the stacking faults, these planar defects are also capable to hinder the dislocation glide. Therefore, as the plastic deformation advances with the application of more cycles, dislocations accumulate on stacking faults. Consequently, the stress needed to generate additional dislocations will increase. This behavior has been documented in low stacking fault energy Mg alloys (JIAN et al., 2013a). However, the same mechanism is expected to operate in other metallic polycrystals (JIAN et al., 2013a, 2013b; YAMANAKA et al., 2017), including Co-Cr-Mo alloy that have a low or negative stacking fault energy.

The activation of these mechanisms can therefore contribute to a surge in both the strain rate and the density of crystallographic defects. This can be qualitatively discerned by the increase in the relative FWHM, Figure 34. The relative FWHM was observed to correlate with the stepwise increase in the HCP-phase fraction. On the one hand, Mori et al. (MORI et al., 2019) showed that the formation of the HCP-phase by DIMT mechanism is accompanied by a reduction in the dislocation density of the matrix. It is to be noted that authors studied the transition between elastic and plastic deformation. On the other hand, Antunes et al. (2021) demonstrated that the FWHM of the FCC-phase increases as the HCP-phase soars, considering the plastic deformation during monotonic tensile loading of an additively manufactured Co-Cr-Mo alloy.

A peak broadening of the HCP-phase was also revealed in Figure 34. This broadening can be attributed to crystal deformation, crystallographic defect accumulation, and partition of the plastic strain between the HCP and FCC phases (LI et al., 2017). The Figure 34 also displayed the highest relative FWHM increase in the $\{311\}_{FCC}$ crystallographic plane and the lowest in the $\{111\}_{FCC}$ crystallographic plane. It is worth noting that such behavior is affected by the strain anisotropy associated with the dislocation type (BALOGH; RIBÁRIK; UNGÁR, 2006; UNGÁR; TICHY, 1999). However, this would require a full line-profile analysis, which is beyond the scope of the current work.

4.5.3 Effect of cyclic loading on the final microstructure

The observed nucleation of HCP-martensite at the twin boundaries indicates that they are of the incoherent type, as shown by the red arrows in Figure 35(a) and Figure 35(c),

consistent with the results proposed by Olson and Cohen (OLSON; COHEN, 1976b). Similar results were reported by Wang, Li, and Raabe (2018). In their work, the authors observed the thickening of the HCP-martensite until the formation of blocks, however, they did not discuss the nucleation of new HCP-variants with progressing strain.

In the present work, the identification of the observed distortional HCP-variants was conducted using Humbert's model. In line with this model, the suggested severity factor of 0.9 for the prediction of variant selection during tensile tests was employed. However, it is not clear if this value is also adequate for cyclic loading experiments. Figure 36 and Table 7 show that two orientational variants were formed after the application of 1500 cycles; however, according to the severity factor used, just one variant is to be expected. Similar results are shown in Appendix and were also found for as-built alloy under analogous cyclic loading conditions (SARAIVA et al., 2023). Humbert's model considers that the same macroscopic stress tensor will be applied to all FCC grains. Nevertheless, the stress distribution might be inhomogeneous after the formation of the first orientational HCP-variant. Indeed, a nonuniform stress field can arise from the constraint posed by impingement of the HCP-martensite with grain boundaries from adjacent grains (ZHANG et al., 2011).

In addition, the FCC grain size can influence the FCC → HCP phase transformation and the formation of crystallographic HCP-variants. This influence can be understood through the Hall-Petch relation, according to which flow stress increases when the average boundary spacing decreases (HANSEN, 2004). For this reason, deformation initially tends to concentrate in the larger grains. The smaller grains, in turn, deform when their flow stress reaches values close to those of the grains that have been subdivided by the formation of the HCP-phase. Therefore, the boundary spacing between the HCP/HCP and HCP/FCC interfaces is presumably the structural parameter that should be considered when discussing the Hall-Petch effect.

In this context, Li et al. (2017) applied the same strain magnitude to a material with different grain sizes that underwent solid-state FCC → HCP phase transformation. They observed that a smaller FCC grain size resulted in a lower relative HCP fraction and *vice versa*. This agrees well with the higher fraction of slip bands found in large grains highlighted as Gr.1 and Gr.2 when compared to smaller grains depicted as Gr.3 and Gr.4, as shown in Figure 35(c). Moreover, grain size inhomogeneity can be a reason for the discrepancy between the observed number of HCP orientational variants and that predicted based on the severity factor. According to Humbert's model, mechanical works are calculated on the basis of the same stress tensor for all grains, but this might not reflect the real stress state of a specific grain. For example, the

mechanical work values of Gr.2 and Gr.3 are very close; however, Gr.2 shows a higher fraction of slip bands, please refer to Appendix.

In addition to the grain size, the Schmid factor can also contribute to the partition of deformation among the grains, and the Schmid factor map is presented in Appendix. Table 9 displays the Schmid factor values corresponding to the Shockley partials for each of the grains highlighted in Figure 35(c). It is possible to note that the grains analyzed exhibit very similar Schmid factor values, ranging from 0.43 to 0.48. Notably, Gr.2 and Gr.3 grains stand out with values of 0.43 and 0.44, respectively. However, the large grain, Gr.2, has a higher fraction of slip bands, which further supports our hypothesis that grain size is the primary influencing factor on nonuniform strain distribution among the grains and, consequently, on the formation of HCP-variants. The same behavior was observed through results from Gr.1 and Gr.4.

Table 9 – Schmid factor for the Shockley partial dislocation slip system from the grains highlighted in Figure 35(c). The load direction was identical with that indicated in Figure 35 by LD.

Slip system	**{111}<112>**
Grain	**Schmid factor**
Gr.1	0.48
Gr.2	0.43
Gr.3	0.44
Gr.4	0.46

Source: Own elaboration.

4.5.4 Effect of the cyclic loading on the crystallographic texture

Figure 39 shows the ODF at section $\varphi_2 = 45°$ for the studied alloy in the as-built condition. In this figure, the {001}<110> and the copper components have higher intensities. The {001}<110> components ((001)//ND and [1$\bar{1}$0]//LD, for example) can be formed because the symmetry of the cubic crystal allows the [100] direction to remain aligned with the laser track, while the [110] direction remains parallel to the build direction (ZHOU et al., 2015). The copper component indicates that recrystallization is already taking place during the layer-by-layer manufacturing process. Thus, the microtexture seen in Figure 37 was formed through the recrystallization of the {001}<110> components toward the {001}<4$\bar{7}$0> components. It can also be seen that there was a reduction in the relative intensity levels.

Figure 41 – ODF displayed at φ2 = 45° section calculated from the EBSD data. (The intensities are shown in multiples of random units – m.r.u.).

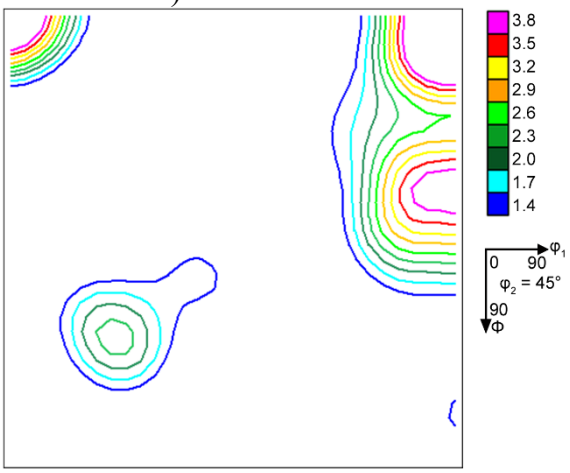

Source: Own elaboration.

It was also shown that the crystallographic texture of the FCC-phase did not change significantly after the application of 1500 cycles, as shown in Figure 39. Similar results were found for the F1537 Co-Cr-Mo alloy during monotonic tensile testing (CAI et al., 2018). In that study, a slight texture strengthening of the $\{111\}_{FCC}$ fiber was observed after approximately 9% engineering strain. Additionally, the presence of the {111}<112> component before plastic deformation may be attributed to the formation of annealing twins through the pilling up of Shockley partials in every $\{111\}_{FCC}$ plane (MEYERS; MURR, 1978).

This work brings insights into microstructural features that can be applied to enhance the lifespan of biomedical prostheses. A promising strategy in this regard, is an application of reverse transformation heat treatment, which results in a refined grain microstructure with equiaxed grains and a weak crystallographic texture. A reduction in grain size scales down the formation of the fragile HCP phase by the DIMT mechanism. At the same time, a weak crystallographic texture decreases the fraction of grains with high Schmid factor values for Shockley partials. As a result, the propensity to the plastic deformation is reduced.

4.6 Conclusions

The Co-28Cr-6Mo alloy was produced via L-PBF route and then subjected to the following heat treatment sequence: 1 - solution annealing, 2 - aging, and 3 – reverse transformation. After that, the effect of load-controlled cyclic deformation on the mechanical

and microstructural evolution was analyzed by combining electron backscatter diffraction and *in situ* synchrotron X-ray diffraction techniques. From this study, the following conclusions are drawn:

- The heat treatment sequence caused heterogeneous distribution of grain size that may be attributed to the grain boundary pinning effect of undissolved second-phase particles, specifically the $M_{23}C_6$ type.
- The heterogenous distribution of grain size caused a nonuniform distribution of strain and its accumulation in large grains.
- The stepwise increase of the macroscopic strain and the HCP volume fraction was associated with the FCC → HCP phase transformation. This phase transition progressed by the nucleation and growth of new HCP-variants. The increase of the HCP volume fraction contributed to the strain hardening of the alloy.
- Cyclic loading caused defect accumulation mostly in the $\{311\}_{FCC}$ crystallographic planes which was manifested by largest absolute increase of relative FWHM values.
- The plastic deformation and the FCC → HCP phase transformation generated during cyclic loading was not sufficient to cause changes in FCC crystallographic texture.

5 SUMMARY

In this study, a systematic microstructure-oriented plasticity analysis was carried out in additively manufactured Co-28Cr-6Mo alloy submitted to cyclic loading. This research topic was presented and discussed in two research papers, namely Chapters 3 and 4. Chapter 3 primarily explored the influence of HCP-martensite on crack nucleation and propagation. In this chapter, crack propagation was analyzed regarding the mechanical work of the HCP crystallographic variants. Chapter 4 studied the increase in plastic deformation with respect to the fraction of HCP-martensite produced by DIMT. This behavior was discussed concerning the nucleation and growth of the crystallographic HCP-variants. From the work conducted, the following conclusions are drawn:

1) The cyclic loading causes deformation-induced FCC → HCP phase transformation. The incremental growth of the HCP-phase fraction with a progressing number of loading cycles is the origin of a stepwise increase in plastic deformation. The slip incompatibility at the FCC/HCP interfaces promotes the accumulation of crystallographic defects in the matrix, contributing to the alloy's strain hardening.
2) The crack propagation is governed by the displacive FCC → HCP phase transformation, and cracks proceed on the HCP crystallographic variants. The zig-zag crack propagation path along FCC/HCP interfaces slows down the crack growth rate.
3) Humbert's model, which is commonly used for prediction of the martensite variant selection under static loading conditions, failed to predict HCP crystallographic variants that were formed during cyclic loading. This indicates the need for more advanced models considering dynamic strain accumulation.
4) The applied heat treatment sequence (solution annealing, aging, and reverse transformation) did not completely eliminate second-phase particles, including $M_{23}C_6$ carbides. Such precipitates can potentially impact grain growth and contribute to the heterogeneity in grain size distribution.
5) The heterogeneous grain size results in a nonuniform strain distribution during cyclic loading, where larger grains accumulate higher amounts of plastic deformation.

6) In the heat treated material, the $\{311\}_{FCC}$ crystallographic planes exhibited pronounced peak broadening, which was associated with a preferential accumulation of crystallographic defects in these planes.

These conclusions encapsulate the effects of microstructural evolution and phase transformation on the mechanical behavior of the Co-28Cr-6Mo alloy under cyclic loading, providing insights into optimizing processing conditions for improved fatigue performance of biomedical implants.

BIBLIOGRAPHY

ALKHAZRAJI, H. et al. Estimation of Dislocation Density in Cold-Rolled Commercially Pure Titanium by Using Synchrotron Diffraction. **Metallurgical and Materials Transactions B**, v. 45, n. 4, p. 1557–1564, 22 ago. 2014.

ANTUNES, L. H. M. et al. Effect of phase transformation on ductility of additively manufactured Co–28Cr–6Mo alloy: An in situ synchrotron X-ray diffraction study during mechanical testing. **Materials Science and Engineering: A**, v. 764, p. 138262, set. 2019.

ANTUNES, L. H. M. et al. Deformation-induced martensitic transformation in Co-28Cr-6Mo alloy produced by laser powder bed fusion: Comparison surface vs. bulk. **Additive Manufacturing**, v. 46, n. June, p. 102100, out. 2021.

ANTUNES, L. H. M. et al. Kinetics of FCC to HCP Transformation During Aging Heat Treatment of Co–28Cr–6Mo Alloy Fabricated by Laser-Powder Bed Fusion. **Metallurgical and Materials Transactions A**, v. 54, n. 6, p. 2329–2339, 13 jun. 2023.

ARANAS, C. et al. Determination of the critical stress associated with dynamic phase transformation in steels by means of free energy method. **Metals**, v. 8, n. 5, 2018.

ASTM, F. 1537–11. **Standard Specification for Wrought Cobalt-28Chromium-6Molybdenum Alloys for Surgical Implants**., 2011.

BACHMANN, F.; HIELSCHER, R.; SCHAEBEN, H. Texture analysis with MTEX- Free and open source software toolbox. **Solid State Phenomena**, v. 160, p. 63–68, 2010.

BAKER, H.; OKAMOTO, H. **ASM handbook. vol. 3. alloy phase diagrams**. ASM International, , 1992. Available from internet: <https://tajhizkala.ir/doc/ASM/ASM%20Handbook%20Vol%203.pdf>. Cited: 20 nov. 2022.

BALOGH, L.; RIBÁRIK, G.; UNGÁR, T. Stacking faults and twin boundaries in fcc crystals determined by x-ray diffraction profile analysis. **Journal of Applied Physics**, v. 100, n. 2, 15 jul. 2006.

BASAK, A.; DAS, S. Epitaxy and Microstructure Evolution in Metal Additive Manufacturing. **Annual Review of Materials Research**, v. 46, n. 1, p. 125–149, 1 jul. 2016.

BENATTI, E. A. et al. Generalized pole figures from post-processing whole Debye–Scherrer patterns for microstructural analysis on deformed materials. **Journal of Synchrotron Radiation**, v. 29, n. 3, p. 732–748, 1 maio 2022.

BÉREŠ, M. et al. Mechanical and phase transformation behaviour of biomedical Co-Cr-Mo alloy fabricated by direct metal laser sintering. **Materials Science and Engineering: A**, v. 714, p. 36–42, jan. 2018.

BIJUKUMAR, D. R. et al. Systemic and local toxicity of metal debris released from hip prostheses: A review of experimental approaches. **Nanomedicine: Nanotechnology, Biology and Medicine**, v. 14, n. 3, p. 951–963, 1 abr. 2018.

BOSE, S. et al. Additive manufacturing of biomaterials. **Progress in Materials Science**, v. 93, p. 45–111, abr. 2018.

CAI, S. et al. Room-Temperature Deformation and Martensitic Transformation of Two Co-Cr-Based Alloys. **Metallurgical and Materials Transactions A**, v. 49, n. 7, p. 2573–2577, 2 jul. 2018.

CAYRON, C. Angular distortive matrices of phase transitions in the fcc–bcc–hcp system. **Acta Materialia**, v. 111, p. 417–441, jun. 2016.

CELADA-CASERO, C. et al. In-Situ Investigation of Strain-Induced Martensitic Transformation Kinetics in an Austenitic Stainless Steel by Inductive Measurements. **Metals**, v. 7, n. 7, p. 271, 13 jul. 2017.

CHEN, Z. et al. Investigation of microstructures and strengthening mechanisms in an N-doped Co-Cr-Mo alloy fabricated by laser powder bed fusion. **Virtual and Physical Prototyping**, v. 18, n. 1, 31 dez. 2023.

CHEN, Z. W.; PHAN, M. A. L.; DARVISH, K. Grain growth during selective laser melting of a Co–Cr–Mo alloy. **Journal of Materials Science**, v. 52, n. 12, p. 7415–7427, 10 jun. 2017.

CHENG, X. et al. Fatigue crack growth in TRIP steel under positive R-ratios. **Engineering Fracture Mechanics**, v. 75, n. 3–4, p. 739–749, fev. 2008.

CUSTOMPART.NET. **Direct Metal Laser Sintering**. Available from internet: <http://www.custompartnet.com/wu/direct-metal-laser-sintering>. Cited: 18 nov. 2022.
DA SILVA COSTA, A. M. et al. Co–Cr–Mo alloy fabricated by laser powder bed fusion process: grain structure, defect formation, and mechanical properties. **The International Journal of Advanced Manufacturing Technology**, v. 116, n. 7–8, p. 2387–2399, 9 out. 2021.

DA SILVA LIMA, M. N. et al. Effect of ECAP processing temperature on an austenitic TWIP steel's microstructure, texture and mechanical properties. **Journal of Materials Research and Technology**, v. 24, p. 1757–1775, maio 2023.

DE CASTRO GIRÃO, D. et al. An assessment of biomedical CoCrMo alloy fabricated by direct metal laser sintering technique for implant applications. **Materials Science and Engineering: C**, v. 107, p. 110305, fev. 2020.

DONG, X. et al. Fatigue behavior of biomedical Co–Cr–Mo–W alloy fabricated by selective laser melting. **Materials Science and Engineering: A**, v. 795, p. 140000, 23 set. 2020.
EOS. **EOS CobaltChrome MP1**. , 2011. . Cited: 16 nov. 2022.

GONG, W. et al. Lattice parameters of austenite and martensite during transformation for Fe–18Ni alloy investigated through in-situ neutron diffraction. **Acta Materialia**, v. 250, p. 118860, maio 2023.

GRAY, G. T.; WILLIAMS, J. C.; THOMPSON, A. W. Roughness-Induced Crack Closure: An Explanation for Microstructurally Sensitive Fatigue Crack Growth. **Metallurgical**

Transactions A, v. 14, n. 2, p. 421–433, fev. 1983.

HALL, E. O. The Deformation and Ageing of Mild Steel: III Discussion of Results. **Proceedings of the Physical Society. Section B**, v. 64, n. 9, p. 747–753, 1 set. 1951.

HAN, J. et al. The size effect of initial martensite constituents on the microstructure and tensile properties of intercritically annealed Fe–9Mn–0.05C steel. **Materials Science and Engineering: A**, v. 633, p. 9–16, maio 2015.

HANSEN, N. Hall–Petch relation and boundary strengthening. **Scripta Materialia**, v. 51, n. 8, p. 801–806, out. 2004.

HASSANI, F. Z. et al. Effects of carbide precipitation on the microstructural and tribological properties of Co–Cr–Mo–C medical implants after thermal treatment. **Journal of Materials Science**, v. 51, n. 9, p. 4495–4508, 29 maio 2016.

HASSANI, F. Z. et al. Grain Refinement of Co-Cr-Mo-C Through Plastic Deformation Followed by Reversion of Lamellar Eutectoid Structure. **Journal of Materials Engineering and Performance**, v. 28, n. 2, p. 1112–1121, 2 fev. 2019.

HASTIE, G. R. et al. Study to Assess the Rate of Adverse Reaction to Metal Debris in Hip Resurfacing at a Minimum 13-year Follow-up. **The Journal of Arthroplasty**, v. 36, n. 3, p. 1055–1059, mar. 2021.

HEDSTRÖM, P. et al. Stepwise transformation behavior of the strain-induced martensitic transformation in a metastable stainless steel. **Scripta Materialia**, v. 56, n. 3, p. 213–216, fev. 2007.

HERMAWAN, H.; RAMDAN, D.; P. DJUANSJAH, J. R. Metals for Biomedical Applications. Em: **Biomedical Engineering - From Theory to Applications**. [s.l: s.n.].
HUMBERT, M. et al. Analysis of the γ–ε–α′ variant selection induced by 10% plastic deformation in 304 stainless steel at −60°C. **Materials Science and Engineering: A**, v. 454–455, p. 508–517, 25 abr. 2007.

IATECOLA, A. et al. Osseointegration Improvement of Co-Cr-Mo Alloy Produced by Additive Manufacturing. **Pharmaceutics**, v. 13, n. 724, 2021.

INTERNATIONAL STANDARD. **ISO 24173:2009(E) Microbeam analysis — Guidelines for orientation measurement using electron backscatter diffraction**. [s.l: s.n.].

JIAN, W. W. et al. Ultrastrong Mg Alloy via Nano-spaced Stacking Faults. **Materials Research Letters**, v. 1, n. 2, p. 61–66, 12 jun. 2013a.

JIAN, W. W. et al. Physics and model of strengthening by parallel stacking faults. **Applied Physics Letters**, v. 103, n. 13, 23 set. 2013b.

KAITA, W. et al. Plastic deformation mechanisms of biomedical Co–Cr–Mo alloy single crystals with hexagonal close-packed structure. **Scripta Materialia**, v. 142, p. 111–115, jan. 2018.

KAJIMA, Y. et al. Fatigue strength of Co–Cr–Mo alloy clasps prepared by selective laser melting. **Journal of the Mechanical Behavior of Biomedical Materials**, v. 59, p. 446–458, jun. 2016.

KAJIMA, Y. et al. Effect of heat-treatment temperature on microstructures and mechanical properties of Co–Cr–Mo alloys fabricated by selective laser melting. **Materials Science and Engineering: A**, v. 726, p. 21–31, maio 2018.

KOIZUMI, Y. et al. Strain-induced martensitic transformation near twin boundaries in a biomedical Co-Cr-Mo alloy with negative stacking fault energy. **Acta Materialia**, v. 61, n. 5, p. 1648–1661, 2013.

KOYAMA, M.; SAWAGUCHI, T.; TSUZAKI, K. Effects of Si on Tensile Properties Associated with Deformation-Induced ε-Martensitic Transformation in High Mn Austenitic Alloys. **MATERIALS TRANSACTIONS**, v. 56, n. 6, p. 819–825, 2015.

KUROSU, S. et al. The damage process in a biomedical Co–29Cr–6Mo–0.14N alloy analyzed by X-ray tomography and electron backscattered diffraction. **Scripta Materialia**, v. 64, n. 5, p. 367–370, 1 mar. 2011.

KUROSU, S.; MATSUMOTO, H.; CHIBA, A. Grain refinement of biomedical Co–27Cr–5Mo–0.16N alloy by reverse transformation. **Materials Letters**, v. 64, n. 1, p. 49–52, jan. 2010.

KWABENA ADOMAKO, N.; HAGHDADI, N.; PRIMIG, S. Electron and laser-based additive manufacturing of Ni-based superalloys: A review of heterogeneities in microstructure and mechanical properties. **Materials & Design**, v. 223, p. 111245, nov. 2022.

LEE, B. S.; MATSUMOTO, H.; CHIBA, A. Fractures in tensile deformation of biomedical Co–Cr–Mo–N alloys. **Materials Letters**, v. 65, n. 5, p. 843–846, mar. 2011.

LEE, J.-Y. et al. The effect of austenite grain size on deformation mechanism of Fe–17Mn steel. **Materials Science and Engineering: A**, v. 809, p. 140972, mar. 2021.

LI, H. et al. Grain boundary character distribution in the CoCrMo alloy processed by selective laser melting and post-heat treatment. **Journal of Materials Science**, v. 55, n. 35, p. 16780–16790, 11 dez. 2020.

LI, Y. P. et al. Role of nitrogen addition in stabilizing the γ phase of Biomedical Co-29Cr-6Mo alloy. **Materials Chemistry and Physics**, v. 133, n. 1, p. 29–32, 15 mar. 2012.

LI, Z. et al. A TRIP-assisted dual-phase high-entropy alloy: Grain size and phase fraction effects on deformation behavior. **Acta Materialia**, v. 131, p. 323–335, jun. 2017.

LIMA, M. N. DA S. et al. Influence of cold deformation on microstructure, crystallographic orientation and tensile properties of an experimental austenitic Fe–26Mn-0.4C steel. **Journal of Materials Research and Technology**, v. 19, p. 7–19, jul. 2022.

LIU, G. **Nucleation and Cross-slip of Partial Dislocations in FCC Metals**. [s.l.] University of California, 2009.

LIU, S. F. et al. Transformation-reinforced high-entropy alloys with superior mechanical properties via tailoring stacking fault energy. **Journal of Alloys and Compounds**, v. 792, p. 444–455, jul. 2019.

LIU, Y. et al. Tribological behavior of CoCrMo artificial knee joint with symmetrically biomimetic textured surfaces on PEEK. **Optics & Laser Technology**, v. 157, p. 108774, jan. 2023.

LONARDELLI, I. et al. Texture analysis from synchrotron diffraction images with the Rietveld method: dinosaur tendon and salmon scale. **Journal of Synchrotron Radiation**, v. 12, n. 3, p. 354–360, 1 maio 2005.

LÓPEZ, H. F.; SALDÍVAR, A.; HUANG, P. Development and Properties of ε-Martensite in Co-Cr-Mo Alloys for Biomaterials Applications. Em: **Properties of Complex Inorganic Solids 2**. Boston, MA: Springer US, 2000. p. 307–325.

LÓPEZ, H. F.; SALDIVAR-GARCIA, A. J. Martensitic transformation in a cast Co-Cr-Mo-C alloy. **Metallurgical and Materials Transactions A: Physical Metallurgy and Materials Science**, v. 39, n. 1, p. 8–18, 2008.

LUTTEROTTI, L.; VASIN, R.; WENK, H.-R. Rietveld texture analysis from synchrotron diffraction images. I. Calibration and basic analysis. **Powder Diffraction**, v. 29, n. 1, p. 76–84, 23 mar. 2014.

MENDES-FONSECA, N. et al. Dynamic Transformation During the Simulated Hot Rolling of an API-X80 Steel. **Steel Research International**, v. 90, n. 8, 2019.

MENG, Q. et al. In Situ Synchrotron X-ray Diffraction Investigations of the Nonlinear Deformation Behavior of a Low Modulus β-Type Ti36Nb5Zr Alloy. **Metals**, v. 10, n. 12, p. 1619, 2 dez. 2020.

MEYERS, M. A.; MURR, L. E. A model for the formation of annealing twins in F.C.C. metals and alloys. **Acta Metallurgica**, v. 26, n. 6, p. 951–962, jun. 1978.

MIRZAEIFAR, R. et al. A micromechanical analysis of the coupled thermomechanical superelastic response of textured and untextured polycrystalline NiTi shape memory alloys. **Acta Materialia**, v. 61, n. 12, p. 4542–4558, jul. 2013.

MITSUNOBU, T. et al. Role of strain-induced martensitic transformation on extrusion and intrusion formation during fatigue deformation of biomedical Co–Cr–Mo–N alloys. **Acta Materialia**, v. 81, p. 377–385, dez. 2014.

MORI, M. et al. Evolution of cold-rolled microstructures of biomedical Co-Cr-Mo alloys with and without N doping. **Materials Science and Engineering: A**, v. 528, n. 2, p. 614–621, dez. 2010.

MORI, M. et al. Microstructures and Mechanical Properties of Biomedical Co-29Cr-6Mo-0.14N Alloys Processed by Hot Rolling. **Metallurgical and Materials Transactions A**, v. 43, n. 9, p. 3108–3119, 5 set. 2012.

MORI, M. et al. Strengthening of biomedical Ni-free Co–Cr–Mo alloy by multipass “low-strain-per-pass” thermomechanical processing. **Acta Biomaterialia**, v. 28, p. 215–224, dez. 2015.

MORI, M. et al. Tuning strain-induced γ-to-ε martensitic transformation of biomedical Co–Cr–Mo alloys by introducing parent phase lattice defects. **Journal of the Mechanical Behavior of Biomedical Materials**, v. 90, p. 523–529, 1 fev. 2019.

MURR, L. E. et al. Next Generation Orthopaedic Implants by Additive Manufacturing Using Electron Beam Melting. **International Journal of Biomaterials**, v. 2012, p. 14, 2012.

NAJJAR, D. et al. Influence of a foreign body on the wear of metallic femoral heads and polyethylene acetabular cups of total hip prostheses. **Journal of Materials Science**, v. 35, n. 18, p. 4583–4588, 2000.

NARAGHI, R.; HEDSTRÖM, P.; BORGENSTAM, A. Spontaneous and Deformation-Induced Martensite in Austenitic Stainless Steels with Different Stability. **steel research international**, v. 82, n. 4, p. 337–345, 21 abr. 2011.

NAWABI, D. H. et al. What Causes Unexplained Pain in Patients With Metal-on metal Hip Devices? A Retrieval, Histologic, and Imaging Analysis. **Clinical Orthopaedics and Related Research®**, v. 472, n. 2, p. 543–554, 30 fev. 2014.

NISHIYAMA, Z. **Martensitic transformation**, v. 1. [s.l.] Elsevier, 1978.

OLSON, G. B.; COHEN, M. A general mechanism of martensitic nucleation: Part I. General concepts and the FCC → HCP transformation. **Metallurgical Transactions A**, v. 7, n. 12, p. 1897–1904, dez. 1976a.

OLSON, G. B.; COHEN, M. A general mechanism of martensitic nucleation: Part II. FCC → BCC and other martensitic transformations. **Metallurgical Transactions A**, v. 7, n. 12, p. 1905–1914, dez. 1976b.

OriginPro. Northampton, MA., 2019. Available from internet: <https://www.originlab.com/>

PARK, S.-Y. et al. Compressive deformation behavior and energy absorption characteristic of additively manufactured sheet CoCrMo triply periodic minimal surface lattices. **Journal of Materials Research and Technology**, v. 18, p. 171–184, maio 2022.

PAWLIK, K.; OZGA, P. LaboTex: the texture analysis software. **Göttinger Arbeiten zur Geologie und Paläontologie, SB4**, p. 146–147, 1999.

PETROV, YU. N. et al. Influence of microstructural modifications induced by ultrasonic impact treatment on hardening and corrosion behavior of wrought Co-Cr-Mo biomedical alloy. **Materials Science and Engineering: C**, v. 58, p. 1024–1035, jan. 2016.

PHAM, M. S.; HOLDSWORTH, S. R. Role of microstructural condition on fatigue damage development of AISI 316L at 20 and 300°C. **International Journal of Fatigue**, v. 51, p. 36–48, jun. 2013.

PHYSIOPEDIA. **Total Knee Arthroplasty**. Available from internet: <https://www.physio-pedia.com/Total_Knee_Arthroplasty>. Cited: 26 nov. 2022.

POLÁK, J. et al. The shape of extrusions and intrusions produced by cyclic straining. **Zeitschrift fuer Metallkunde/Materials Research and Advanced Techniques**, v. 94, n. 12, p. 1327–1330, 2003.

POLÁK, J.; MAN, J.; OBRTLÍK, K. AFM evidence of surface relief formation and models of fatigue crack nucleation. **International Journal of Fatigue**, v. 25, n. 9–11, p. 1027–1036, 1 set. 2003.

POLÁK, J.; SAUZAY, M. Growth of extrusions in localized cyclic plastic straining. **Materials Science and Engineering: A**, v. 500, n. 1–2, p. 122–129, 25 jan. 2009.

POLIAK, E. I.; JONAS, J. J. A one-parameter approach to determining the critical conditions for the initiation of dynamic recrystallization. **Acta Materialia**, v. 44, n. 1, p. 127–136, jan. 1996.

PRASAD, K. et al. Synchrotron diffraction characterization of dislocation density in additively manufactured IN 718 superalloy. **Materials Characterization**, v. 179, n. July, p. 111379, set. 2021.

PRASHANTH, K. G.; ECKERT, J. Formation of metastable cellular microstructures in selective laser melted alloys. **Journal of Alloys and Compounds**, v. 707, p. 27–34, jun. 2017.

PURNAMA, A. et al. Electroforming as a New Method for Fabricating Degradable Pure Iron Stent. Em: NIINOMI, M.; NARUSHIMA, T.; NAKAI, M. (Eds.). Springer Series in Biomaterials Science and Engineering. Berlin, Heidelberg: Springer Berlin Heidelberg, 2015. v. 4.

RAZAVI, N. et al. Effect of heat treatment on fatigue behavior of as-built notched Co-Cr-Mo parts produced by Selective Laser Melting. **International Journal of Fatigue**, v. 142, p. 105926, jan. 2021.

RODRIGUES, S. F. et al. Effect of Grain Size and Residual Strain on the Dynamic Transformation of Austenite under Plate Rolling Conditions. **Steel Research International**, v. 89, n. 6, 2018.

RODRIGUES, S. F.; ARANAS, C.; JONAS, J. J. Dynamic transformation during the simulated plate rolling of a 0.09% Nb Steel. **ISIJ International**, v. 57, n. 6, 2017.

ROUDNICKA, M. et al. Different Response of Cast and 3D-Printed Co-Cr-Mo Alloy to Heat Treatment: A Thorough Microstructure Characterization. **Metals**, v. 11, n. 5, p. 687, 22 abr. 2021a.

ROUDNICKÁ, M. et al. Microstructural instability of L-PBF Co-28Cr-6Mo alloy at elevated temperatures. **Additive Manufacturing**, v. 44, p. 102025, 1 ago. 2021b.

ROUDNICKÁ, M. et al. Heat treatment of laser powder-bed-fused Co–28Cr–6Mo alloy to remove its microstructural instability by massive FCC→HCP transformation. **Additive Manufacturing**, v. 47, p. 102265, nov. 2021c.

SALDÍVAR GARCÍA, A. DE J.; MEDRANO, A. M.; RODRÍGUEZ, A. S. Formation of hcp martensite during the isothermal aging of an fcc Co-27Cr-5Mo-0.05C orthopedic implant alloy. **Metallurgical and Materials Transactions A**, v. 30, n. 5, p. 1177–1184, maio 1999.

SAMES, W. J. et al. The metallurgy and processing science of metal additive manufacturing. **International Materials Reviews**, v. 61, n. 5, p. 315–360, 3 jul. 2016.

SARAIVA, B. R. C. et al. Effect of cyclic loading on microstructure and crack propagation in additively manufactured biomaterial Co–Cr–Mo alloy. **Journal of Materials Research and Technology**, v. 26, p. 3905–3916, set. 2023.

SCHOELL, R. et al. Investigation of the fatigue crack behavior of 304 stainless steels using synchrotron X-ray tomography and diffraction: Influence of the martensite fraction and role of inclusions. **Materials Characterization**, v. 188, p. 111903, jun. 2022.

SEKI, E. et al. Effect of heat treatment on the microstructure and fatigue strength of CoCrMo alloys fabricated by selective laser melting. **Materials Letters**, v. 245, p. 53–56, jun. 2019.

SONG, M. et al. Transformation induced crack deflection in a metastable titanium alloy and implications on transformation toughening. **Acta Materialia**, v. 118, p. 120–128, out. 2016.

STEPHENS, R. I. et al. **Metal fatigue in engineering**. [s.l.] John Wiley & Sons, 2000.

SWEENEY, C. A. et al. The role of elastic anisotropy, length scale and crystallographic slip in fatigue crack nucleation. **Journal of the Mechanics and Physics of Solids**, v. 61, n. 5, p. 1224–1240, maio 2013.

TAKAICHI, A. et al. Effect of heat treatment on the anisotropic microstructural and mechanical properties of Co–Cr–Mo alloys produced by selective laser melting. **Journal of the Mechanical Behavior of Biomedical Materials**, v. 102, p. 103496, fev. 2020.

TAKAKI, S.; NAKATSU, H.; TOKUNAGA, Y. Effects of Austenite Grain Size on ε Martensitic Transformation in Fe-15mass%Mn Alloy. **Materials Transactions, JIM**, v. 34, n. 6, p. 489–495, 1993.

TEOH, S. Fatigue of biomaterials: a review. **International Journal of Fatigue**, v. 22, n. 10, p. 825–837, 1 nov. 2000.

TOBY, B. H.; VON DREELE, R. B. *GSAS-II* : the genesis of a modern open-source all purpose crystallography software package. **Journal of Applied Crystallography**, v. 46, n. 2, p. 544–549, 1 abr. 2013.

TONELLI, L. Revealing the Hierarchical Microstructure of Innovative Additively Manufactured Metal Parts with Conventional Light Microscopy. **Metallography, Microstructure, and Analysis**, v. 10, n. 2, p. 278–282, 29 abr. 2021.

TONELLI, L.; AHMED, M. M. Z.; CESCHINI, L. A novel heat treatment of the additively manufactured Co28Cr6Mo biomedical alloy and its effects on hardness, microstructure and sliding wear behavior. **Progress in Additive Manufacturing**, v. 8, n. 2, p. 313–329, 24 abr. 2023.

TOYODA, K. et al. Effect of Stacking Fault Energy on Recrystallization in Cold Worked <I>FCC</I> Crystals. **Transactions of the Japan Institute of Metals**, v. 25, n. 5, p. 339–347, 1984.

TURNER, T. **Hip Replacement**. Available from internet: <https://www.drugwatch.com/hip-replacement/>. Cited: 26 nov. 2022.

UNGÁR, T.; TICHY, G. The Effect of Dislocation Contrast on X-Ray Line Profiles in Untextured Polycrystals. **physica status solidi (a)**, v. 171, n. 2, p. 425–434, fev. 1999.

WANG, H.; MIYAGI, T.; CHIBA, A. Effect of Multiple Reverse Transformation Treatments on Grain Refinement and Mechanical Properties of Biomedical Co–Cr–Mo–N Alloys Fabricated by Electron Beam Melting. **Materials**, v. 16, n. 19, p. 6528, 1 out. 2023.

WANG, M.; LI, Z.; RAABE, D. In-situ SEM observation of phase transformation and twinning mechanisms in an interstitial high-entropy alloy. **Acta Materialia**, v. 147, p. 236–246, abr. 2018.

WANG, X. et al. The dual role of martensitic transformation in fatigue crack growth. **Proceedings of the National Academy of Sciences**, v. 119, n. 9, 24 mar. 2022.

WANG, Z. et al. Additive manufacturing of a martensitic Co–Cr–Mo alloy: Towards circumventing the strength–ductility trade-off. **Additive Manufacturing**, v. 37, p. 101725, jan. 2021.

WEI, D. et al. Fatigue improvement of electron beam melting-fabricated biomedical Co–Cr–Mo alloy by accessible heat treatment. **Materials Research Letters**, v. 6, n. 1, p. 93–99, 2 jan. 2018.

WEI, D. et al. On microstructural homogenization and mechanical properties optimization of biomedical Co-Cr-Mo alloy additively manufactured by using electron beam melting. **Additive Manufacturing**, v. 28, p. 215–227, 1 ago. 2019.

WEI, S. et al. Plastic strain-induced sequential martensitic transformation. **Scripta Materialia**, v. 185, p. 36–41, ago. 2020.

WEI, S.; TASAN, C. C. Deformation faulting in a metastable CoCrNiW complex concentrated alloy: A case of negative intrinsic stacking fault energy? **Acta Materialia**, v. 200, p. 992–1007, nov. 2020.

WEISSENSTEINER, I. et al. Deformation-induced phase transformation in a Co-Cr-W-Mo alloy studied by high-energy X-ray diffraction during in-situ compression tests. **Acta Materialia**, v. 164, p. 272–282, fev. 2019.

WENK, H. R.; GRIGULL, S. Synchrotron texture analysis with area detectors. **Journal of Applied Crystallography**, v. 36, n. 4, p. 1040–1049, ago. 2003.

WILLMOTT, P. Introduction. Em: **An introduction to synchrotron radiation : techniques and applications**. [s.l.] John Wiley & Sons, 2011.

XIE, M. Y. et al. Texture analysis in cubic phase polycrystals by single exposure synchrotron X-ray diffraction. **Journal of Applied Physics**, v. 114, n. 16, p. 163502, 28 out. 2013.

YAMANAKA, K. et al. Ultrafine Grain Refinement of Biomedical Co-29Cr-6Mo Alloy during Conventional Hot-Compression Deformation. **Metallurgical and Materials Transactions A**, v. 40, n. 8, p. 1980–1994, 20 ago. 2009.

YAMANAKA, K. et al. Local strain evolution due to athermal γ→ε martensitic transformation in biomedical Co Cr Mo alloys. **Journal of the Mechanical Behavior of Biomedical Materials**, v. 32, p. 52–61, abr. 2014.

YAMANAKA, K. et al. Stacking-fault strengthening of biomedical Co–Cr–Mo alloy via multipass thermomechanical processing. **Scientific Reports**, v. 7, n. 1, p. 10808, 7 set. 2017.

YAMANAKA, K.; MORI, M.; CHIBA, A. Origin of Significant Grain Refinement in Co-Cr-Mo Alloys Without Severe Plastic Deformation. **Metallurgical and Materials Transactions A**, v. 43, n. 12, p. 4875–4887, 27 dez. 2012.

YAMANAKA, K.; MORI, M.; CHIBA, A. Nanoarchitectured Co–Cr–Mo orthopedic implant alloys: Nitrogen-enhanced nanostructural evolution and its effect on phase stability. **Acta Biomaterialia**, v. 9, n. 4, p. 6259–6267, abr. 2013.

YANG, J. et al. Materials for heterogeneous object 3D printing. Em: **Multimaterial 3D Printing Techology**. [s.l.] Elsevier, 2021. p. 113–152.

YANG, J. et al. Effects of deformation-induced martensitic transformation on cryogenic fracture toughness for metastable Si8V2Fe45Cr10Mn5Co30 high-entropy alloy. **Acta Materialia**, v. 225, p. 117568, fev. 2022.

ZANGENEH, S. et al. Evaluation of the aging effect on the microstructure of co-28cr-6mo-0.3c alloy: Experimental characterization and computational thermodynamics. **Metals**, v. 9, n. 5, p. 1–14, 1 maio 2019.

ZANGENEH, S. et al. The Effect of Cyclic Solution Heat Treatment on the Martensitic Phase Transformation and Grain Refinement of Co-Cr-Mo Dental Alloy. **Metals**, v. 10, n. 7, p. 861, 29 jun. 2020.

ZANGENEH, SH.; KETABCHI, M. Grain refinement by pearlitic-type constituents in Co–

28Cr–5Mo–0.3C alloy. **Materials Letters**, v. 94, p. 206–209, 1 mar. 2013.

ZHANG, M. et al. An investigation into the aging behavior of CoCrMo alloys fabricated by selective laser melting. **Journal of Alloys and Compounds**, v. 750, p. 878–886, jun. 2018.

ZHANG, M. et al. High cycle fatigue and ratcheting interaction of laser powder bed fusion stainless steel 316L: Fracture behaviour and stress-based modelling. **International Journal of Fatigue**, v. 121, p. 252–264, abr. 2019.

ZHANG, W. et al. Deformation processes of additively manufactured interstitial-strengthened high entropy alloy: In-situ high-energy synchrotron X-ray diffraction and microstructural appraisal. **Additive Manufacturing**, v. 76, p. 103791, ago. 2023.

ZHANG, X. et al. Orientation dependence of variant selection and intersection reactions of ϵ martensite in a high-manganese austenitic steel. **Philosophical Magazine Letters**, v. 91, n. 9, p. 563–571, set. 2011.

ZHAO, C. et al. Selective laser melting of Cu–Ni–Sn: A comprehensive study on the microstructure, mechanical properties, and deformation behavior. **International Journal of Plasticity**, v. 138, p. 102926, mar. 2021.

ZHONG, Z. Y. et al. Dislocation density evolution of AA 7020-T6 investigated by in-situ synchrotron diffraction under tensile load. **Materials Characterization**, v. 108, p. 124–131, out. 2015.

ZHOU, X. et al. Textures formed in a CoCrMo alloy by selective laser melting. **Journal of Alloys and Compounds**, v. 631, p. 153–164, maio 2015.

6 APPENDIX

Table 10 – Theoretical and experimental crystallographic variants of HCP-phase considering experimentally obtained Euler angles from the grain marked as Gr.2 in Figure 33(b), corresponding to the sample submitted to 1500 loading cycles. Experimentally determined Euler angles of the parent FCC-phase are represented by the $[\Phi_1\ \Phi\ \Phi_2]_{FCC}$ format, with angles in degree. Bold numbers indicate the experimentally observed distortional variants.

Variant	**Slip system**	**Gr.2 - theoretical**				**Gr.2 - experimental**		
		[40.8 42.7 35.2]$_{FCC}$				**[40.8 42.7 35.2]$_{FCC}$**		
		Euler angles (°)			**Mecha-nical work (MJ/m^3)**	**Euler angles (°)**		
		Φ_1	**ϕ**	**Φ_2**		**Φ_1**	**ϕ**	**Φ_2**
$V_{\varepsilon 1}$	$(111)\ [1\bar{1}2]$	186.0	14.1	298.3	0.3			
	$(111)\ [\bar{2}11]$	186.0	14.1	58.3	0.2			
	$(111)\ [1\bar{2}1]$	186.0	14.1	178.3	-0.4			
$V_{\varepsilon 2}$	$(\bar{1}11)\ [211]$	330.6	58.8	98.6	-0.9			
	$(\bar{1}11)\ [\bar{1}21]$	330.6	58.8	338.6	-5.3			
	$(\bar{1}11)\ [\bar{1}1\bar{2}]$	**330.6**	**58.8**	**218.6**	**6.2**	**150.9**	**122.1**	**22.1**
$V_{\varepsilon 3}$	$(1\bar{1}1)\ [\bar{2}11]$	99.3	70.7	195.1	4.0			
	$(1\bar{1}1)\ [121]$	99.3	70.7	75.1	-5.9			
	$(1\bar{1}1)\ [1\bar{1}\bar{2}]$	99.3	70.7	315.1	1.9			
$V_{\varepsilon 4}$	$(11\bar{1})\ [112]$	212.8	83.0	96.7	-1.5			
	$(11\bar{1})\ [\bar{2}1\bar{1}]$	**212.8**	**83.0**	**336.7**	**7.6**	**33.0**	**96.9**	**23.1**
	$(11\bar{1})\ [1\bar{2}1]$	212.8	83.0	216.7	-6.0			

Source: Own elaboration.

Table 11 – Theoretical and experimental crystallographic variants of HCP-phase considering experimentally obtained Euler angles from the grain marked as Gr.3 in Figure 33(b), corresponding to the sample submitted to 1500 loading cycles. Experimentally

determined Euler angles of the parent FCC-phase are represented by the $[\Phi_1\ \Phi\ \Phi_2]_{FCC}$ format, with angles in degree. Bold numbers indicate the experimentally observed distortional variants.

Variant	**Slip system**	**Gr.3 - theoretical**				**Gr.3 - experimental**		
		[94.5 25.8 66.1]$_{FCC}$				**[94.5 25.8 66.1]$_{FCC}$**		
		Euler angles (°)			**Mecha-nical work (MJ/m^3)**	**Euler angles (°)**		
		Φ_1	**ϕ**	**Φ_2**		**Φ_1**	**ϕ**	**Φ_2**
$V_{\varepsilon1}$	$(111)\ [11\bar{2}]$	**308.6**	**31.6**	**252.6**	**6.0**	**127.6**	**148.6**	**46.8**
	$(111)\ [\bar{2}11]$	308.6	31.6	12.6	-5.5			
	$(111)\ [1\bar{2}1]$	308.6	31.6	132.6	-0.5			
$V_{\varepsilon2}$	$(\bar{1}11)\ [211]$	38.6	66.9	123.8	-6.5			
	$(\bar{1}11)\ [\bar{1}\bar{2}1]$	38.6	66.9	3.8	7.7			
	$(\bar{1}11)\ [\bar{1}1\bar{2}]$	38.6	66.9	243.8	-1.3			
$V_{\varepsilon3}$	$(1\bar{1}1)\ [\bar{2}\bar{1}1]$	185.5	49.6	182.2	-1.3			
	$(1\bar{1}1)\ [121]$	185.5	49.6	62.2	0.5			
	$(1\bar{1}1)\ [1\bar{1}\bar{2}]$	185.5	49.6	302.2	0.8			
$V_{\varepsilon4}$	$(11\bar{1})\ [112]$	291.9	100.9	80.8	1.8			
	$(11\bar{1})\ [\bar{2}1\bar{1}]$	291.9	100.9	320.8	-6.4			
	$(11\bar{1})\ [1\bar{2}\bar{1}]$	291.9	100.9	200.8	4.6			

Source: Own elaboration.

Table 12 – Theoretical and experimental crystallographic variants of HCP-phase considering experimentally obtained Euler angles from the grain marked as Gr.4 in Figure 33(b), corresponding to the sample submitted to 1500 loading cycles. Experimentally determined

Euler angles of the parent FCC-phase are represented by the $[\Phi_1\ \Phi\ \Phi_2]_{FCC}$ format, with angles in degree. Bold numbers indicate the experimentally observed distortional variants.

Variant	Slip system	Gr.4 - theoretical [94.5 25.8 66.1]$_{FCC}$				Gr.4 - experimental [94.5 25.8 66.1]$_{FCC}$		
		Euler angles (°)			Mechanical work (MJ/m^3)	Euler angles (°)		
		Φ_1	ϕ	Φ_2		Φ_1	ϕ	Φ_2
$V_{\varepsilon1}$	$(111)\ [11\bar{2}]$	217.5	25.8	274.6	2.9			
	$(111)\ [\bar{2}11]$	217.5	25.8	34.6	1.6			
	$(111)\ [1\bar{2}1]$	217.5	25.8	154.6	-4.5			
$V_{\varepsilon2}$	$(\bar{1}11)\ [211]$	331.0	57.8	115.0	1.0			
	$(\bar{1}11)\ [\bar{1}2\bar{1}]$	331.0	57.8	355.0	-6.2			
	$(\bar{1}11)\ [\bar{1}1\bar{2}]$	331.0	57.8	235.0	5.2			
$V_{\varepsilon3}$	$(1\bar{1}1)\ [\bar{2}11]$	**113.0**	**61.6**	**183.5**	**6.0**	**113.0**	**61.2**	**3.0**
	$(1\bar{1}1)\ [121]$	113.0	61.6	63.5	-8.1			
	$(1\bar{1}1)\ [1\bar{1}2]$	113.0	61.6	303.5	2.1			
$V_{\varepsilon4}$	$(11\bar{1})\ [112]$	221.8	96.2	92.0	0.5			
	$(11\bar{1})\ [\bar{2}1\bar{1}]$	221.8	96.2	332.0	7.3			
	$(11\bar{1})\ [1\bar{2}1]$	221.8	96.2	212.0	-7.9			

Source: Own elaboration.

Figure 42 – Schmid factor map for Shockley partial dislocation slip system from the grains highlighted in the Figure 33(b). The load direction was the same indicated in Figure 33 by LD.

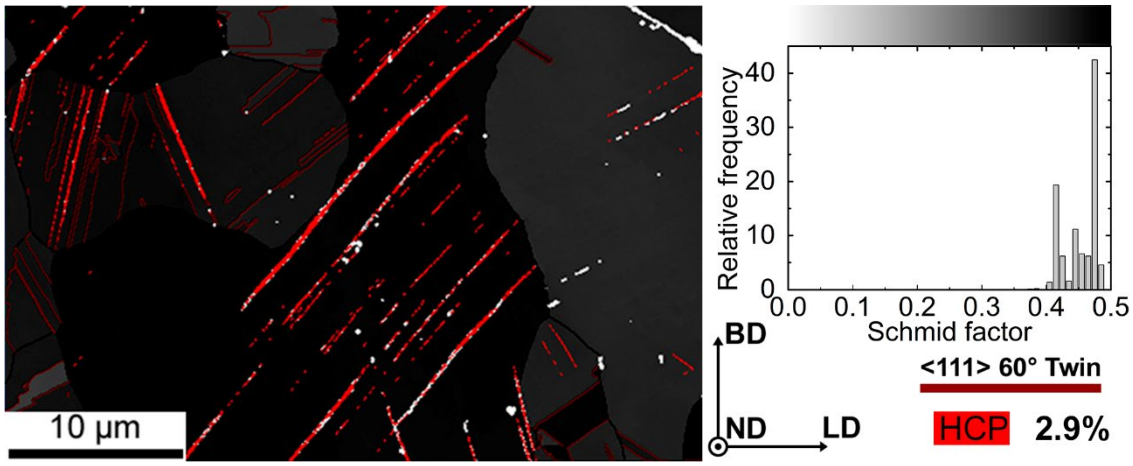

Source: Own elaboration.